**Calhoun: The NPS Institutional Archive**

**DSpace Repository**

Theses and Dissertations                               1. Thesis and Dissertation Collection, all items

1999-03

# Mapping coastal surface winds in Monterey Bay using high frequency radar

Delgado, Raymond R.

Monterey, California. Naval Postgraduate School

http://hdl.handle.net/10945/13596

http://www.nps.edu/library

# NAVAL POSTGRADUATE SCHOOL
## Monterey, California

# THESIS

| |
|---|
| **MAPPING COASTAL SURFACE WINDS IN MONTEREY BAY USING HIGH FREQUENCY RADAR**<br><br>by<br><br>Raymond R. Delgado III<br><br>March 1999<br><br><br>Thesis Advisor:                        Jeffrey D. Paduan<br>Thesis Co-Advisor:             Carlyle H. Wash |

**Approved for public release; distribution is unlimited.**

| REPORT DOCUMENTATION PAGE | | Form Approved OMB No. 0704-0188 |
|---|---|---|
| Public reporting burden for this collection of information is estimated to average 1 hour per response, including the time for reviewing instruction, searching existing data sources, gathering and maintaining the data needed, and completing and reviewing the collection of information. Send comments regarding this burden estimate or any other aspect of this collection of information, including suggestions for reducing this burden, to Washington headquarters Services, Directorate for Information Operations and Reports, 1215 Jefferson Davis Highway, Suite 1204, Arlington, VA 22202-4302, and to the Office of Management and Budget, Paperwork Reduction Project (0704-0188) Washington DC 20503. | | |
| **1. AGENCY USE ONLY** *(Leave blank)* | **2. REPORT DATE** March 1999 | **3. REPORT TYPE AND DATES COVERED** Master's Thesis |
| **4. TITLE AND SUBTITLE** MAPPING COASTAL SURFACE WINDS IN MONTEREY BAY USING HIGH FREQUENCY RADAR | | **5. FUNDING NUMBERS** |
| **6. AUTHOR(S)** Raymond R. Delgado III | | |
| **7. PERFORMING ORGANIZATION NAME(S) AND ADDRESS(ES)** Naval Postgraduate School Monterey, CA 93943-5000 | | **8. PERFORMING ORGANIZATION REPORT NUMBER** |
| **9. SPONSORING / MONITORING AGENCY NAME(S) AND ADDRESS(ES)** | | **10. SPONSORING / MONITORING AGENCY REPORT NUMBER** |

**11. SUPPLEMENTARY NOTES**
The views expressed in this thesis are those of the author and do not reflect the official policy or position of the Department of Defense or the U.S. Government.

| **12a. DISTRIBUTION / AVAILABILITY STATEMENT** Approved for public release; distribution is unlimited. | **12b. DISTRIBUTION CODE** |
|---|---|

**13. ABSTRACT** *(maximum 200 words)*

Over-water wind directions derived from high frequency (HF) radar - the new Multi-frequency Coastal Radar (MCR) - are compared to in-situ observations to determine the skill of the radar measurements. Conventional beam processing of data collected from two MCR sites located around Monterey Bay during summer 1997 is used to create wind directions based on the relative strength of the positive and negative Bragg-resonant peaks, which correspond to the wind-driven waves approaching and receding from the radar, respectively. Based on a selected functional relationship that converts the radar signal to wind direction, radar-derived wind directions are created using a new wind-retrieval algorithm and are compared to mooring observations under a variety of wind conditions. Analysis indicates that the signal not only follows wind direction, but also strongly correlates to the wind speed measured at the mooring. Results show that many of the Bragg peaks are close to the noise level, and consequently, low signal-to-noise ratios restrict the statistical confidence of the measurements. Nonetheless, maps of radar-derived wind directions show good agreement with in situ observations, especially when the wind speed is relatively strong and is sustained for long duration.

| **14. SUBJECT TERMS** HF Radar, Diurnal winds, HF Surface Current Radar, Mesoscale circulations, Monterey Bay Circulation, Wind direction, Sea breeze, Surface winds, Multi-frequency radar, wind maps. | **15. NUMBER OF PAGES** 135 |
|---|---|
| | **16. PRICE CODE** |

| **17. SECURITY CLASSIFICATION OF REPORT** Unclassified | **18. SECURITY CLASSIFICATION OF THIS PAGE** Unclassified | **19. SECURITY CLASSIFI- CATION OF ABSTRACT** Unclassified | **20. LIMITATION OF ABSTRACT** UL |
|---|---|---|---|

# MAPPING COASTAL SURFACE WINDS IN MONTEREY BAY USING HIGH FREQUENCY RADAR

Raymond R. Delgado III
Lieutenant, United States Navy
B.S., Iowa State University, 1991

Submitted in partial fulfillment of the
requirements for the degrees of

## MASTER OF SCIENCE IN METEOROLOGY
### AND
## MASTER OF SCIENCE IN PHYSICAL OCEANOGRAPHY

from the

### NAVAL POSTGRADUATE SCHOOL
**March 1999**

Author: _____

Raymond R. Delgado III

Approved by: _____

Jeffrey D. Paduan, Thesis Advisor

_____

Carlyle H. Wash, Thesis Co-Advisor;
Chairman, Department of Meteorology

_____

Roland W. Garwood, Jr., Chairman
Department of Oceanography

# ABSTRACT

Over-water wind directions derived from high frequency (HF) radar - the new Multi-frequency Coastal Radar (MCR) - are compared to in-situ observations to determine the skill of the radar measurements. Conventional beam processing of data collected from two MCR sites located around Monterey Bay during summer 1997 is used to create wind directions based on the relative strength of the positive and negative Bragg-resonant peaks, which correspond to the wind-driven waves approaching and receding from the radar, respectively. Based on a selected functional relationship that converts the radar signal to wind direction, radar-derived wind directions are created using a new wind-retrieval algorithm and are compared to mooring observations under a variety of wind conditions. Analysis indicates that the signal not only follows wind direction, but also strongly correlates to the wind speed measured at the mooring. Results show that many of the Bragg peaks are close to the noise level, and consequently, low signal-to-noise ratios restrict the statistical confidence of the measurements. Nonetheless, maps of radar-derived wind directions show good agreement with in situ observations, especially when the wind speed is relatively strong and is sustained for long duration.

# TABLE OF CONTENTS

# ACKNOWLEGMENTS

# I. INTRODUCTION

The use of reflected high frequency (HF) electromagnetic waves to remotely-sense ocean properties has been demonstrated to be an effective observation technique (Paduan and Rosenfeld, 1996; Haus et al., 1997). Systems such as the Coastal Ocean Dynamics Applications Radar (CODAR) continue to gain confidence as a high-resolution measurement tool and attain popularity as a research utility. Additional environmental variables can also be attained from the HF signal reflected from the ocean surface. Marine wind direction can be deduced, given that a suitable relationship relating the reflected HF signal to the wind-driven ocean gravity waves is known. Recent improvements of automated ground-wave HF radar systems with relatively low output power that are capable of sensing ~10 m wavelength gravity waves have made continuous measurements possible at various sites. Further study and evaluation of these independent mesoscale coastal wind data are needed to lend credence to its output and determine its potential use in a research and operational setting.

The principle advantage of HF-derived wind information is the spatial coverage and resolution which would not otherwise be possible with in-situ measurement platforms. The unique ability of ground-wave HF radar to instantaneously measure areas on the order of hundreds of square kilometers with a resolution of a few kilometers holds the potential of revealing mesoscale wind structures, like sea breeze evolutions or flow near topography or port entrances, that would otherwise be under-sampled or even unnoticed by ship-based sensors or single buoy moorings. Since the resolution of HF measurements is on

1

the same order as many coastal mesoscale meteorological models, the radar data could potentially be used as an additional input into the numerical models or regional observation networks.

However, this remotely-sensed method is a fairly unproven technique with inherent limitations. The accuracy of HF wind measurements depends on the validity of the relationship of the radar signal to the actual wind direction as well as the physical limitations of the radar such as power and antenna considerations. Moreover, the technique's accuracy reduces during transient environmental conditions such as shifts in wind velocity due to passage of a weather front or sea-breeze evolution. These features are of particular importance to the accuracy of HF measurements since the radar is detecting wind-driven gravity waves which build and decay according to the wind forcing. Thus, it is important that non-steady state conditions be identified, and the output of the radar be thoroughly studied during these occasions.

Numerous studies have examined the utility of HF radar for wind measurement (Long and Trizna, 1973; Ahern et al., 1974; Stewart and Barnum, 1975; Georges et al., 1993). These experiments studied the use of HF radar using sky-wave propagation. Applications of those high-powered systems were used to measure storms at great distances, particularly hurricanes, over the radio horizon. Although the measurement principle is nearly identical for ground-wave radar (ionospheric effects need not be accounted for in coastal systems), relatively few studies have been done. Heron et al. (1985) conducted experiments with single-frequency ground-wave radar in seas sheltered from ocean swell. Recent work by Vesecky et al. (1998) used the newly developed Multi-frequency Coastal

2

Radar (MCR) set up at two sites around Monterey Bay, California to compare the wind direction derived from four HF frequencies to in-situ data collected at a mooring and a streamline blend of numerical model and local land observations.

This thesis will further examine the skill of the MCR based on different wind algorithms and compare its output to in-situ observations. The radar and in-situ measurements will be compared over an approximately two-month period during the summer 1997 in Monterey Bay, California to determine not only the skill of the radar, but characterize radar output during various wind regimes relative to the shape of the coastline in Monterey Bay and the position of radar sites. The means of deducing surface wind direction from the radar signal will be described in Section II. Section III describes the MCR and the required data processing needed to display its output. Section III also outlines the attributes of the in-situ observation sites used for comparison to the radar data. Analysis of the observations, wind maps, comparisons, and other results are given in Section IV. A summary and recommendations are contained in Section V.

## II. BACKGROUND

## A.   HIGH FREQUENCY RADAR WIND MEASUREMENT TECHNIQUE

Wind measurements derived from reflected HF radio waves are based on the ratio of the strong first-order peaks that appear in the received Doppler shift spectrum corresponding to the wind-driven ocean waves of resonant length traveling radially toward or away from the radar site.   The wavelengths of HF radar are such that the resonant backscattering, the phenomenon known as "Bragg scattering," occurs due to the coherent reflection of the transmitted energy by short ocean gravity waves (~ 10-30 m) with wavelength specifically one-half of that of the radar wavelength.   Because the sea surface is not a single sinusoidal waveform but an infinite sum of moving wave components, the reflected electromagnetic signal will produce a full energy spectrum instead of single Doppler lines.   Figure 1 is an example of a received power spectrum from a particular azimuth and range cell.   The horizontal axis is marked by positive (waves approaching the receiver) and negative (wave receding from the receiver) Doppler shifts from the radar frequency ('0' on the horizontal axis).   The vertical axis is the power level in decibels.   The echo power is directly proportional to wave energy per unit area in a particular sea-wave component.   Since only sea-wave components travelling directly towards or away from the radar satisfy the Bragg condition, inspection of the amplitude of the corresponding positively and negatively Doppler-shifted lines from a particular patch

of sea indicates the ratio of energy in the approaching and receding wind-driven waves, and thus, a measure of wind direction (Shearman, 1981).

It is important to distinguish the difference between the way that wind direction and ocean currents are deduced from the same power density spectrum. While wind measurements are simply made from the ratio of the positive and negative peak levels, current measurements are derived from the frequency shifts due to the phase speed of traveling ocean waves and the speed of the underlying ocean current. The phase speed contribution of the resonant wave speed can be computed and subtracted from the observed Doppler shift so that the remaining portion can be attributed to the ocean current. Unlike the wind measurement, the radar sees only the component of the total surface current that is oriented radially along the look direction of the radar.

Figure 2 illustrates how the wind and current measurements, as well as other parameters, can be derived from the HF backscatter energy spectrum. The robustness of these derivations varies depending on the sensitivity and signal-to-noise ratios of present radar systems and the relationship relating the measured quantity to the physical parameter.

Wind speed is neither directly measured by HF radar nor easily discernable from the power spectrum. Instead, wind speed is inferred by a variety of ways including line broadening of the first-order peaks (Steward and Barnum, 1975), comparing the second-order spectral content to the Bragg line power or relating wind speed to significant wave height calculated from the returned radar echo (Heron et al., 1985). The success of these approaches has varied, but their results are often poor in low-wind speed conditions or

limited fetch regions. As an alternative approach, the unique capability of the MCR to simultaneously sense four Bragg-resonant ocean waves enables measurement of the near-surface current shear (the effective current depth of each resonant wave can be estimated, as modeled by Ha {1979}). It is expected that over-water wind speed should be positively correlated with the ocean current shear that can be measured by the MCR. Although ocean stratification and the poorly understood mechanisms by which momentum is transferred through the air-sea interface complicate this approach, there is potential to more directly measure wind speeds in varied wind conditions.

## B.   WIND-DRIVEN WAVE GENERATION AND ENERGY DISTRIBUTION

The wind direction derived from HF radar measurements fundamentally depends on the wind-sea conditions before and during radar illumination of the sea surface. Kinsman (1965) and Shearman (1981) discuss at length the mechanism of wind-wave generation. The key factor from the standpoint of HF radar is the condition known as a "fully developed" sea. Surface wind moving over a initially glassy calm sea will produce small ripples on the surface which are of the order of a few centimeters in wavelength. Satellite or aircraft-based scatterometers use short wavelengths (~ 1 cm) that sense Bragg scattering from these ocean capillary waves. The dominate restoring force for waves up to 1.7 cm in length is surface tension of the water. If the wind continues long enough and with sufficient fetch, the capillary waves continue to organize and build to increase the friction experienced by the wind moving over the sea surface. Once waves become greater than 1.7 cm in length, gravity becomes their dominate restoring force. The

presence of these longer waves further enhances the transfer of momentum from the air to the sea so that progressively longer gravity waves are produced. In addition, nonlinear processes allow the exchange of momentum between waves of different length. For a given wind speed momentum transfer occurs to all waves with phase speed up to the speed of the wind since no mechanism exists to force the sea beyond the wind speed. Eventually, an equilibrium is reached when the amplitude of the gravity waves of each wavelength remains constant, and a fully developed sea is said to exist.

Since gravity waves are dispersive in deep-water propagation, waves of different wavelengths travel at different speeds and thus have different frequencies. The phase speed of a gravity wave is given by:

$$c_w = \sqrt{gL/2\pi} = f_w L \qquad [1]$$

where $c_w$ is phase velocity of the gravity wave, g is the acceleration of gravity, $f_w$ is the wave frequency and L is the wavelength. Due to the dispersiveness of the waves, an infinite range of frequencies extending from capillary up to the maximum allowed for a given wind speed produces a spectrum of phase velocities and wave energy. Although waves will predominately propagate in the direction of the wind forcing, there is spread of the wave energy in all directions much like the manner in which ripples travel in all directions when a thrown stone strikes water. The ripples favor the direction from which the stone was thrown, but less dominant waves move in all directions. The distribution of wave energy per unit area, which is dependant on wave frequency, wind speed and direction, can be expressed by:

8

$$(\text{Wave Energy}) \, \text{m}^{-2} = \rho \, g \int S(\, f_w, \, \theta, u \,) \, df_w \, d\theta \quad \text{joules} \, \text{m}^{-2} \qquad [2]$$

where $\rho$ is the density of water, u is the wind velocity and $\theta$ is the angle between the direction of travel of a particular wave component and the reference direction, usually the direction of the mean wind (Shearman, 1981). The directional wave height variance spectrum $S(f_w, \theta, u)$ has dimensions $\text{m}^2 \, \text{Hz}^{-1} \, \text{rad}^{-1}$ and has temporal dependence implied with the wind speed. The spectrum can be factored into temporal and directional expressions:

$$S(\, f_w, \, \theta, u \,) = S_0(\, f_w, u \,) \, G(\theta, u) \qquad [3]$$

where $G(\theta, u)$ is dimensionless ( $\int G(\theta, u) \, d\theta = 1$ ). The amplitude of the Bragg-related component of the directional time-averaged sea spectrum is expressed in the first order radar return (Hasselman, 1971), and thus contains the radar-derived wind direction.

Traditional determination of this directional factor is difficult. Crude physical measurements can be made by airborne stereographic photography or a wave tilt buoy containing a compass as a directional reference (Shearman, 1981). However, since the received HF radar signal is proportional to the wave energy moving radially towards and away from the radar receiving antenna, the reverse of equation [2] gives a measure of $G(\theta, u)$, given that a steady-state, fully developed sea exists ( $S_0(f_w, u)$ is constant ). If a correct model relating the directional factor and the reference angle, $\theta$ (the angle of the wind relative to the observed wave direction, which is determined by the radar look direction due to Bragg scattering), is known, then the wind direction can be measured.

9

## 1. Models Relating the Directional Spectrum to the Mean Wind Direction

### a. Cardioid Model

Models for a functional relationship between the directional spectrum $G(\theta, u)$ and the wave (and mean wind) direction are determined empirically. Munk (Tyler et al., 1974) fit measured spectra with the expression:

$$G(\theta, u) = \left[ \varepsilon + (1-\varepsilon) cos^s\left(\theta/2\right) \right] \qquad [4]$$

where s, the directional spreading parameter, is a function of u and L. The factor $\varepsilon$ was included by Munk to take into account consistent radar oceanographic evidence of up-wind wave propagation. Steward and Barnum (1975) set $\varepsilon = 0$ and define the ratio of approaching to receding waves by the expression:

$$R_b = \frac{G(\theta)}{G(\theta + \pi)} = tan^s\ (\theta/2) \qquad [5]$$

where $R_b$, hereafter called the Bragg ratio, is the difference between the positive (approaching) and negative (receding) Bragg peak power levels (in dB). Inverting equation [5] yields:

$$\theta = 2\ arctan(R_b^{1/s}) \qquad [6]$$

Figure 3 illustrates this cardioid model. The relative strength of the Bragg peaks determine the orientation of the cardioid and solves the wind direction relative to the

radar look direction. If the peaks are equal in strength, the Bragg ratio equals one, and the waves (and wind) are moving perpendicular to the radar azimuth.

In Tyler et al. (1974) the spreading parameter s is plotted vs. a parameter $\mu$ which characterizes the momentum transfer from the wind to the waves. A drag coefficient $C_D$ is assumed to relate the wind speed to the ocean wave speed c:

$$\mu = \sqrt{C_D} \frac{U}{(\kappa c)} \qquad [7]$$

where $\kappa = 0.4$ is von Karman's constant. Stewart and Barnum (1975) assume values for the drag coefficient based on Wu (1969): $C_D = 5 \times 10^{-4} U^{1/2}$ for $U < 15$ m s$^{-1}$ and $C_D = 2.6 \times 10^{-3} U$ for $U > 15$ m s$^{-1}$. The corresponding expressions for $\mu$ are given by:

$$\mu = 3.65 \times 10^{-3} U^{5/4} f_r^{1/2}, \quad U < 15 \, ms^{-1}$$
$$\mu = 8.33 \times 10^{-3} U \; f_r^{1/2}, \quad U > 15 ms^{-1} \qquad [8]$$

where $f_r$ is the frequency of the radar in MHz. Tyler et al. (1974) found a good fit of s($\mu$) by:

$$s = 0.4(\mu - 0.1)^{-1}, \quad \mu > 0.1$$
$$s = 4.0, \quad\quad\quad\;\; \mu < 0.1 \qquad [9]$$

Table 1 lists values of the spreading parameter for various wind speeds and frequencies of the MCR used in this study. A higher value of the spreading parameter means that there is more departure from the normal direction for a given Bragg ratio. In other words, greater values of s increase the model's sensitivity to the directional spectrum.

11

**TABLE 1.** Range of Wave Spreading Parameters Based on the Algorithm of Steward and Barnum (1975)

| Wind Speed (m s$^{-1}$) | Radar Freq. (MHz) | $\mu$ Parameter | Spreading Parameter, s |
|---|---|---|---|
| 5.0 | 4.8 | 0.0598 | 4.0 |
| 5.0 | 6.8 | 0.0712 | 4.0 |
| 5.0 | 13.3 | 0.0995 | 4.0 |
| 5.0 | 21.8 | 0.1274 | 14.5885 |
| 10.0 | 4.8 | 0.1422 | 9.4777 |
| 10.0 | 6.8 | 0.1693 | 5.7756 |
| 10.0 | 13.3 | 0.2367 | 2.9259 |
| 10.0 | 21.8 | 0.3031 | 1.9699 |

### b. *Log-Cosine Model*

A second model to relate the directional spectrum and the wind direction is presented in Long and Trizna (1973) and used by Ahern (1974). Here the directional spectrum is a function of frequency as well as wind speed and direction. The directional component (from Long and Trizna equation (5) that is based on the spectrum of Pierson et al. {1966}) is given by:

$$F(\omega,\theta,u) = (\tfrac{1}{\pi})\{\gamma + 0.50 + 0.82\,exp\,[-\tfrac{1}{2}(\tfrac{\omega_0}{\omega})^4]\,cos\,2\theta$$
$$+\,0.32\,exp\,[-\tfrac{1}{2}(\tfrac{\omega_0}{\omega})^4]\,cos\,4\theta \qquad [10]$$

where $\omega$ is angular frequency of the sea components, $\omega_0 = g\,v^{-1}$ (v is the wind speed at 19.5 m above the sea surface) and $\gamma$ is a constant fitted from data. The Bragg ratio is then related by:

$$R_b = 20\log F(\theta) + r_0 \qquad [11]$$

where $r_0$ is a constant fitted to the data. The authors found to good approximation for

sky-wave radar frequencies (15 – 18 MHz) that equation [10] can be simplified to:

$$F(\theta) = (\tfrac{1}{\pi})(\gamma + 0.5\cos 2\theta) \qquad [12]$$

for $\theta \le \pi/2$. Long and Trizna determine the constants $r_0$ and $\gamma$ directly from the sky-wave

data. It is assumed that the largest value of $R_b$ was obtained from illumination parallel to

the wind (based on measurement by in-situ observations) and $R_b$ must be zero for wind

perpendicular to the radar look direction. The data (collected during a North Atlantic

storm) showed that $r_0 = 24.6$ dB for winds blowing parallel to the radar look direction.

Substituting these values into equations [11] and [12] yields the model of Long and

Trizna (1973):

$$R_b(\theta) = 20\log[(\tfrac{1}{\pi})(0.56 + \tfrac{1}{2}\cos 2\theta)] + 34.02\,\text{dB} \qquad [13]$$

or inverted for $\theta(R_b)$:

$$\theta(R_b) = \frac{1}{2}a\cos\left[2\pi 10^{\left(\frac{R_b - 34.02}{20}\right)} + 0.56\right] \qquad [14]$$

#### c.    *Linear Model*

Another model used in a more recent study is that proposed by Georges et

al. (1993). They acknowledge that $G(\theta)$ is not well known and depends not only on wind

speed, but also on fetch, duration, and ocean wavelength. For their study of tracking a

hurricane over-the-horizon using sky-wave propagation of HF radar, they assume a

13

simple linear relationship that lies between those derived by Long and Trizna (1973) and Stewart and Barnum (1975):

$$\theta(R_b) = \pm \frac{\pi}{2}\left(\frac{24 - R_b}{24}\right), \quad -24\,\text{dB} < R_b < 24\,\text{dB} \qquad [15]$$

For $R_b \geq 24$ dB the wind angle $\theta$ is 0° (wind directly towards radar), and for $R_b \leq -24$ the wind angle is 180° (wind directly away from radar). The cutoff value of 24 dB is taken from the empirical results of Long and Trizna (1973).

Figure 4 illustrates the difference between the three models discussed with respect to positive Bragg ratios (wind towards radar). The models are very similar for small Bragg ratios, but diverge for values greater than 5 dB. The linear equation of Georges et al. and the cardioid model of Stewart and Barnum are close for Bragg ratios up to 15 dB, while the model of Long and Trizna can be as much as 20° greater (more anti-parallel) for a similar ratio. Both the linear and long linear model account for observed winds directly towards or away from the radar, whereas the cardioid model requires very large ratios (beyond the dynamic range of the summer 1997 MCR data) to achieve near-zero relative wind angles. Since all of these models were applied to sky-wave propagation, this study will examine which of these models gives the best results for the ground-wave data set used here.

## 2. Solution Ambiguity

The solution of the wind direction for a given Bragg ratio is not unique. There is a left-right ambiguity in all models due to HF radar's inability to distinguish the

perpendicular component of waves moving in either cross direction to the radar look direction. A Bragg ratio yielding a wind angle of 30° implies that the wind is blowing 30° left or right of the radar look direction. Thus, some other means of independent measurement of the wind at (or near) the location of radar illumination is required to resolve this right-left ambiguity. In-situ observations, synoptic or mesoscale weather charts, or satellite measurements will resolve the solution, but measurements from another HF radar site ideally resolves the ambiguity at many range azimuth cells within the coverage area of each radar.

### 3.    Wind Duration and Fetch

The growth and decay of radar-resonant waves as a function of wind speed, fetch and duration are likely to have a significant impact on the wind retrieval algorithm (Vesecky et al., 1998). Specifically, how long of wind duration and how large of fetch is sufficient for a given body of water to produce equilibrium conditions required to apply the HF wind models presented above. Kinsman (1965) describes the conditions required for a fully developed sea. The sea is either fetch-limited or duration-limited, depending on whether the fetch or the duration imposes the greater restriction on the growth of the waves. According to theory, for a fetch-limited condition the wind duration is long enough to allow the waves to reach maximum height for the given (constant) wind speed. The empirically supported theory of Sverdrup and Munk (1947) suggests fetch of 7 to 10 km for MCR resonant ocean waves (Vesecky et al. 1998). For a 5 m/s wind the fetch requirement increases to 14 km for the shortest resonant waves, while the longest

resonant waves cannot be generated directly because their phase speed is 1.4 times the wind speed.

For a duration-limited condition (i.e. the wind has unlimited area in which to act on the sea surface), Vesecky et al. (1998) cite the growth times approximated by Phillips (1981) neglecting dissipation:

$$T_{growth} \approx 3\left(\frac{c_w}{U*}\right)^2 \qquad [16]$$

where $T_{growth}$ is the growth time in wave periods, $c_w$ is the wave phase speed and $U*$ is the mean wind speed. For a 10 m/s wind e-folding growth times ranging from 11 minutes to 108 minutes can be expected for the four resonant waves of the MCR. Assuming equilibrium at 3-5 e-folding times, fully developed conditions would be expected on the order of a hour for the lower frequencies and many hours for the highest frequency. In order to distinguish a fetch-limited or duration-limited condition for coastal radar-resonant waves, factors such as shoreline geometry, wind direction relative to the coastline, and wind duration must be assessed. The next section will address these conditions in Monterey Bay.

## 4.    Wind Duration and Fetch Conditions in Monterey Bay

The general wind duration and fetch conditions during the summer season can be characterized by examining the geometry of Monterey Bay, the predominate synoptic pattern and the diurnal sea-land circulation. First, the westward-facing, semi-circular geometry of Monterey Bay is such that wind flowing from directions ranging from the

south to the northwest are unimpeded by land and have nearly unlimited fetch. Winds from directions of northwesterly to south-southeasterly flow offshore from mountainous terrain, except winds from the easterly direction that flow from the flat Salinas River Valley. Offshore winds would require extended duration (~ days) to generate radar-resonant waves over the limited area of Monterey Bay.

The summertime meteorological synoptic conditions in Monterey Bay are dominated by the Eastern North Pacific high pressure system and strong thermally-induced low pressure system over the southwestern United States. These two features result in quasi-stationary, prolonged northwesterly synoptic flow along the coast of California. The mean oceanic wind speed ranges from 10 to 15 m s$^{-1}$. Although small deviations of this flow occur due to changes in the strength and position of the seaward high pressure cell and the thermal trough axis in central California, the large fetch (~ 500 km) and long duration (~ 3-5 days) of the synoptic flow generate ocean swell with wavelengths typically longer than those sensed by the MCR. The longest wavelength sensed by the MCR, 31.2 m, is, however, in the range of the swell wavelengths and may, therefore, be expected to produce results that differ from the other three sensed wavelengths that are resonant with locally generated waves.

From the perspective of HF radar, the dominate effect on fetch and wind duration in Monterey Bay is the thermally-induced sea-land circulation. Foster (1993) analyzes the diurnal sea breeze cycle in Monterey Bay based on land and mooring data collected during September 1992. The directional response of wind sensors at offshore moorings indicate that the temporal scale of the onshore sea breeze roughly coincides with the

17

required wind duration computed above. Thus, the wind duration appears to be the limiting factor during typical sea breeze conditions for the generation of radar-resonant waves. If the sea breeze cycle is shorter or too weak to produce organized onshore flow, radar-resonant waves would not be expected to be well developed, and the radar derived wind direction would suffer. Likewise, during land breeze or other offshore flow conditions, the limited fetch would inhibit the growth of resonant waves and reduce the effectiveness of the radar.
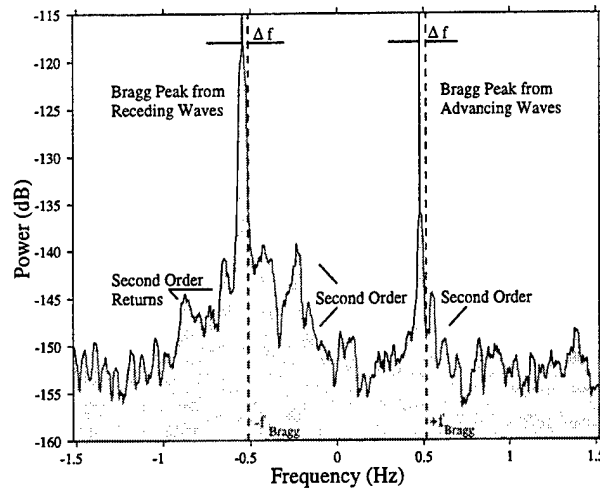
**Figure 1.** Sample backscatter spectrum showing prominent Bragg peaks due to wind-waves advancing toward and receding from the receiver. The Doppler shifts, $\Delta f$, from the Bragg frequencies, $\pm f_{bragg}$, are due to ocean currents. (Adapted from Paduan and Graber, 1997).
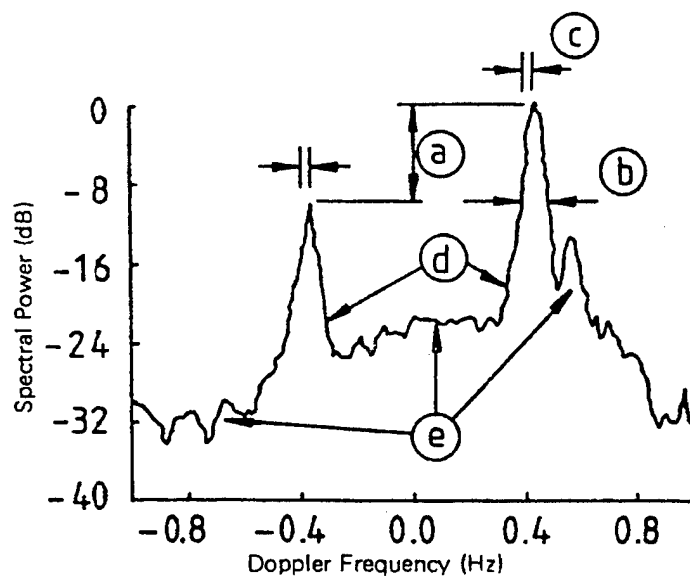


**Figure 2.** Air-ocean parameters estimated from HF radar spectra: (a) ratio of two first-order Bragg lines - wind direction; (b) -10 dB width of larger Bragg peak - wind speed; (c) Doppler shift of first-order Bragg lines from expected values - radial component of surface current; (d) magnitudes of first order Bragg lines - ocean wave height spectrum for one wave-frequency and direction; (e) magnitude of second order structure - ocean wave height spectrum for all wave-frequencies and directions. (Adapted from Shearman, 1981).

19
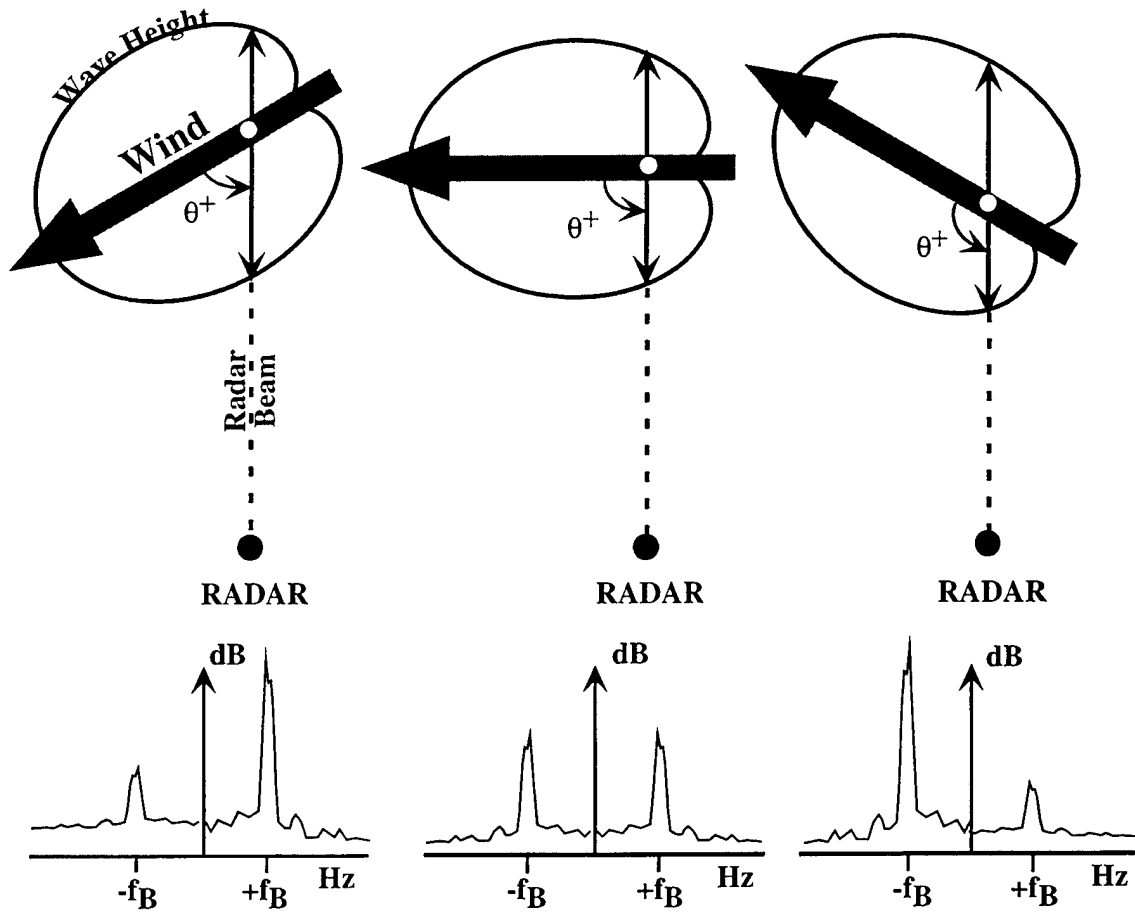
**Figure 3.** Sample cardioid distributions of surface energy as a function of angle relative to the wind for cases with wind blowing toward (left), perpendicular (middle) and away from (right) the radar look direction. Sample backscatter spectra below each case show the relative heights of the approaching (+) and receding (-) Bragg peaks required for each cardioid solution. The angle $\theta_+$ denotes the angular difference between the wind and the radar look direction, which is identical to the approaching wave direction.
(Adapted from Fernandez, et al., 1997).
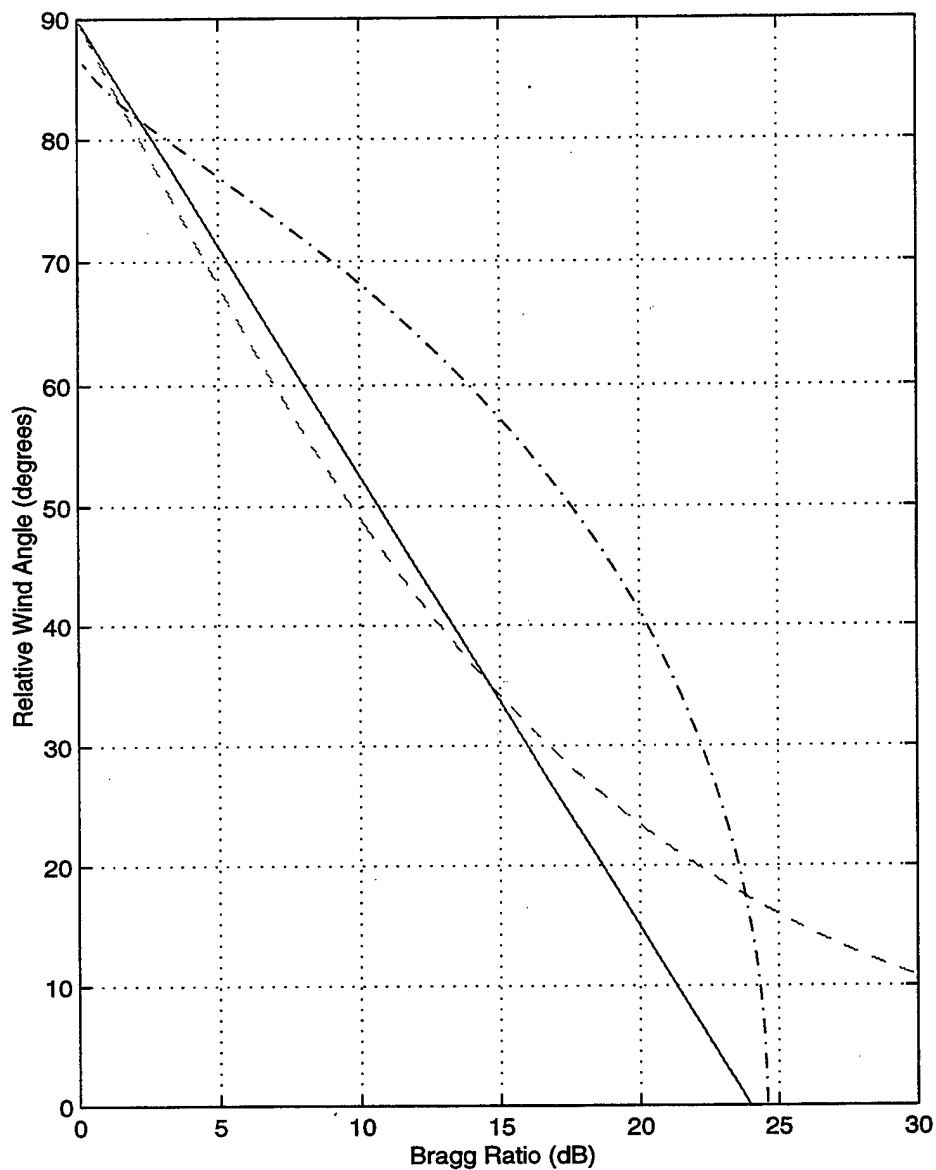
**Figure 4.** Relative wind angle as a function of positive Bragg ratio for three models: linear (Georges et al., 1993) [solid]; cardioid (Stewart and Barnum, 1975) [dashed]; and log-cosine (Long and Trinza, 1973) [dashed-dot]. A positive wind angle is defined as the radar-derived wind direction measured to the left or right of the radar beam direction towards the radar. Negative Bragg ratios produce wind angles measured from the beam direction away from the radar.

21

# III. DATA AND METHODS

## A. MULTI-FREQUENCY COASTAL (MCR) HF RADAR

### 1. System Description

The newly developed Multi-Frequency Coastal Radar (MCR) is a phased-array system using vertical transmit antennas and a linear array of eight wideband-loop-receive antennas spaced 6 m apart for an aperture of 48 m. Figure 5 is a photograph of the radar installed at the Long Marine Laboratory of the University of Santa Cruz (UCSC) on the northern side of Monterey Bay. A second identical site was installed at the Moss Landing Marine Laboratory on the eastern edge of Monterey Bay (Figure 5). Table 2 lists the physical attributes the radar's four channels.

**TABLE 2.**    MCR Radar Parameters

| Channel | Frequency (MHz) | Resonant Ocean Wavelength (m) | Effective Depth (m) |
|---------|-----------------|-------------------------------|---------------------|
| 1 | 4.8 | 31.2 | 1.4 |
| 2 | 6.8 | 22.0 | 1.0 |
| 3 | 13.4 | 11.1 | 0.5 |
| 4 | 21.8 | 7.0 | 0.3 |

The last column of Table 2 is the effective depth of the surface current according to theory by Ha (1979).

The range of the radars is about 40 to 50 km, depending on the wave height. Range can be increased by increasing the peak transmit power from the current value of 30 W, although the effective transmitted power will be lower and the propagation loss will be greater for higher frequencies. The range resolution is about 3 km, and the angular resolution is approximately 15° based on the receiving array's aperture, which is optimized for channel four. The measured spectrum of each range-azimuth bin is actually a temporal and spatial average over a patch of sea surface for that bin that ranges in area from 1 to 25 $km^2$. Each radar transmits continuously for approximately 12 minutes (required time to digitally record samples from each receiving element) each hour. The Santa Cruz site begins its transmission at the top of the hour, while the Moss Landing site transmits 17 minutes later to prevent interference with the Santa Cruz system. The hourly records from each site are then saved to electronic media (CD-ROM or magnetic disk) for additional processing. Further description of the radar's design and operation is given in Teague et al. (1997).

## 2. Spectrum Generation by Beam Formation

The recorded signal at each receiver element is coherently summed to electronically "steer" the phased-array radar beam and measure the entire Bragg spectrum for each range-azimuth cell. Using personal computer-based processing, optimum beam weights for each receiving element were first calculated for each radar look direction and frequency. At the lower frequencies beam formation produces Doppler spectra that average over large look angles. The undesirable artifacts of the beam formation

technique are side lobes (Figure 6) which decrease the directivity of the radar's steered beam. Side lobes are unavoidable and occur for every steering direction and every frequency. They are small for look directions near normal (or "broadside") to the receiving array, but are most problematic for large steering angles (angles greater than about 45° from broadside). To minimize side lobes, an iterative algorithm (created by Jason Diada of University of Michigan) optimizes the beam formation by (1) not steering the array all the way to the intended direction and/or (2) attenuating the entire pattern and subsequently weighting the main lobe and side lobe towards an average of the two. In an effort to over-sample the domain, the algorithm was set up to compute beam weights for azimuths every 5° ranging from -50° to +50° from the radar broadside.

The time series was then corrected and normalized for slight differences in the preamplifiers used at each receiver element . A fast Fourier transform was then applied. Individual transforms are weighted and summed to steer a beam in a desired direction. Further processing results in the power density spectrum for each range-azimuth cell. Figure 7 is an example of a power spectrum produced for a given range-azimuth cell and time. The power levels (in dB) of the positive and negative Bragg peak as well as the noise levels were determined and recorded from the spectra. Additionally, the Doppler frequency and corresponding currents are computed via a two-stage centroid search. The output of the this processing was then recorded in netCDF format to facilitate further processing. The first range cell is 3 km from the radar, and a total of 15 range cells were computed resulting in an effective radar range of approximately 45 km for each site. Figure 8 shows the radial coverage patterns of the two sites.

## B.    WIND RETRIEVAL ALGORITHM

Once the peak Bragg power levels and noise levels were known for all range-azimuth cells for a particular hour from each site, the HF radar-derived wind field were determined. The first range cell was discarded since it is overloaded by the transmit signal (personal correspondence with C. Teague of Stanford University). The coverage areas of the two radar sites were first compared, and all data in areas that do not overlap was disregarded. The overlap area did not extend over land, so no corrections were needed for over-land observations. The Bragg ratio was then computed by simply subtracting the positive and negative peak power levels. The signal-to-noise ratio (SNR) levels were also computed for the positive and negative sides of the spectrum. If both the peak levels were not above a specified threshold greater than the noise level (which is generally the same for both sides of the spectrum) then the wind calculation was disregarded for that cell. For all the remaining cells, the wind angle relative to the radar look direction was calculated depending on which of the three models presented above (equations [6], [14] or [15]) was used. Each model results in a left and right solution of the wind angle. The wind angle was then converted to east-west (u) and north-south (v) unit-length components since the radar solution gives direction only, not speed. Figures 9 and 10 are examples of the two solutions for each site.

The radially-spaced solutions of each site were then mapped to a 3-km Cartesian grid (Figure 11) to reduce the bias of the look direction on the solution. For each Cartesian grid point, all the radial-space cells from each site within a search radius

(nominally 3 km) were determined. If there were only two points from a particular site, then the wind calculation was not done at that grid point. This condition reduces spurious solutions along the boundaries of the domain. The mean of all the solutions from each site (i.e. all the Santa Cruz "left" solutions, all the Santa Cruz "right" solutions, and so on) within the search radius and average SNR were then calculated. Rather than match up single radial cells from one radar site with a cell from the other site as was done by Vesecky et al. (1998) to resolve the ambiguity of the two solutions, the mean solutions of each site were compared to determine which solution combination best resolves the ambiguity and maintains realistic continuity of the wind direction. For a two-site geometry, this yields four possible pairs of solutions: $L_1L_1$, $R_1R_2$, $L_1R_2$ and $R_1L_2$, where the left solution is denoted by L and the right solution is denoted by R, and the subscripts refer to the radar site. The smallest angular difference was then chosen of these four combinations. The final solution was then chosen based on higher average SNR between the two sites at that grid point in recognition of the fact that direction estimates from radar sites looking more nearly upwind or downwind, or from closer range cells are bound to be better than estimates from radar sites looking nearly crosswind or at large range. Wind maps using this algorithm can be found in section IV.

## C.    AVAILABLE OBSERVATIONS

### 1.    MCR Data for Summer 1997

Figure 12(a) shows the data time coverage of each MCR when data was successfully processed (spectrum formation) from the period 19 June to 20 August 1997. The gaps in coverage were primarily caused by radar support system malfunctions or data recording errors. Some files (approximately 110 total for each channel from both sites) failed to process due to data format errors or partial time-series records. The disparity in the number of files between the middle two channels and channels 1 and 4 is due to apparent problems extracting the time series records from the CD-ROM disks. Figures 13 and 14 display the hourly coverage of each channel when data was concurrently available (roughly 750 hourly measurements) from both sites in order to resolve the solution ambiguity in the wind retrieval algorithm.

### 2.    In-situ Observations

In-situ wind observations were collected for the 60-day period of 21 June to 19 August 1997 from three different sites to compare to the radar-derived wind results. The single afloat measurement used is the mooring called M1, which is operated by the Monterey Bay Aquarium Research Institute (MBARI). It is located at approximately 36.75° North and 122.04° West (Figure 5) and has an anemometer height of 3.8 m. The hourly-averaged preprocessed mooring data was extracted from the MBARI OASIS

28

database and gross-error checked for continuity. Since the mooring position is well within the coverage area of the two MCR sites, wind observations from that site provide independent ground truth for the radar-based winds in this study. The times of available wind observations from the M1 mooring site are shown in Figure 12(b) for comparison with the available MCR data. Gaps in the observation data are due to missing or unusable values.

Land observations were also collected to roughly assess the spatial variability of the surface wind field around Monterey Bay. The first of two land stations used was the automated observation station located at the Long Marine Research Laboratory at the University of California at Santa Cruz (UCSC). The second land measurement station is located at MBARI near the Moss Landing Marine Laboratory in Moss Landing. Each of these sites are co-located with the Santa Cruz and Moss Landing MCR sites. The data from these two stations were recorded at 10-second resolution by the Real-time Environmental Information Network and Analysis System (REINAS). The data was extracted from REINAS, quality checked and averaged to hourly intervals. Figure 12(b) displays the temporal coverage of the two land stations during the experiment period.

## 3.    Summer 1997 Synopsis

All of the hourly observations from each of the three in-situ stations during the 60-day period of 1997 are plotted in Figure 15. Each observation has been decomposed into north-south (u) and east-west (v) components in m s$^{-1}$. The ticks on the time axis mark midnight GMT. Immediately evident in all three panels are the diurnal fluctuations

29

of both u and v associated with the sea breeze circulation in Monterey Bay. The daily peaks in u correspond to the mature sea breeze when the synoptic flow and onshore thermal surface circulation combine to maximize the eastward flow during the afternoon and evening hours. Each peak occurs during these hours each day, and the magnitudes are larger at Santa Cruz and the M1 mooring than at Moss Landing. The smaller eastward and larger southward components at Moss Landing indicate the strong tendency for the sea breeze to align with the inland valley. During the nighttime hours, both components drop off to near zero at the land stations due to breakdown of the thermal forcing and land breeze reversal, while weak flow sustains at M1 due to the dominate influence of the synoptic scale pattern on the seaward location. At M1 there was more day-to-day variation of each component compared to the land stations which implies that subtle changes synoptic pattern are most evident over water.

During the first quarter of the period, the peak wind speeds were generally over 5 m s$^{-1}$ during the mature sea breeze, while morning magnitudes were near zero. There were consistent southwestward flow (positive u and negative v) at the mooring, pronounced eastward flow at Santa Cruz and weaker southward flow at Moss Landing. These observations are consistent with the classic sea breeze described and analyzed during September 1992 by Foster (1993) which indicated a clockwise rotation of the wind from eastward over the outer portion of Monterey Bay to southeastward over the inner coastal portion as winds align with the inland valley during onset of maximum sea breeze, which usually occurs at approximately 1500 local time. Although there was about a 7-m s$^{-1}$ daily fluctuation in wind speed, the sustained southeastward flow during the

evening hours had longer duration than any other segment and, thus, presents the best possibility for fully developed seas during the two-month study period.

During middle and late July, the sea breeze signature was still present, but the wind magnitude was generally much weaker (less than 5 m s$^{-1}$) and eastward in direction. In early August, the winds again increase in magnitude and shift towards the southeast. However, from about the 7$^{th}$ to the 10$^{th}$ and again on the 16$^{th}$ and 17$^{th}$, the wind direction shifts towards the north (v positive) at both the mooring and Santa Cruz due to synoptic-scale offshore flow. Unfortunately, measurements from nearby NOAA buoy 46042 were not available during this time to verify the extent of this reversal. The flow is northwestward even at M1. The magnitude of the wind during this shift is not overly strong, but the flow does sustain for about three days, which would be sufficient time to develop wind-driven gravity waves with a northwestward tendency, or at least, substantially offset any residual southeastward propagating waves. However, limited fetch likely restricts the growth of radar-resonant waves and prevents a fully developed sea. Although there is no wind shift observed in the Moss Landing v component, there is a clear perturbance in the eastward (u) component during and immediately after the return to normal southeastward flow on the 10$^{th}$. The output of the MCR during this wind reversal episode will be examined later.
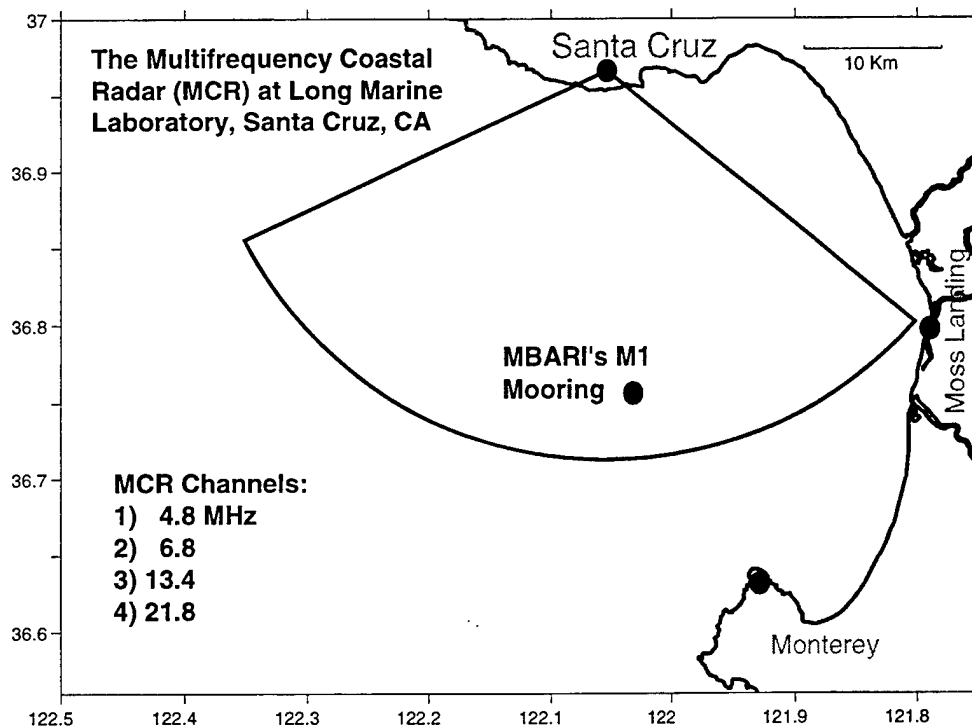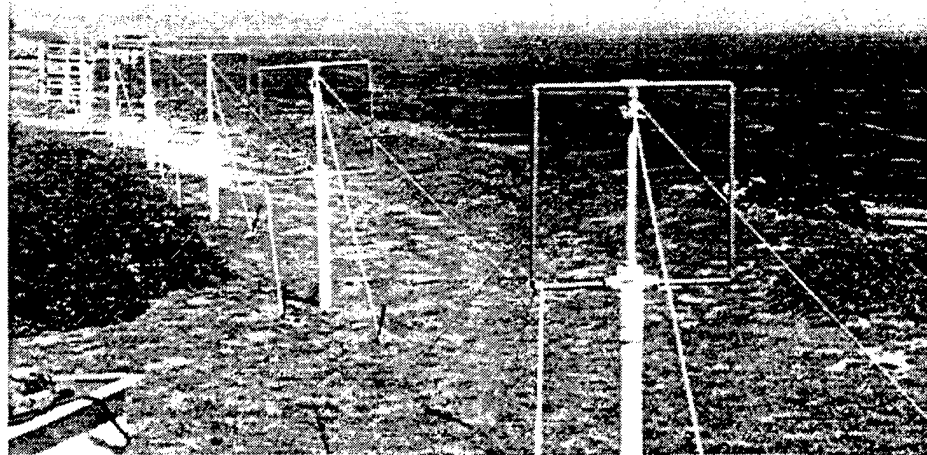
**Figure 5.** Photograph of the eight loop antennas of the receiving array at the Santa Cruz MCR site. A vertical transmitting antenna is located to the left of the array, outside the view of the photograph (top). Schematic diagram showing the position and coverage area of the Santa Cruz MCR to a range of 30 km (bottom). The Moss Landing MCR has similar coverage area (not shown) extending from its site. The actual range used in this study was approximately 45 km. The position of the MBARI M1 mooring is also marked.
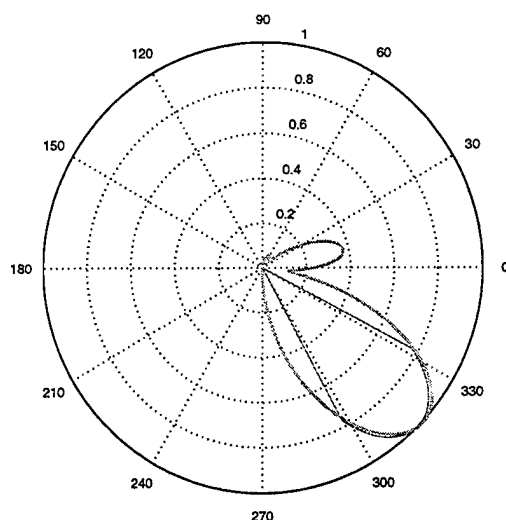
**Figure 6.** Example of HF radar side lobes for a look direction of 45° right of radar broadside (0°) as optimized by the beam weight algorithm for channel 2 (6.8 MHz). The solid line indicates an ideal beam pattern.
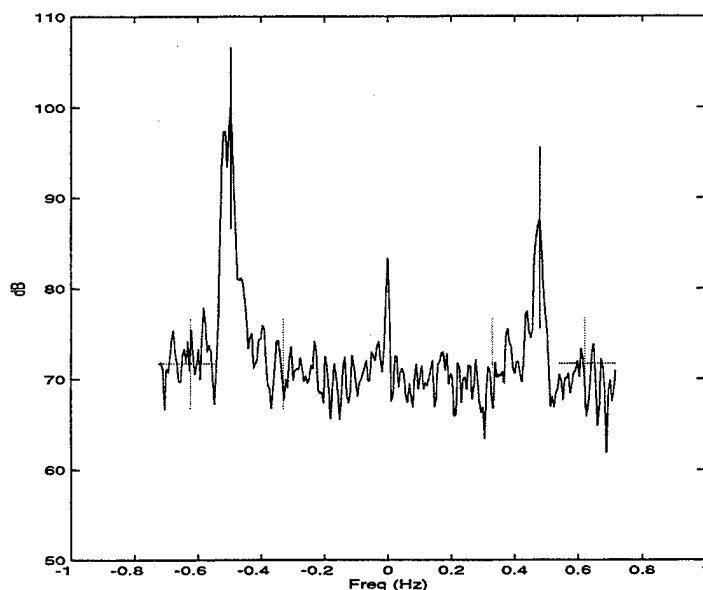


**Figure 7.** Sample MCR output spectrum for a range-azimuth cell (Santa Cruz channel 4, 3rd range bin, and 45° left of broadside, in this case). The expected Doppler shift (long vertical line in each Bragg peak), computed noise floor (short horizontal line on each side) and noise level ± 5 dB (short vertical lines embedded in the higher-order return) are displayed. The peak located at 0 frequency shift is due to radar echo from land.

33
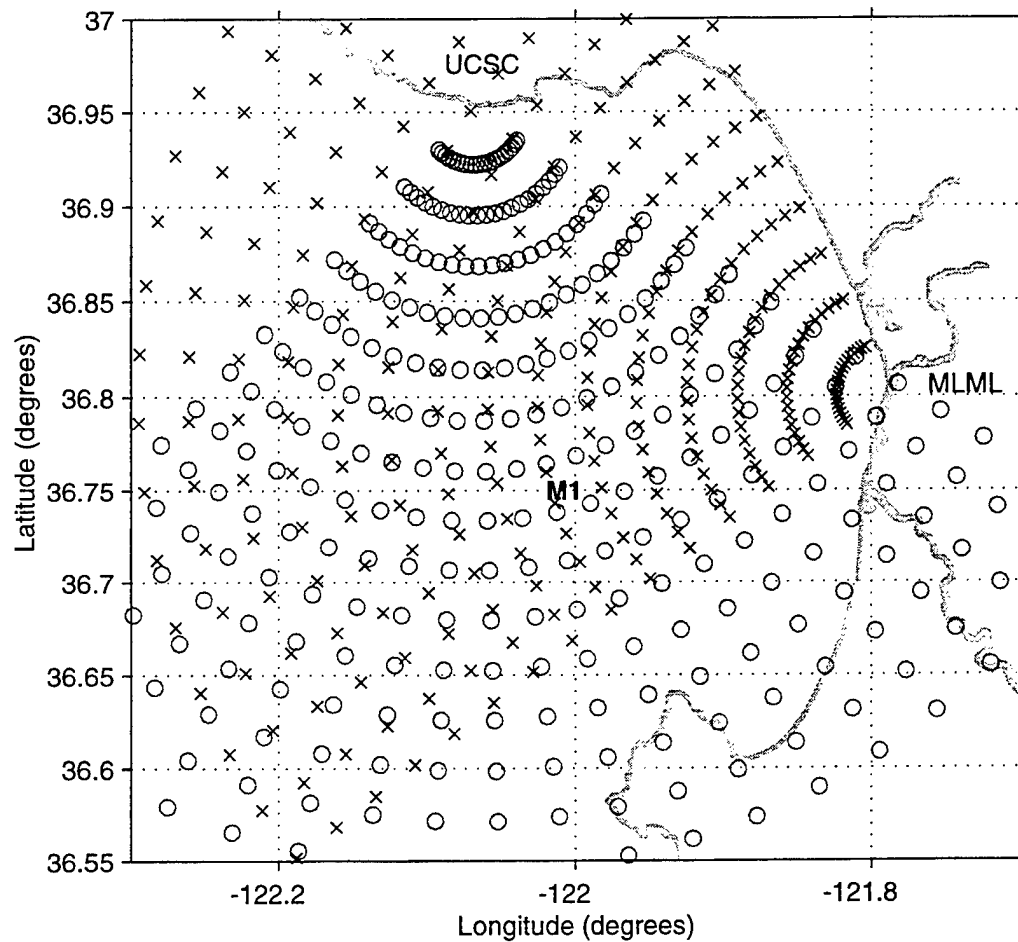
**Figure 8.** Radial coverage patterns computed for this study for the Santa Cruz (o) and Moss Landing (x) MCR. The radials are spaced every 5° and the range bins are spaced every 3 km.
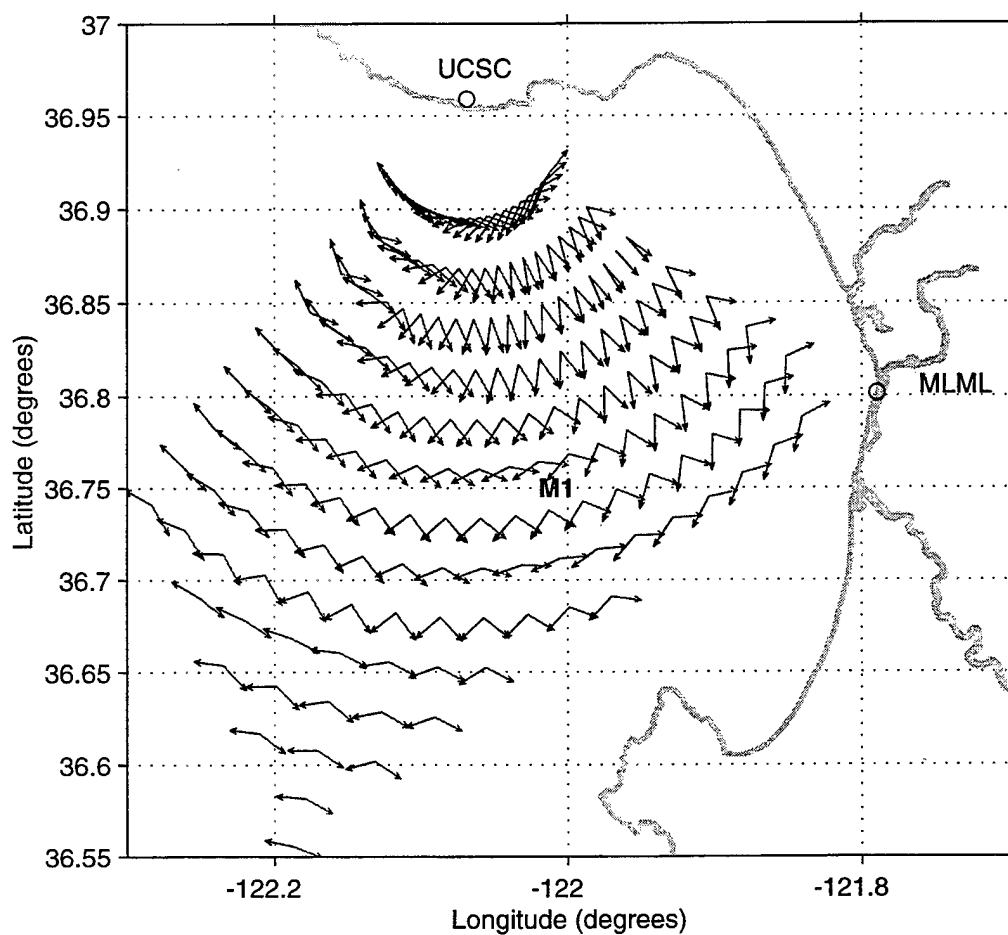
**Figure 9.** Example of Santa Cruz left and right solutions of the radar-derived wind direction. Solutions are computed only where there is overlap with the Moss Landing MCR coverage area. The positions of MCR sites and mooring M1 are also marked.
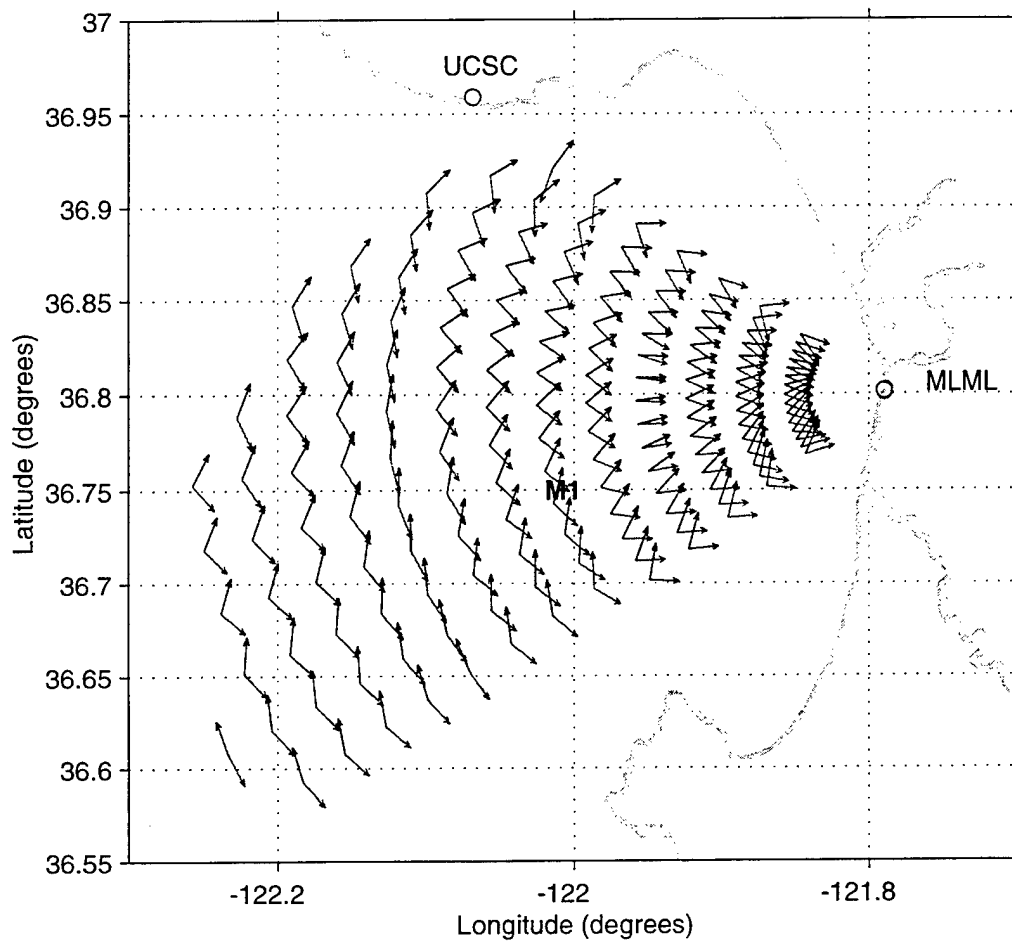
**Figure 10.** Example of Moss Landing left and right solutions of the radar-derived wind direction. Solutions are computed only where there is overlap with the Moss Landing MCR coverage area. Points with a single arrow imply that the Bragg ratio is large and, hence, the radar-derived wind direction coincides with the radar look direction.

36
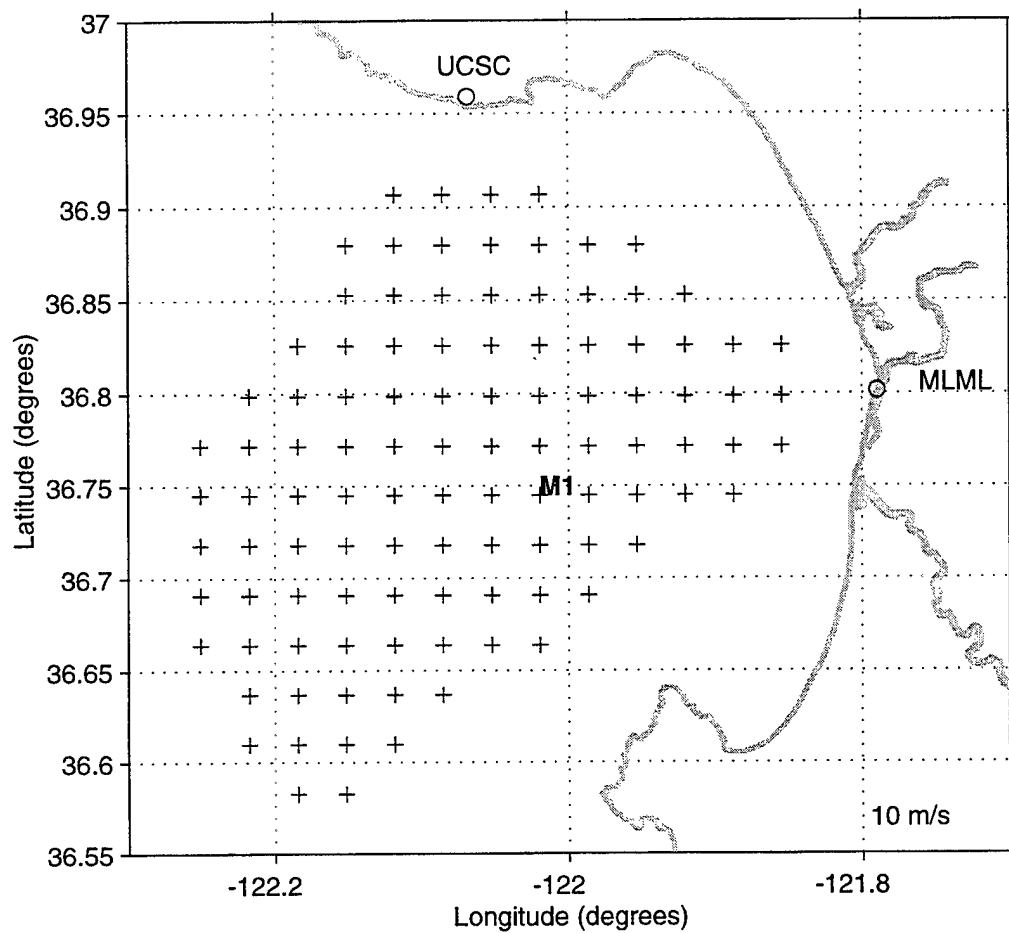
**Figure 11.** 3-km Cartesian grid used in the wind retrieval algorithm.
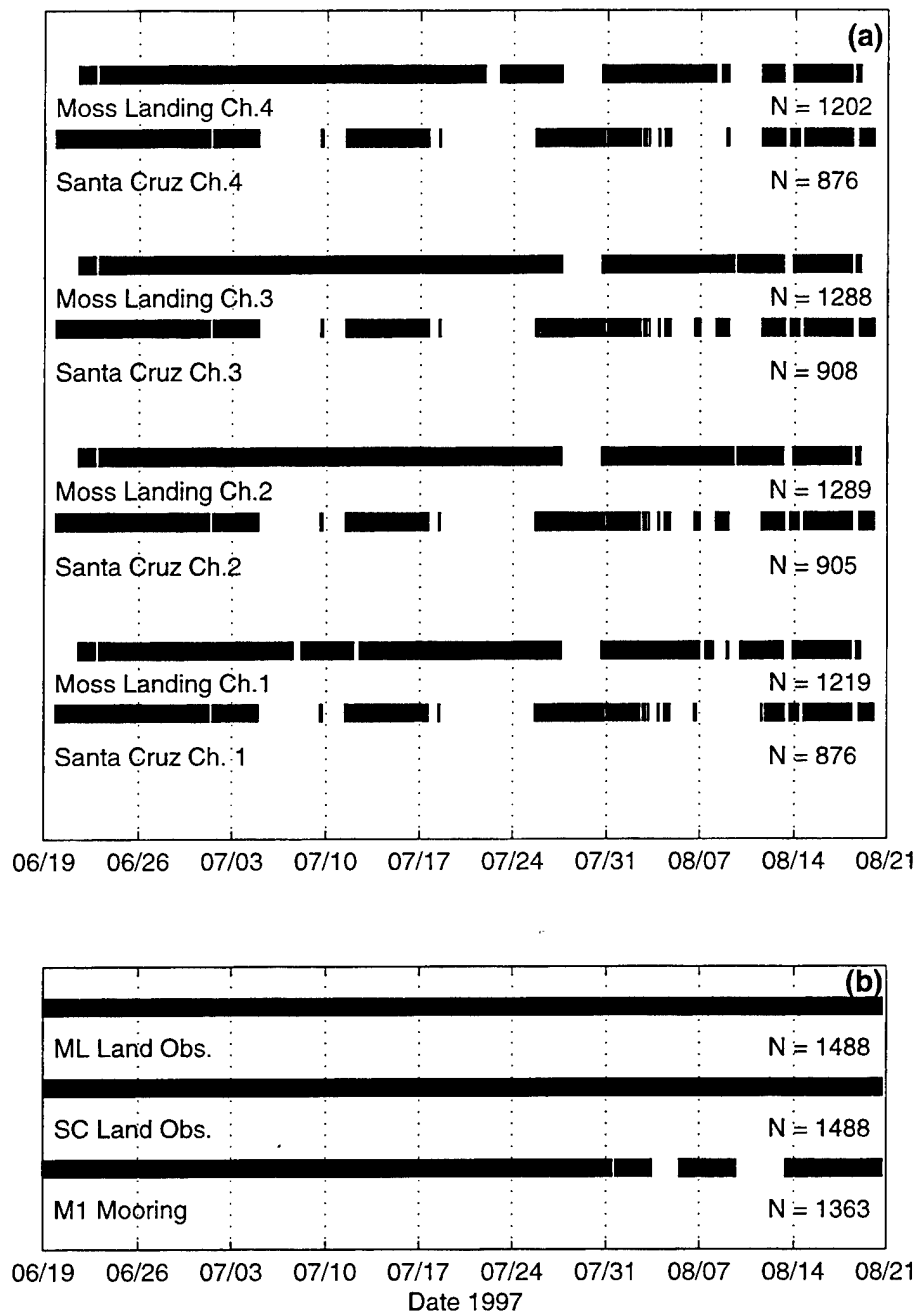
**Figure 12.** Bar graphs indicating times when usable data was available from the MCR systems (a) and in-situ observations (b) during summer 1997. Each site and channel are denoted below each bar. The values on the far right indicate the number of hourly measurements available during the period out of 1,488 total possible hours.
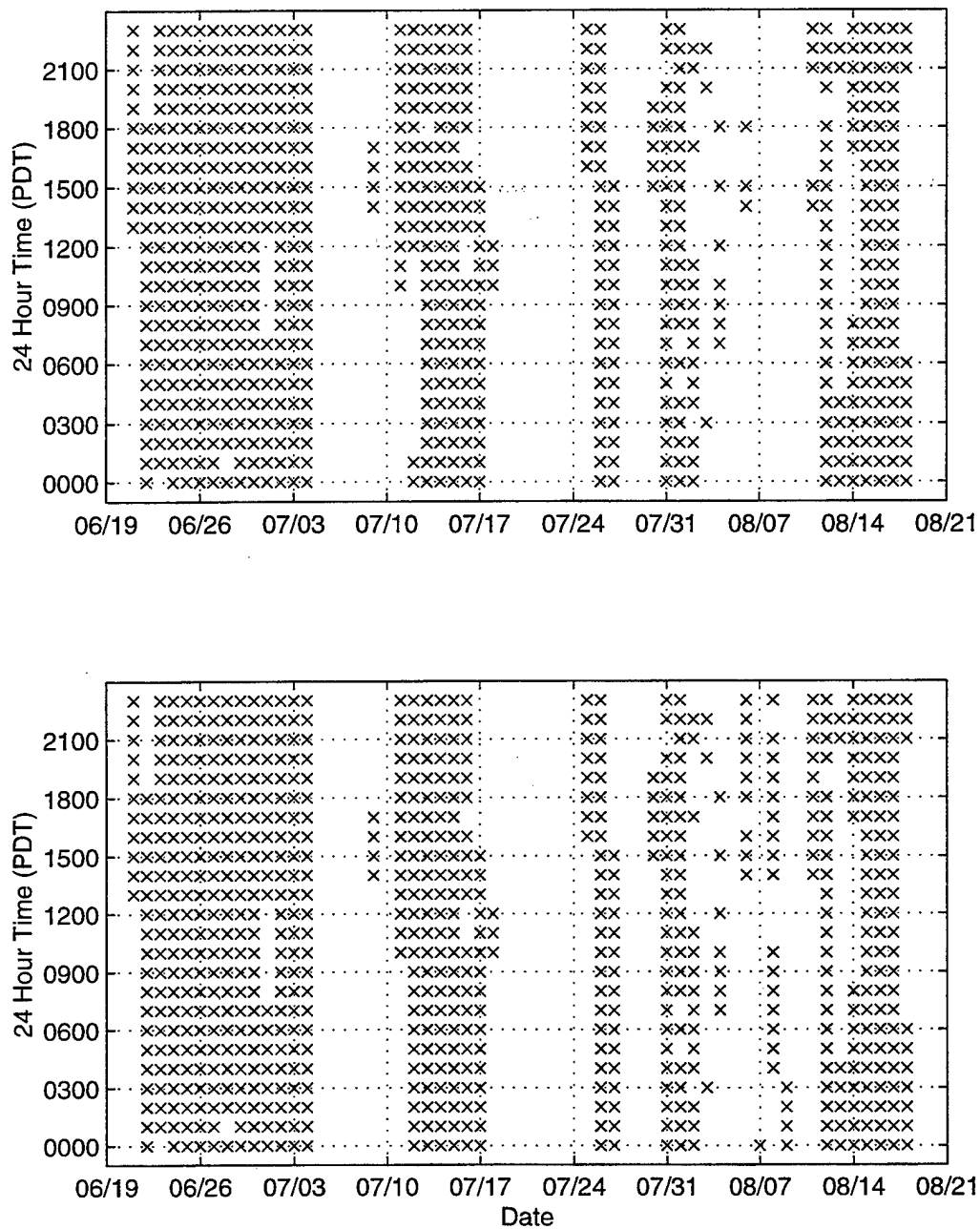
**Figure 13.** Listing by hour when usable data was concurrently available from both MCR sites during summer 1997 for channel 1 (top) and channel 2 (bottom).
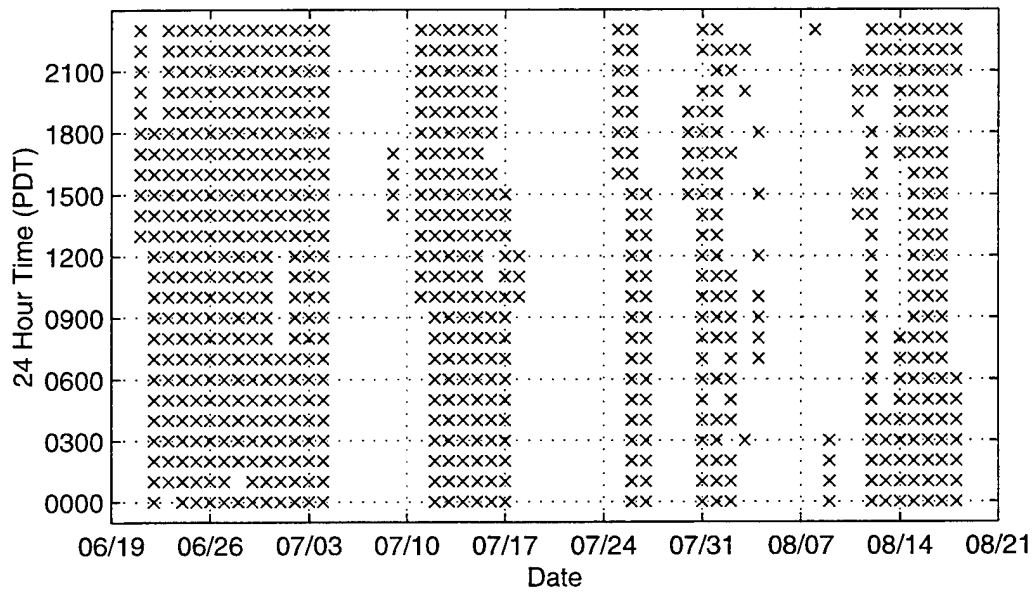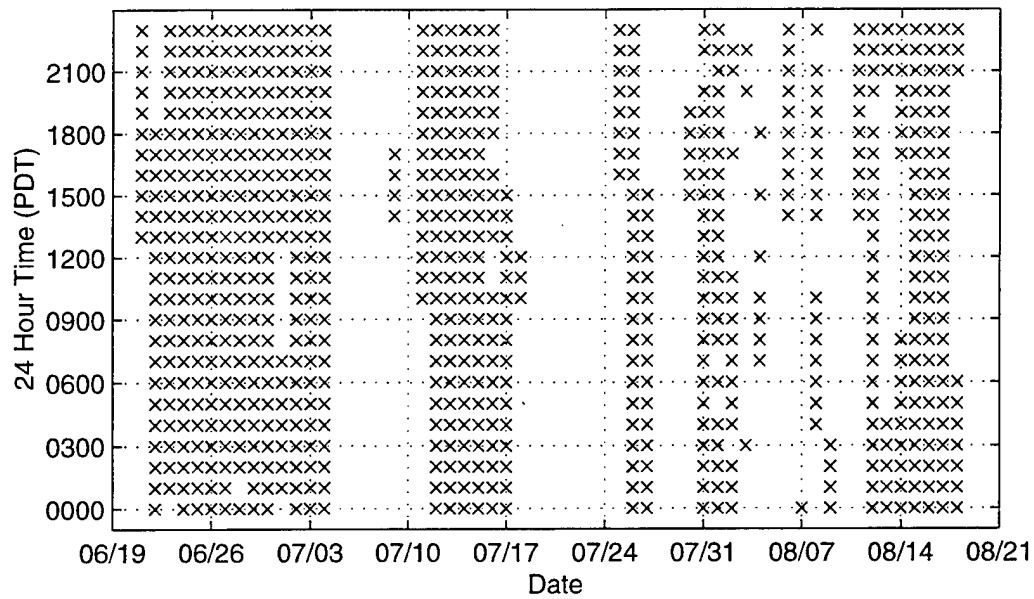
**Figure 14.** Listing by hour when usable data was concurrently available from both MCR sites during summer 1997 for channel 3 (top) and channel 4 (bottom).

40
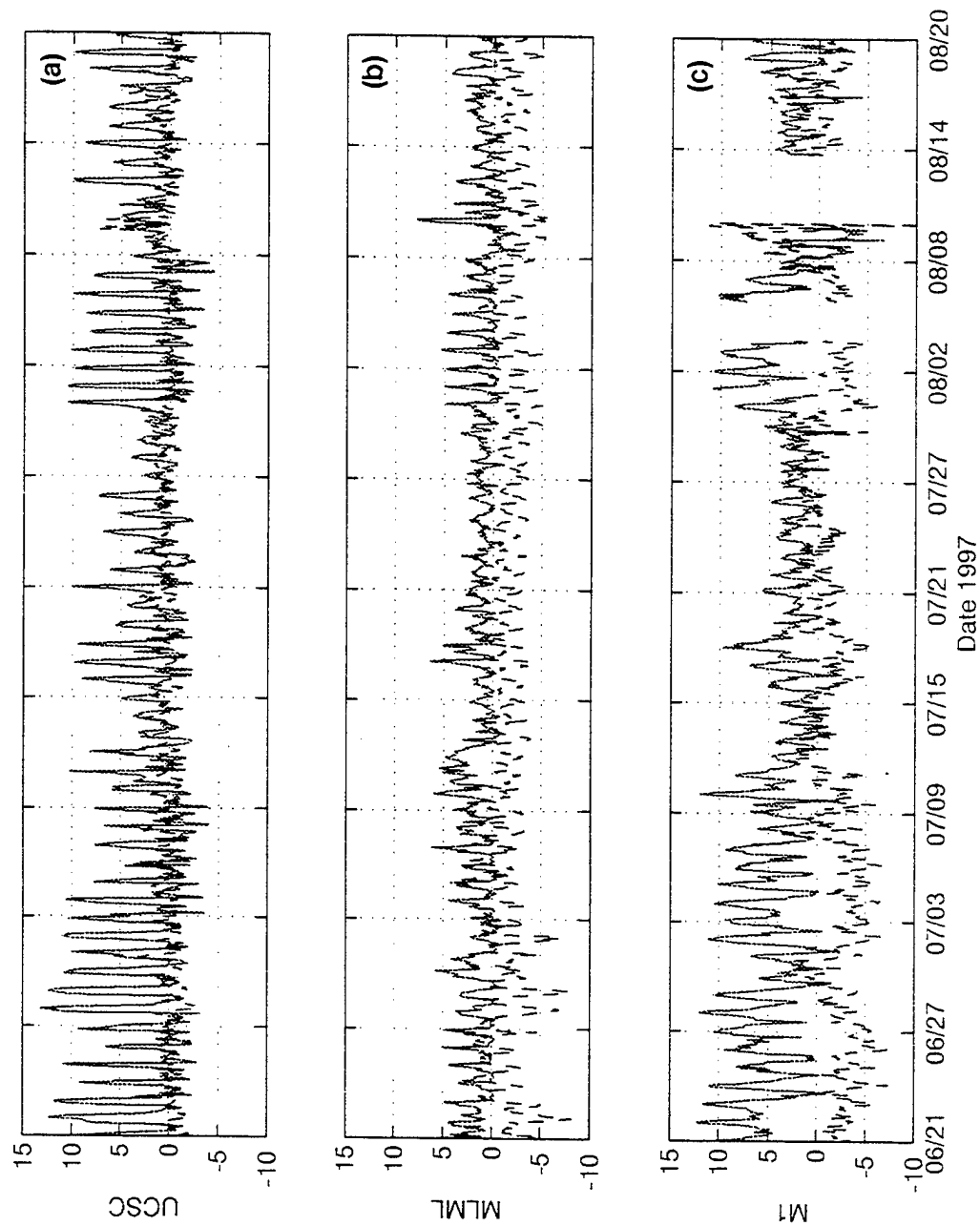
**Figure 15.** Time series of east-west [solid] and north-south [dashed] in-situ wind components in m s$^{-1}$ measured by (a) Long Marine Laboratory land station at the University of Santa Cruz (UCSC); (b) MRARI near the Moss Landing Marine Laboratory (MLML) land station; and (c) mooring station M1 operated by MBARI. Vertical tick marks indicate midnight GMT for the given day.

41

# IV. RESULTS

## A.    MCR MEASUREMENTS

As mentioned above, the in-situ observations at the M1 mooring are considered the primary ground truth for comparisons to the radar measurements at grid points near the mooring position. Within the coverage area of the Santa Cruz MCR, the M1 mooring position lies in the 8th range bin and 5° to the left of the radar broadside look direction (173° true), based on the 3-km range and 5°-azimuth resolutions set in the beam formation algorithm. Similarly, the mooring position coincides with the 7th range bin and 25° left of broadside (283° true) of the Moss Landing MCR. Hence, the mooring measurements are close to the broadside look directions and range of both radars so that side lobes are minimized, and the beam directivity is higher compared to larger steering angles. Since the land stations at Santa Cruz and Moss Landing are approximately 6 km from the first usable range bin of both MCR sites, only subjective comparisons between observations and radar measurements of the wind direction near the northern and eastern portions of Monterey Bay are made. Indirect synoptic or mesoscale numerical weather analysis were not used in this capacity due to additional sources of uncertainty that they include.

In order to compare the mooring observations to the radar measurements, the mooring data was re-calculated to wind direction and speed in order to separately compare the direction and speed to the Bragg ratios and signal-to-noise of the radar

43

measurements. As discussed in the background section above, high frequency radar wind direction measurements should ideally be independent of the wind speed. In the practical application of HF radar, however, the wind speed significantly impacts the measurement. Figures 16 and 17 display the mooring wind direction (values are in the oceanography convention, i.e. 100° means winds from 280° true) and speed in the top panel, followed by the time series of the Bragg ratio (upper side peak power level minus lower side peak power level in dB) of the closest range-azimuth cell of each of the four channels of the Santa Cruz and Moss Landing MCR, respectively. No averaging or thresholds have yet been applied to the radar data. As a frame of reference, a wind direction of 100° corresponds to a Bragg ratio of -6.8 dB for the Santa Cruz MCR and +28.5 dB for the Moss Landing MCR using the cardioid model (equation [6]) with a spreading parameter equal to 4. If the radar direction measurement were truly independent of the wind speed, the Bragg ratio would follow the wind direction. This independence is clearly not the case for any of the Santa Cruz channels (Figure 16). While the negative Santa Cruz ratios do in fact verify with M1 wind directions with a component away from the radar, the ratios oscillate coincident with the diurnal wind speed. When the wind speed is minimum during the morning and the sea breeze is not well established, the Bragg ratio is near zero, even though the wind direction does not change significantly from its east-southeastward value. This result is not surprising considering that the radar-resonant waves rapidly decay as the wave heights abate each morning and, consequently reduce the radar backscatter amplitude, especially for wind-waves moving in the cross direction relative to the radar. This decrease in the morning hours is especially detrimental to the

effectiveness of the Santa Cruz radar since the Bragg ratio would be near zero anyway as the bulk of the wave energy is directed perpendicular to the radar look direction. When the four Santa Cruz channels are compared to each other, it appears that frequency has little effect on the magnitude or amplitude of oscillation of the Bragg ratio. The exception to this result is the different signature of channel 4 in which the ratio has lower magnitude and less diurnal fluctuations.

As expected, the Moss Landing Bragg ratios (Figure 17) were generally positive since the winds usually flow toward the radar. Like the Santa Cruz MCR, channels 1 and 2 at Moss Landing display a clear high-amplitude diurnal signal coincident with the wind speed observed at the mooring . However, channels 3 and 4 do not contain a high correlation with the wind speed. In fact, the channel 3 (13.3 MHz) Bragg ratio sustains at values fluctuating around 10-15 dB and displays roughly the same trends as the mooring direction. It is this signature that most fits the expectation that the Bragg ratio is independent of the wind speed. Channel 4 Bragg ratios fluctuate around zero, which indicates a degraded signal during the study period. This output will be examined more closely later.

There are two particularly noteworthy time intervals that are worth examining more closely. Specifically, the prolonged southeastward-directed flow during the first two weeks and the wind shift to northward flow in August will be examined to better characterize the performance of the radar during the typical wind conditions of Monterey Bay and during a sustained departure from those conditions, respectively. For convenience of analysis of these two events, the full period was divided into four 15-day

segments. Figures 18 through 30 display the segmented time series of the mooring observations, the Bragg ratios, and both lower and upper side SNR of each site and channel. The multiple lines in the radar time series are each radar's closest three points to the mooring in order to illustrate the (minimal) variability from one range-azimuth cell to another.

## 1.    21 June - 5 July

Prolonged southeastward (towards ~100° true) flow dominates at M1 during this time, with the exception of 29-30 June when the wind abruptly shifted towards the north, but fell off in speed to less than 2.5 m s$^{-1}$. The wind speed generally maintained above 2.5 m s$^{-1}$ otherwise. Although there is about a 7 m s$^{-1}$ daily fluctuation in wind speed, the sustained flow during the evening hours has longer duration than any other segment and, thus, presents the best possibility for fully developed seas. First considering channel 1 (Figure 18), there is a clear diurnal cycle in the Bragg ratio (discussed above) and in both upper and lower SNR at both sites. The SNR traces are in phase for each site, and as would be expected, and the SNR increases during the daytime and evening hours then decreases to the lowest values during the early morning hours. The fact that the channel 1 amplitude of the dominate side SNR (lower side for Santa Cruz and upper side for Moss Landing) has greater daily variance than the subordinate side indicates that the Bragg peaks do not grow and abate equally with the wind speed. This disparity would cause an obvious error to the radar-derived wind directions. Channel 2 (Figure 19) exhibits similar results.

Channel 3 (Figure 20), however, has markedly different output. The Bragg ratio at Santa Cruz still displays a daily oscillation, but the upper side SNR amplitude is greatly dampened to the point where there is no discernable diurnal signal. Moreover, both the Bragg ratio and the lower side noise are relatively free of the diurnal signal at Moss Landing. The caveat to this encouraging output is the fact that the Moss Landing lower side SNR is equally as low during low wind speeds which indicates that the lower peak is very close to the noise level. In other words, the positive peak is very evident above the noise, but the negative peak is indistinguishable above the noise. Hence, the Bragg ratio and radar-derived direction would be less accurate due to this contamination of the negative peak. Santa Cruz channel 4 (Figure 21) displays similar output to channel 3, except the diurnal fluctuations in the lower-side SNR are even less.

What is not clear from the SNR plots is whether the diurnal SNR fluctuations are due solely to variations in the Bragg peaks or a combined oscillation of the noise levels, as well. Figures 22 to 25 display again the mooring data and the Bragg ratio in the top panels, but, instead, the actual Bragg peak power and noise levels for the upper and lower sides of the spectrum are displayed. Santa Cruz channel 1 (Figure 22) noise levels clearly dropped of when the wind speed was minimum, but Bragg peak levels did not fall by the same amount. In fact, there are some times (e.g. 28 June) when the lower peak was at a maximum value, but the noise level was a minimum. In sharp contrast, the Moss Landing channel 1 and 2 (Figure 23) peak power and noise levels oscillated nearly in phase and by nearly the same magnitude. Thus, it appears that the noise level fluctuations are the principle contributor to the SNR oscillation at each site.

The channel 3 (Figure 24) noise levels are notably different from channels 1 and 2. The Santa Cruz levels are nearly constant with respect to time of day, and the magnitude of fluctuations at Moss Landing is half as much as the other channels. The reason for the near-constant Bragg ratios at Moss Landing is evident from the lower and upper peak levels {Figure 24(g) and 24(h)}. The peaks do, in fact, oscillate with the mooring wind speed, but the magnitude of each oscillation is nearly equal in each peak. Hence, the Bragg ratios do not follow the wind speed. The low SNR of the subordinate peaks notwithstanding, channel 3 should produce the most credible wind directions based on this result.

The Moss Landing channel 4 (Figure 25, right column) Bragg peak levels are nearly identical for both sides of the spectrum, and, consequently, the Bragg ratios are always near zero. Since the signal measured by the Santa Cruz channel 4 did not display this same result, there is some additional degradation of the signal at Moss Landing. Vesecky (1998) suggests that the low transmitter power and higher propagation loss of channel 4 may account for the poor output of that channel.

### 2. 5 - 20 August

During the early part of August there was a wind shift from southeastward to northward (Figure 15). Although the mooring wind direction does rapidly fluctuate from the 8th to the 10th, the wind speed was significantly stronger ( $> \sim 5$ m s$^{-1}$) than other times when the wind had a northerly component. Unfortunately, there was little or no Santa Cruz radar data during this time, particularly from channel 1 (Figure 26). The

intermittent data from channel 2 (Figure 27) on 9 August does verify with the mooring observations. The Bragg ratio at Santa Cruz changes to positive (winds towards the radar) and the Bragg ratio at Moss Landing does tend towards zero (wind across the radar). Also interesting to note is that the Santa Cruz upper side SNR is higher than usual as the noise level has fallen about 5-8 dB. The Moss Landing upper side SNR lowers during the same period as the upper peak is less pronounced above the noise. Santa Cruz channel 3 (Figure 28) does not identify the shift as well as channel 2 on the $8^{th}$-$10^{th}$, but does identify the wind shift on $16^{th}$ and $17^{th}$. The reason for this disparity can been seen in the poor SNR on the $8^{th}$-$10^{th}$ which was caused by an anomalous jump in the channel 3 output (Figure 30). Both the peak powers and the noise floor spike on 9 August at 0100 which was probably caused by temporary internal system interference. The SNR drastically improved by the $16^{th}$ and $17^{th}$. The output is slightly better at Moss Landing, but the upper side SNR is markedly less than channel 2. The output for Santa Cruz channel 4 (Figure 29) does pick up the shift on the $16^{th}$, but the Moss Landing output is again degraded.

In summary, channel ·3 appears to have most viable output during both the sustained southeastward and brief northward flows. The next section will objectively compare radar-derived wind directions to the mooring measurements and identify when the radar is most likely to produce accurate wind directions based on the present wind retrieval algorithm.

## B. MOORING OBSERVATIONS VS. RADAR MEASUREMENTS

### 1. Model Selection

To compare the radar-derived wind direction to the mooring observations, a suitable model to invert the Bragg ratio was first chosen for the wind retrieval algorithm. Of the three models presented in section II, the linear model (Georges, et al. 1993), equation [15], was used here since it is similar to the cardioid model for Bragg ratios in the ranges observed by the MCR, but it also accounts for observed winds directly towards or away from the radar, whereas the cardioid model requires very large ratios (beyond the dynamic range of the summer 1997 MCR data) to achieve near-zero relative wind angles (Figure 4). Additionally, using a fixed spreading parameter equal to 4 in the cardioid model is not necessarily appropriate for the higher frequencies of the MCR (Table 1), and basing the spreading parameter on mooring wind speeds removes the independence of the radar estimates. The Long and Trizna (1973) model, equation [14], was not used because the linear data better correlated to the mooring data and there was no clear justification to use the non-linear relationship.

The issue then arose whether or not the reference value of 24 dB was suitable for the ground-wave MCR data. When the mooring winds were directly towards each site, it was found that the Bragg ratios were consistent with the 24-dB reference value. Figure 31 shows the behavior of the Bragg peaks and noise along the broadside radial of each site with respect to range of each MCR during the limited time periods when the wind was blowing toward the radar sites (0° look direction) according to the observed winds at

the M1 buoy. The first range bin is not shown due to signal overload at close range, and the jump in Bragg levels at range bin 11 signifies the different encoding used within the beam formation processing for the longer range bins. Although the noise level is nearly constant, the decrease in both upper and lower power levels shows how the SNR drops off with range. Nonetheless, these two cases are good examples that show a near-constant Bragg ratio of approximately 20 dB for the first ten range bins. This result implies that the radar-derived wind direction would not vary with range, given that the actual wind direction was uniform along the radial, and that an upwind calibration of the Bragg ratio probably does exist. The high variability (~ 7-8 dB) of the Bragg power among upwind cases precluded establishing a more statistically significant reference than the 24-dB value used by Georges et al. (1993). Further study of MCR output at additional sites and wind conditions will be required to establish a more precise upwind reference value with statistical significance.

## 2. Signal-to-Noise Considerations

In order to produce prudent radar-derived wind directions, both Bragg peaks must be distinguishable above the noise floor of the power spectrum. Often, one or both of the MCR Bragg peaks is very close to the noise level. Since the noise computation is simply a statistical measure of the higher-order return in the spectrum, there is an expected variance of the noise floor among different spectra. The noise level (the horizontal line segment on each side of the spectrum in Figure 8) computed for each range-azimuth cell widely varies, depending on numerous environmental and system factors, such as wind

speed, frequency, look direction, output power, etc. Ideally, the variance of the noise level for each spectrum should be determined as part of the spectrum generation to ensure Bragg peaks are statistically significant over the noise. Instead, fixed SNR thresholds were applied here to all spectra in order to illustrate how many measurements meet various threshold criteria, and are consequently likely to give suitable data to the wind retrieval algorithm.

Arbitrary SNR thresholds of 3 dB and 5 dB were applied, based on inspection of the SNR time series (Figures 18 to 30). Figure 32 displays a scatter plot of the mooring wind direction vs. the radar-derived direction derived by the wind retrieval algorithm at the closest grid point to the mooring. Data that meets the 3-dB SNR criteria from each MCR channel are displayed. The directions are in the oceanography convention, and each point represents the concurrent hourly wind direction measurement by the mooring and the two radars (although the radars transmit during separate 12-minute blocks within the first half of each hour). The diagonal line represents equal measurements by both platforms, while the dotted lines on either side of the diagonal line show errors of ± 15°. There is obviously great spread of the data. Channels 1 and 2 radar directions are generally limited to a range of 0° to 200°, and channel 3 and 4 results show no correlation to mooring winds outside the same range. The channel 4 directions should be viewed cautiously since the 3 dB threshold is within the poor SNR output at the Moss Landing MCR (Figure 21). There are apparent horizontal bands in the measured radar directions, which imply that radar-derived solutions have preferential directions. These bands can be

attributed to the left-right solution bias inherent to measurement from each site. The averaging in the wind retrieval algorithm reduces, but does not eliminate, this bias.

When the SNR threshold is increased to 5 dB (Figure 33), the correlation is still poor, but the spread of the data decreases significantly and many of the "outliers" disappear. However, the number of points substantially decreases from about 700 to 250 for each channel (except channel 4, which falls to less than 50 due to the low SNR). As will been seen in the wind maps of the next section, this 2 dB increase in the SNR threshold has a severe degradation on the usable full-field data. Nonetheless, correlation coefficient calculations with this threshold verify that channel 3 best agreed (although the correlation coefficient was only 0.395) with the mooring winds so that measurements at this channel can be further analyzed to identify specific times when the radar and wind retrieval algorithm are likely to produce viable wind direction maps.

### 3. High vs. Low Wind Speed

The signal quality discussion in section IV.A. indicates that the MCR clearly has better SNR during higher wind conditions when wave heights and backscatter intensities are high. To illustrate this effect, channel 3 radar data during mooring wind speeds of 5 m s$^{-1}$ or greater were separated from low wind conditions, based on the typical daytime maximum and nighttime minimum wind speeds during the period. Figure 34(a) shows the results applied to the 5-dB SNR data. There is clear correlation improvement during high wind conditions. Moreover, when the speed criteria is increased to 7.5 m s$^{-1}$ {Figure 34(b)}, the correlation improves, but the number of measurements falls off by nearly half.

Interestingly, Heron (1985) performed this same high-low wind speed analysis on a 30-MHz radar data set and found no clear improvement in the correlation with in-situ observations.

## 4. Short vs. Long Wind Duration

To assess the effect of wind duration on the radar performance, the channel 3 data was subdivided into periods when the wind speed sustained above 5 m s$^{-1}$ for longer than the 12 hours expected growth time for fully developed seas calculated from equation [16]. Figure 35 displays the results. Similar to the high wind analysis, the MCR-derived wind directions better agree with the mooring observations when the wind has sustained for long duration when the ocean is most likely at its fully developed state. Although there are many short-duration points that also agree with the mooring values, the long duration points are exclusively close to the in-situ measurements, with the exception of three outliers.

## 5. Identification of Optimum Radar Measurements

Hourly radar measurements that agreed to within 15° of the mooring observations were identified (open circles in Figure 36) as potential times for accurate full-field radar measurements. Only times when both radar sites were available (Figures 13 and 14) to resolve the left-right solution ambiguity were considered. Additionally, times when the mooring wind speed was above 5 m s$^{-1}$ and the duration was greater than 12 hours were identified and are shown as dots and crosses, respectively. As expected, the radar had

close agreement to the mooring generally during the afternoon and evening hours coincident with times of high wind speed conditions. However, there was also good agreement during many early morning hours on 23 June to 3 July because the wind speed sustained above 5 m s$^{-1}$ (Figure 16), and thus, the seas were sufficient to produce suitable backscatter for the radar. During July good agreement occurs generally in the afternoon, and there are no agreement times during the northward winds in early and mid-August. It is important to note, however, that radar measurements at points near the mooring have only been considered thus far. The next section will display the full radar field in light of the SNR considerations presented above and show when environmental conditions are both favorable and unfavorable to the accuracy of the radar measurements.

## C.   WIND MAPPING

The full field of the radar measurements from each site can be displayed, as well as the field calculated by the wind retrieval algorithm described in section III.B. Figure 37 displays the left and right channel 3 (with a SNR threshold of 5 dB) solutions of each site for 24 June 1997 at 1600 PDT, which is a time when the wind speed was greater than 5 m s$^{-1}$ and the radar-derived direction at points around the mooring agreed to within 15°. Each radar arrow is unit length since Bragg peaks reflect direction information only. The wind arrows from each site are radially spaced to each range-azimuth cell set by the beam formation algorithm. The effect the 5 dB threshold is evident on both site maps. For this particular case, most of the long range range-azimuth cells beyond the 9th range bin of

55

the Santa Cruz MCR and nearly all cells beyond the 5th range for the Moss Landing MCR fail to meet the signal criteria.

Since the wind retrieval algorithm does not compute a direction if there is not at least two usable (both Bragg peaks are 5 dB above the noise) measurements around a grid point, the subsequent resolved wind map has very limited spatial coverage (Figure 38). The solid dots at each grid point display the average SNR of the smaller peak from the site solution that was used at each grid point, as determined by the retrieval algorithm. For comparison, the mooring, Santa Cruz (UCSC) and Moss Landing (MLML) in-situ wind vectors are also plotted. The results of this example are typical of the entire period.

In light of the severe degradation in coverage with a threshold of 5 dB, wind maps with this criteria would show only small, sporadic patches of radar-derived measurements, primarily closer to the radar sites due to higher propagation loss at longer range. Although the measurements that do meet this SNR criteria could be viewed with higher confidence, the resultant maps were of little use to describe the mesoscale coastal features in Monterey Bay. Hence, the SNR threshold was lowered to 3 dB to include more data in the wind maps with the realization that the confidence in the radar-derived directions is somewhat lower.

Figure 39 illustrates the improved coverage gained by the lower SNR criteria for the same case used above. Nearly all of the Santa Cruz data is accepted, as well as much more of the long range data from Moss Landing. Figure 40 shows the resultant wind map, which is near the time of maximum sea breeze in Monterey Bay. The directions are generally continuous, and the radar-derived directions match well with the mooring

estimate and the eastward flow in the northern portion of area near Santa Cruz. The radar measurements clearly identify the apparent turning of the wind flow to align with the entrance of the inland valley at Moss Landing.

When the wind speeds are low or fetch and duration are limited, the backscatter intensity from radar-resonant waves will be low due to low wave heights. Figure 41 is an example of the MCR output from both sites during low wind conditions. The wind speed at all three in-situ stations is less than 2 m s$^{-1}$. Since the SNR is low for both Bragg peaks in this case the Bragg ratio tends toward zero, and consequently, the solutions are $\pm$ 90° from each look direction. These polarized solutions generated from both sites are not realistic, and can be viewed as diagnostic for poor signal conditions. The resolved wind map (Figure 42) under these conditions is chaotic. This result is typical during early morning hours, particularly if the winds are calm.

## 1. Sea Breeze Cycle Detected by Radar Measurements

The channel 3 radar-derived wind directions generally agreed with the mooring observations during the complete 24-hour period on 27 June (Figure 36). Figures 43 to 66 display the hourly resolved radar measurements for this day. The winds over water were towards the southeast and relatively strong (~ 8-10 m s$^{-1}$), but the observations at UCSC and MLML were calm during morning hours from 0000 to 0900 PDT (Figures 43 to 52). The radar directions seaward of M1 agree with the mooring direction quite well, but closer to MLML the radar directions are directed east-northeastward and are consistent with the typical (canonical) land-breeze directions analyzed by Foster (1993) at

a station south of Moss Landing. By 0400 (Figure 47) the directions near shore are rather chaotic. From 0400 to 0700 (Figure 50), the wind abates and some radar data drops out below the 3 dB criteria. By 0800 (Figure 51), the winds measured by M1 start to increase in speed, and the MLML winds shift to align with the inland valley. Between 1000 and 1100 PDT (Figures 53 and 54, respectively), there was a wind reversal and speed increase at UCSC and an speed increase at MLML. These observations signal the onset of the sea breeze along the coastline. The radar measurements show an eastward change in direction near MLML by 1200 PDT (Figure 55), which is an hour or so later. This time lag would be expected as the radar-resonant waves build in response to the wind forcing. By 1400 (Figure 57), the radar directions near MLML shift slightly more southeastward, but the radar measurements never align with the southward observations at MLML. During the afternoon hours the radar arrows show that winds diverge or split south of the mooring where some of flow moves towards the city of Monterey. This difluence is again consistent with observations in Foster (1993). On this particular day the sea breeze pattern sustained well into the evening and was well depicted by the radar. Other sea breeze cycles (not shown) display similar results, but often show a time lag of an hour or two since the radar-resonant seas require time to build toward the fully developed state.

## 2. Northward Flow in August

As mentioned in section III.C.2., channel 3 Bragg ratios at the Santa Cruz MCR fit the mooring and UCSC in-situ observations of northward winds on the 16 and 17 August. Figures 67 to 72 display selected hourly radar and in-situ measurements from 0600 to

1800 PDT on 16 August. Clearly, the radar-derived winds reverse from the usual southeastward direction and concur with the mooring measurements throughout the morning. There is significant SNR throughout the domain during this fetch-limited condition. However, after the northward flow breaks down between around 1400 (Figure 70), the northwestward directions in the radar data persist to 1800 (Figure 72). This disagreement is likely due to the decay time of the radar-resonant waves and weak re-establishment of onshore flow as noted in the mooring measurements and low SNR in the radar data.
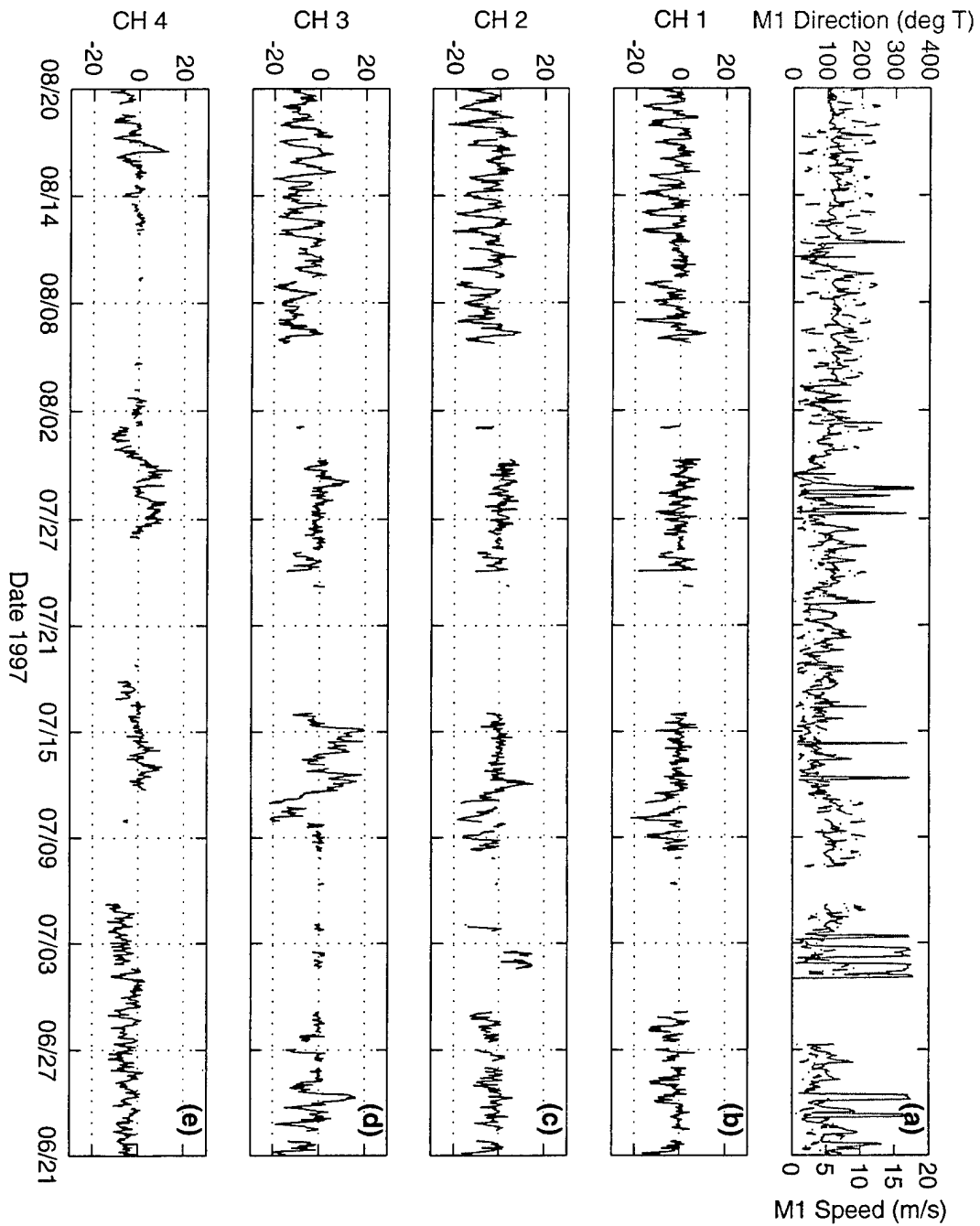
**Figure 16.** (a) Mooring M1 wind direction [solid] (oceanography convention, in degrees measure from true north) and speed [dashed] in m s$^{-1}$. Bragg ratios (upper peak power minus lower peak power in dB) measured at the Santa Cruz MCR are shown for channel 1 (b), channel 2 (c), channel 3 (d) , and channel 4 (e). Ticks on the time axis mark midnight GMT for the given day.

60
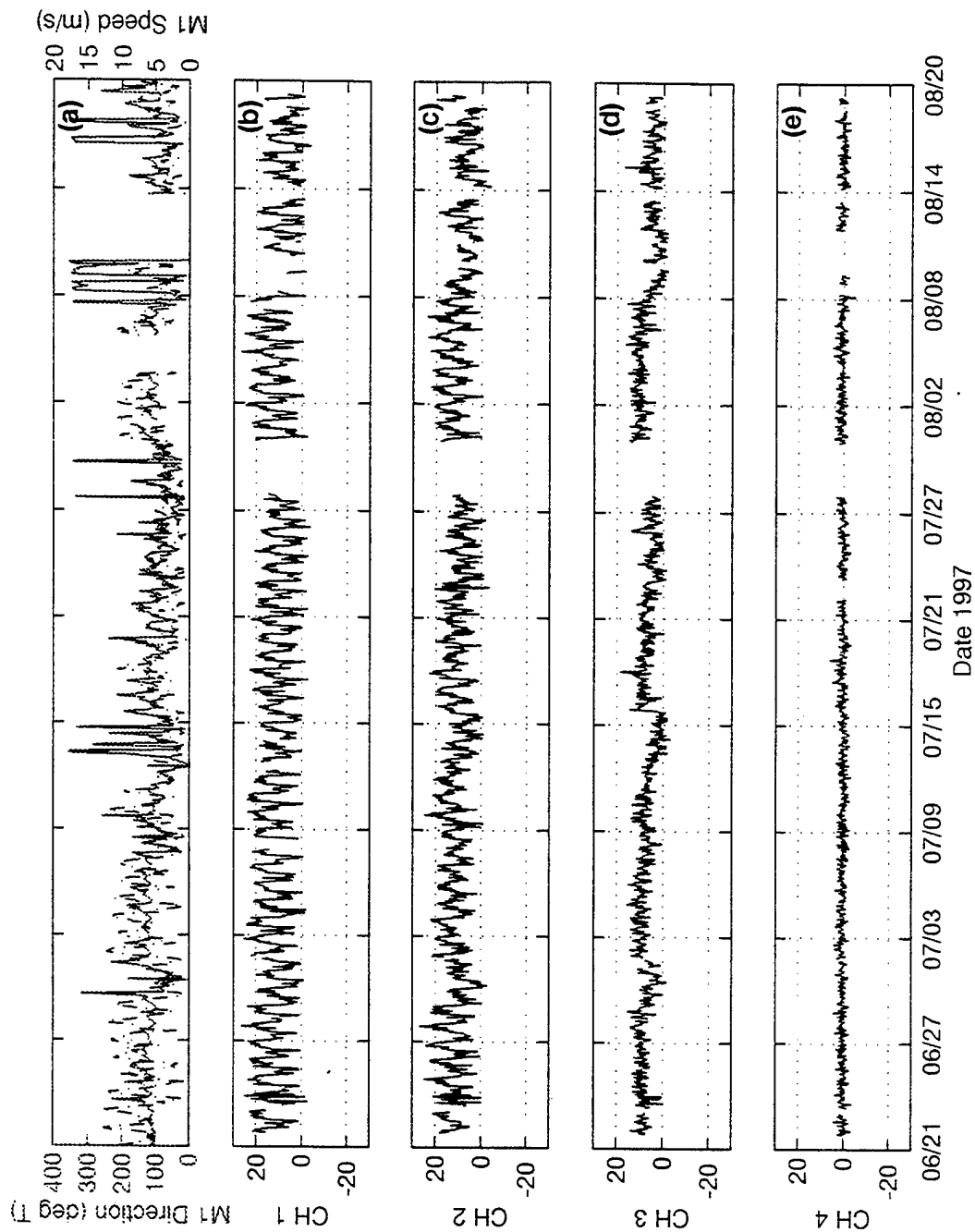
**Figure 17.** (a) Mooring M1 wind direction [solid] (oceanography convention, in degrees measure from true north) and speed [dashed] in m s$^{-1}$. Bragg ratios (upper peak power minus lower peak power in dB) measured at the Moss Landing MCR are shown for channel 1 (b), channel 2 (c), channel 3 (d), and channel 4 (e).
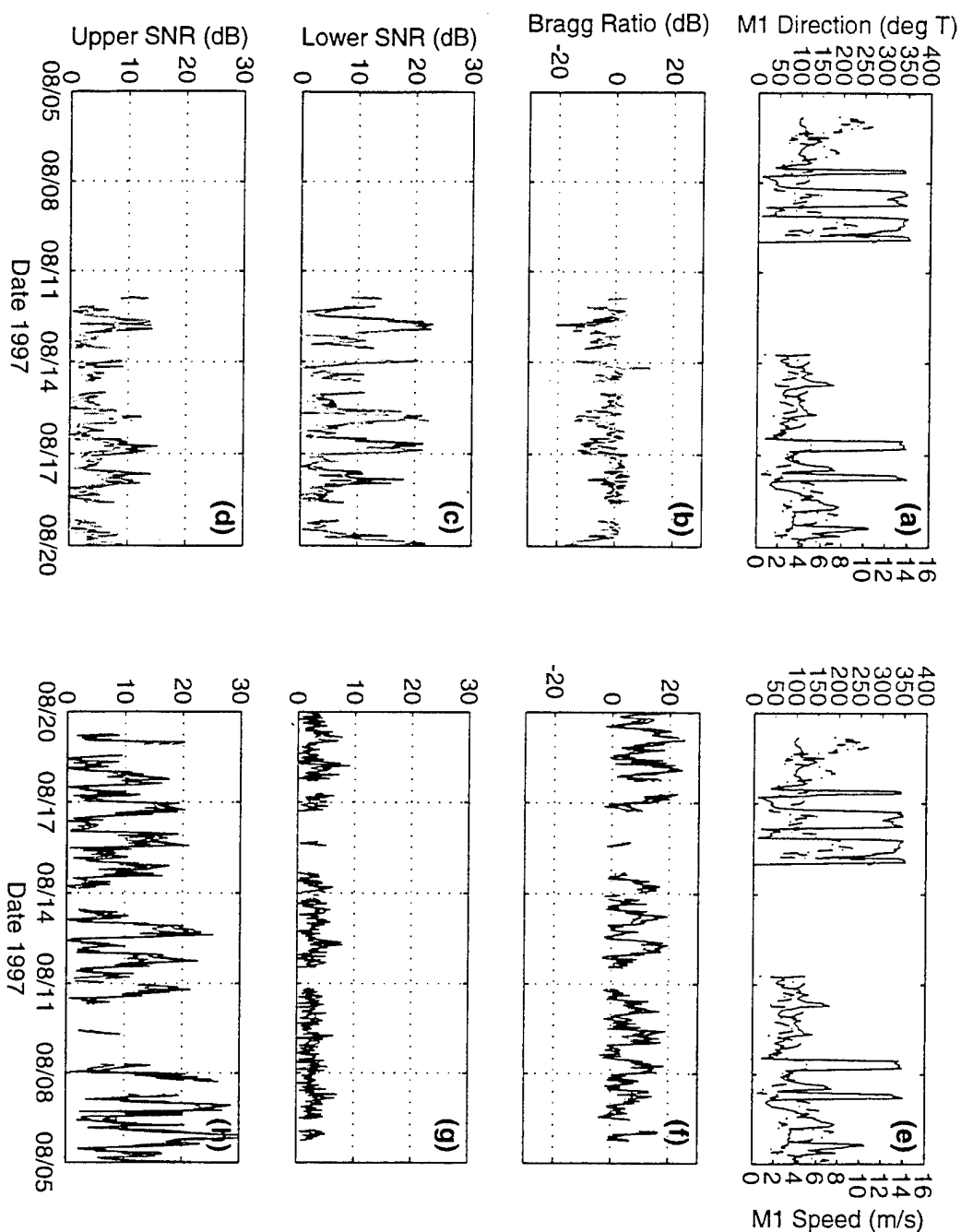
61
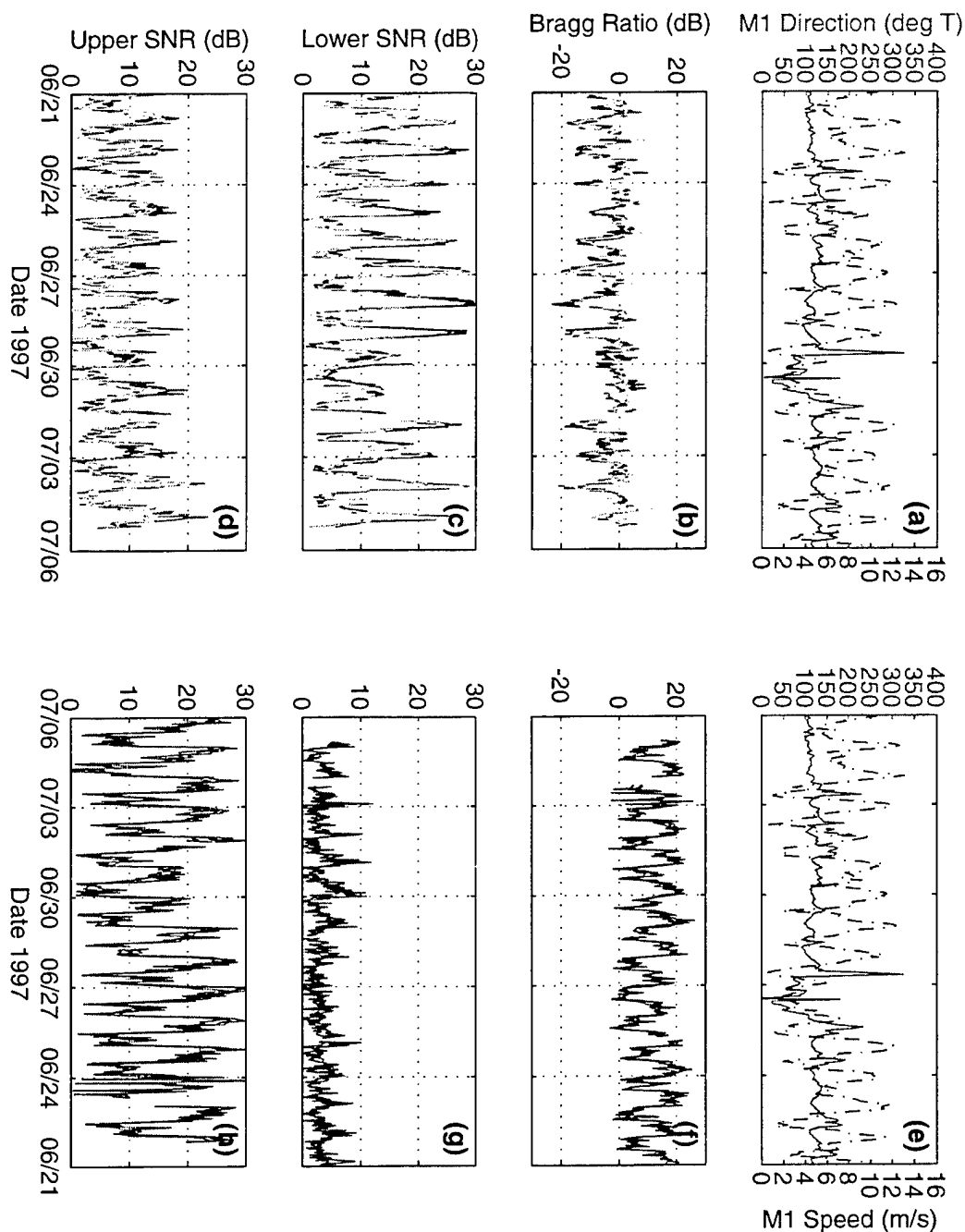
**Figure 18**. Mooring M1 and MCR channel 1 measurements from 21 June to 6 July 1997. (a) and (e) mooring M1 wind direction and speed followed by the Santa Cruz (b) Bragg ratio; (c) lower side signal-to-noise; (d) upper side signal-to-noise. The right column shows the Moss Landing (f) Bragg ratio; (g) lower side signal-to-noise; (h) upper side signal-to-noise. Ticks on the time axis mark midnight GMT for the given day.
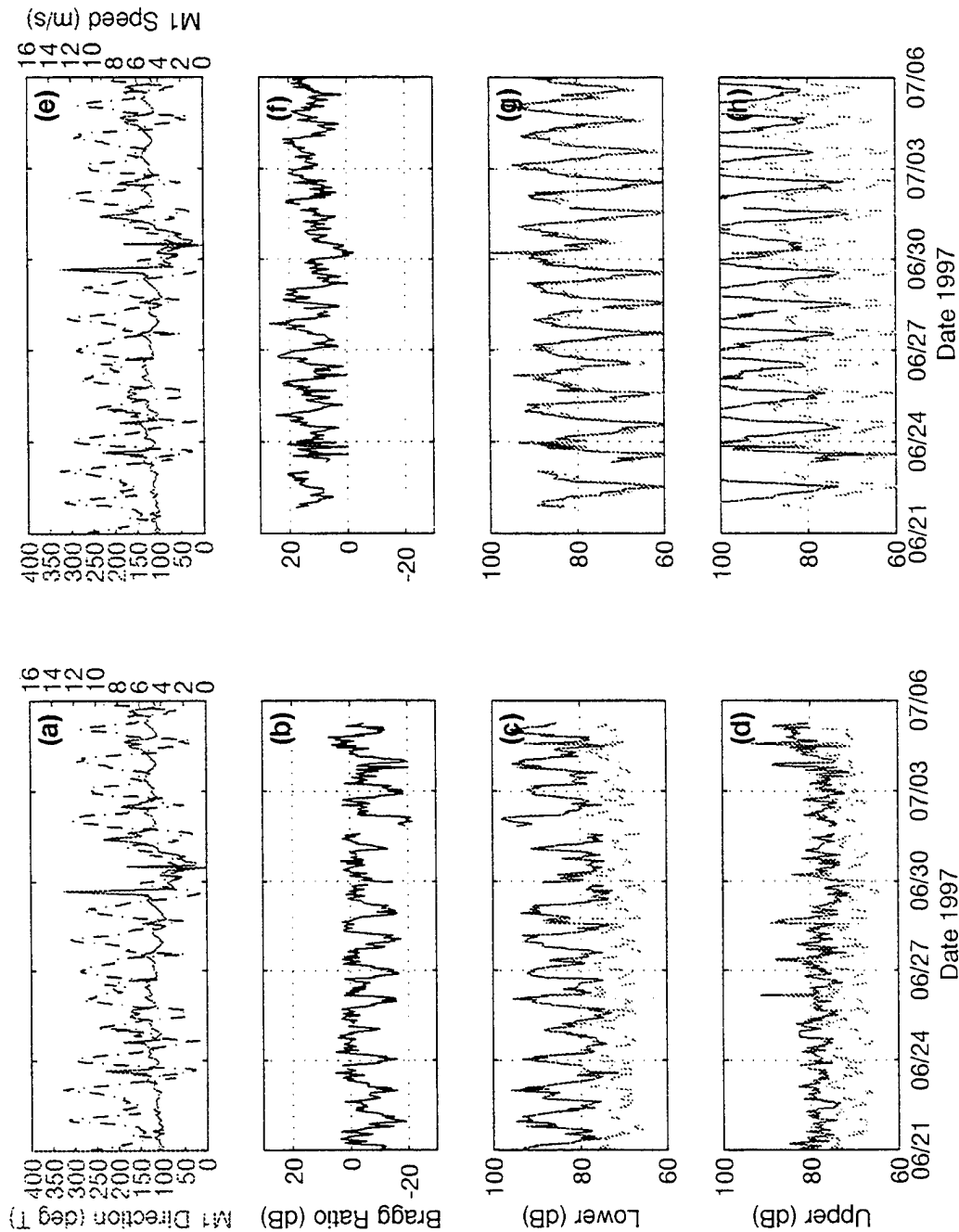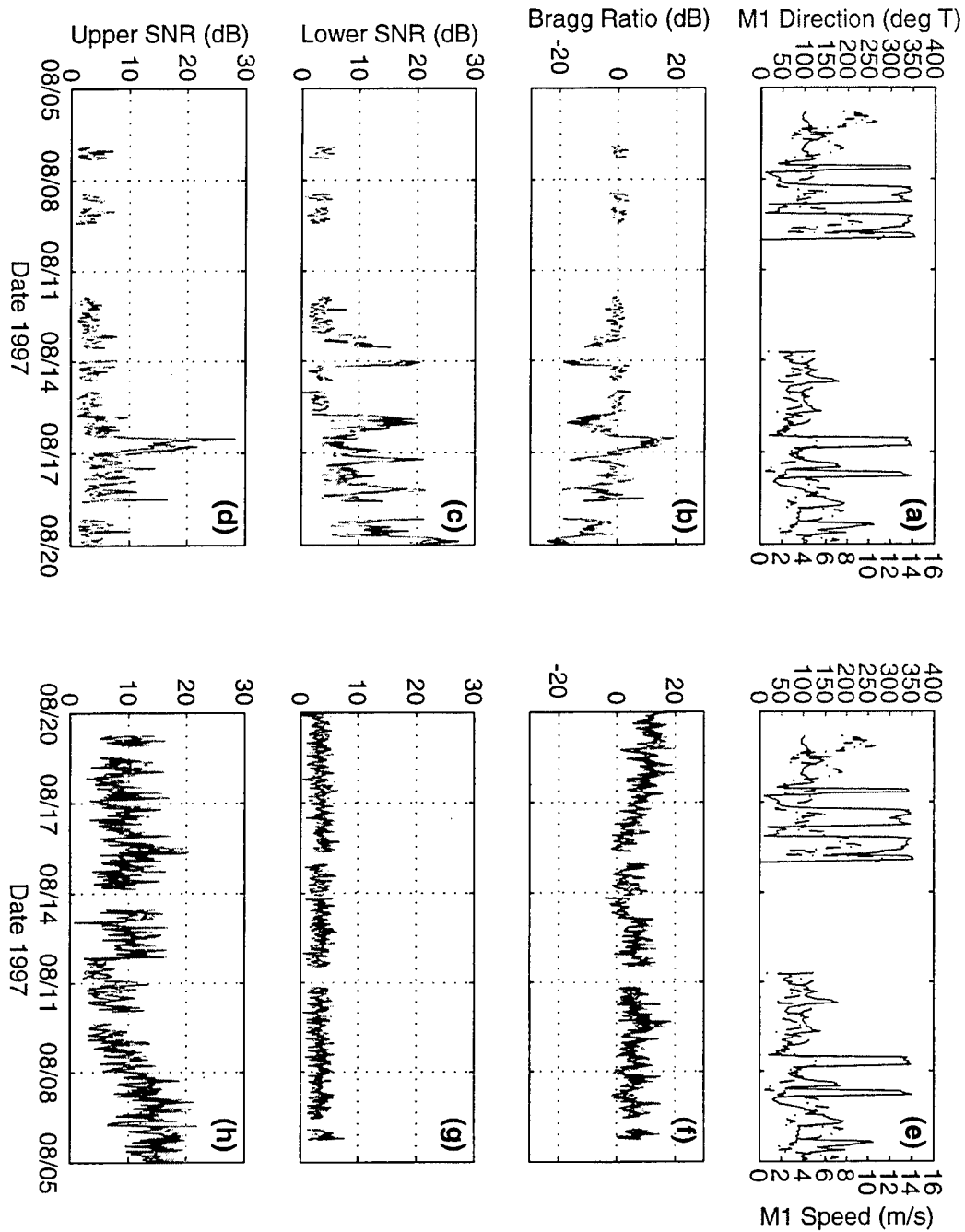
62
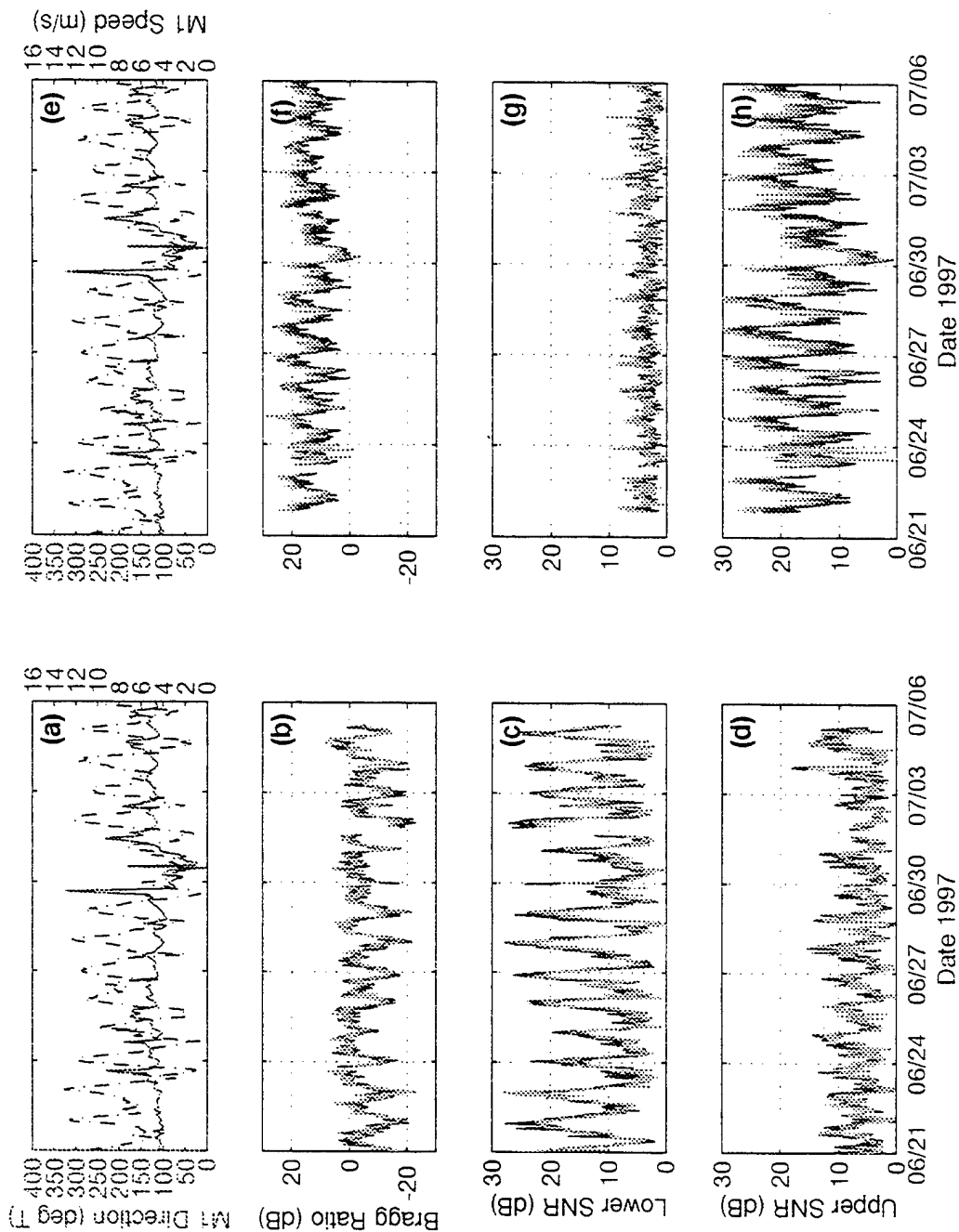
**Figure 19**. Mooring M1 and MCR channel 2 measurements from 21 June to 6 July 1997. (a) and (e) mooring M1 wind direction and speed followed by the Santa Cruz (b) Bragg ratio; (c) lower side signal-to-noise; (d) upper side signal-to-noise. The right column shows the Moss Landing (f) Bragg ratio; (g) lower side signal-to-noise; (h) upper side signal-to-noise.

63
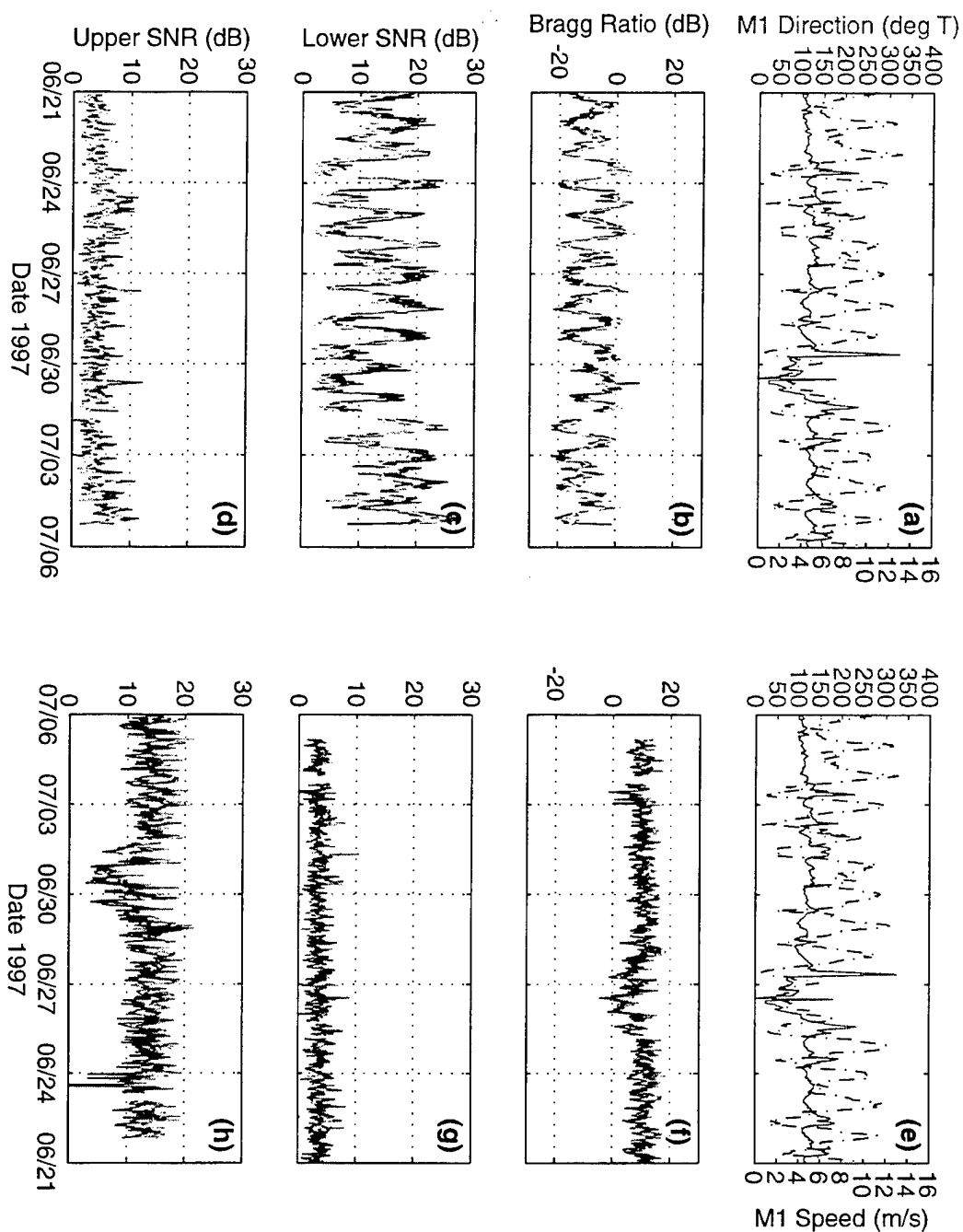
**Figure 20.** Mooring M1 and MCR channel 3 measurements from 21 June to 6 July 1997. (a) and (e) mooring M1 wind direction and speed followed by the Santa Cruz (b) Bragg ratio; (c) lower side signal-to-noise; (d) upper side signal-to-noise. The right column shows the Moss Landing (f) Bragg ratio; (g) lower side signal-to-noise; (h) upper side signal-to-noise.
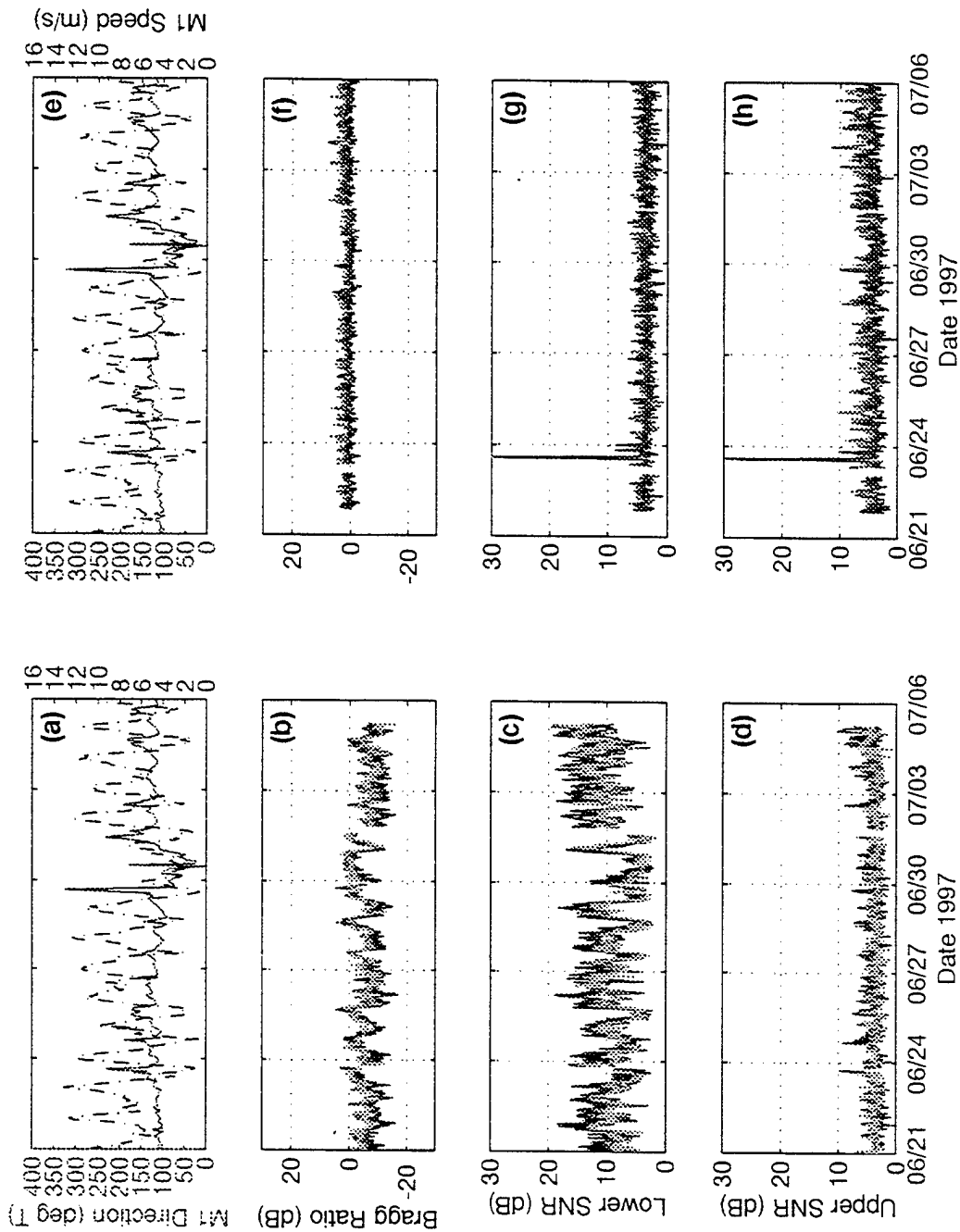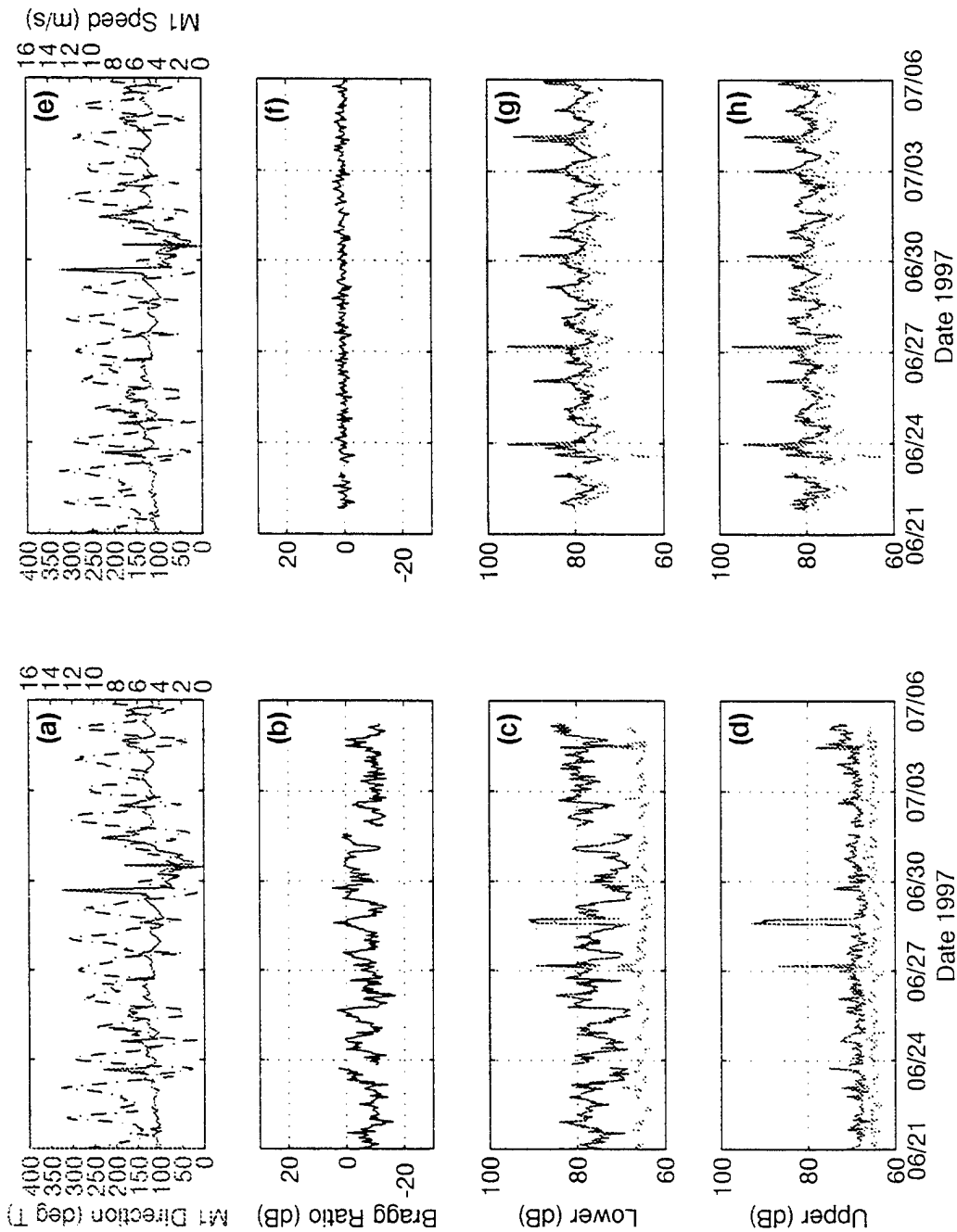
**Figure 21.** Mooring M1 and MCR channel 4 measurements from 21 June to 6 July 1997. (a) and (e) mooring M1 wind direction and speed followed by the Santa Cruz (b) Bragg ratio; (c) lower side signal-to-noise; (d) upper side signal-to-noise. The right column shows the Moss Landing (f) Bragg ratio; (g) lower side signal-to-noise; (h) upper side signal-to-noise.
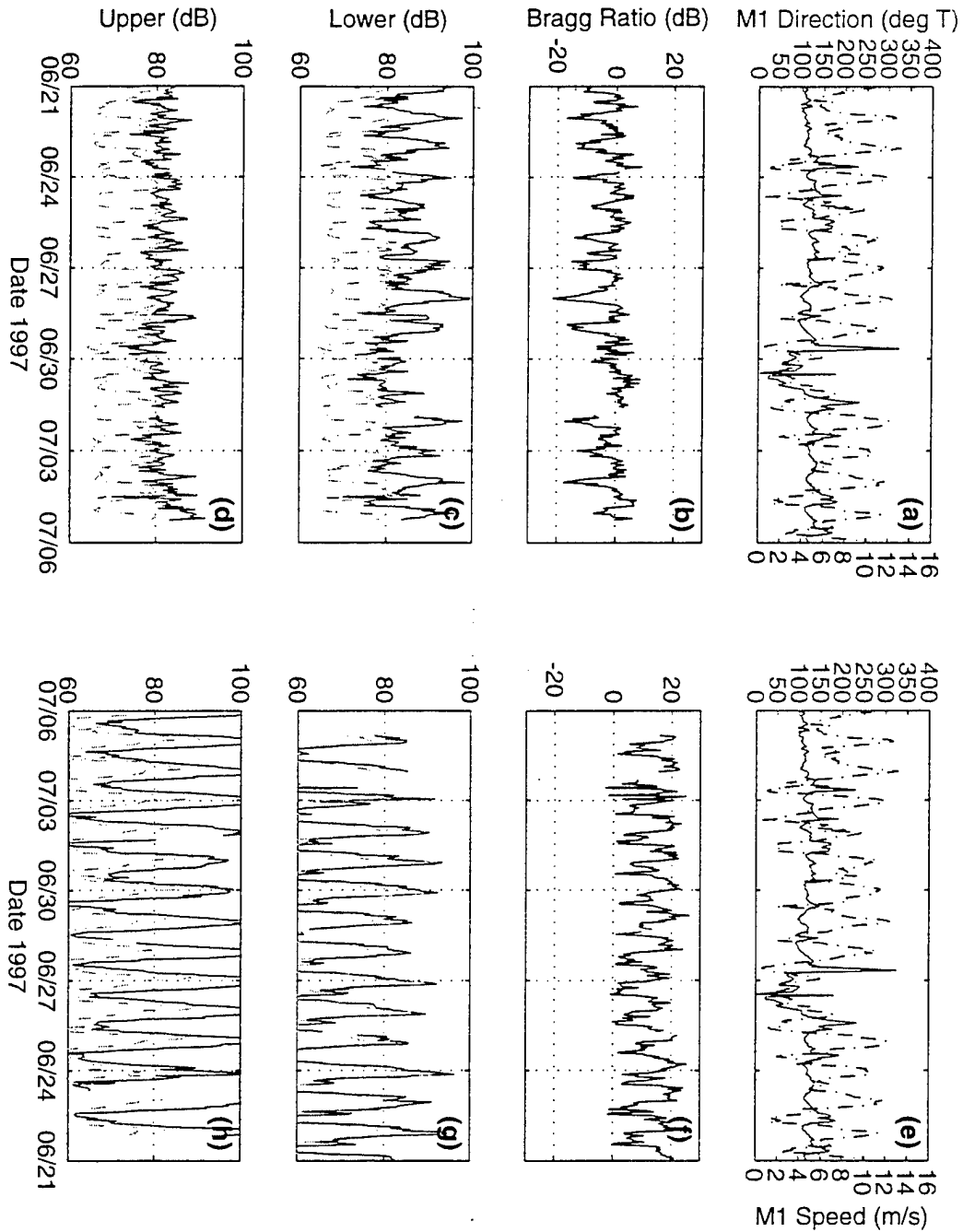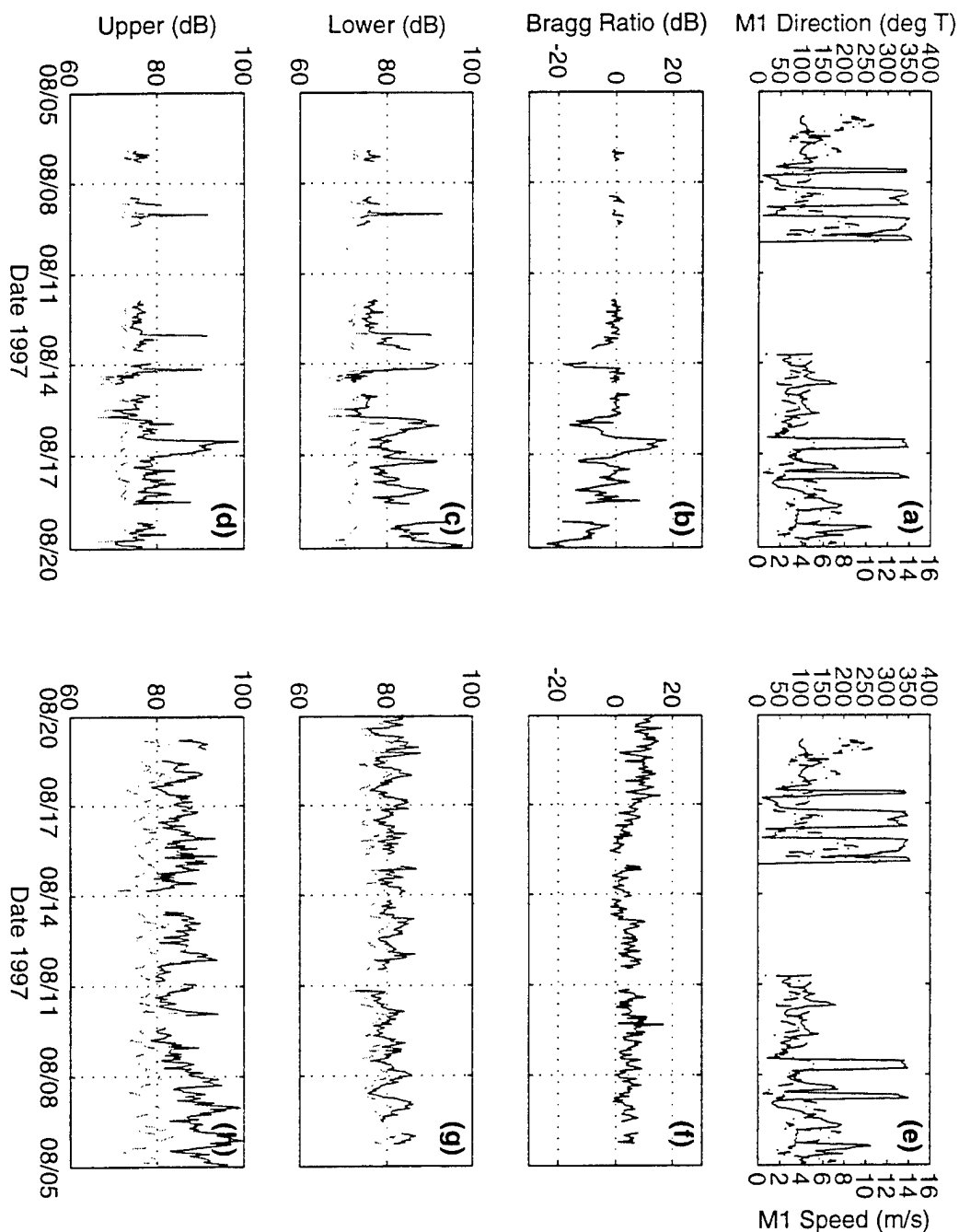
**Figure 22.** Mooring M1 and MCR channel 1 measurements from 21 June to 6 July 1997. (a) and (e) mooring M1 wind direction and speed followed by the Santa Cruz (b) Bragg ratio; (c) lower side peak power [solid] and noise [dashed]; (d) upper side peak power [solid] and noise [dashed]. The right column shows the Moss Landing (f) Bragg ratio; (g) lower side peak power [solid] and noise [dashed]; (h) upper side peak power [solid] and noise [dashed].
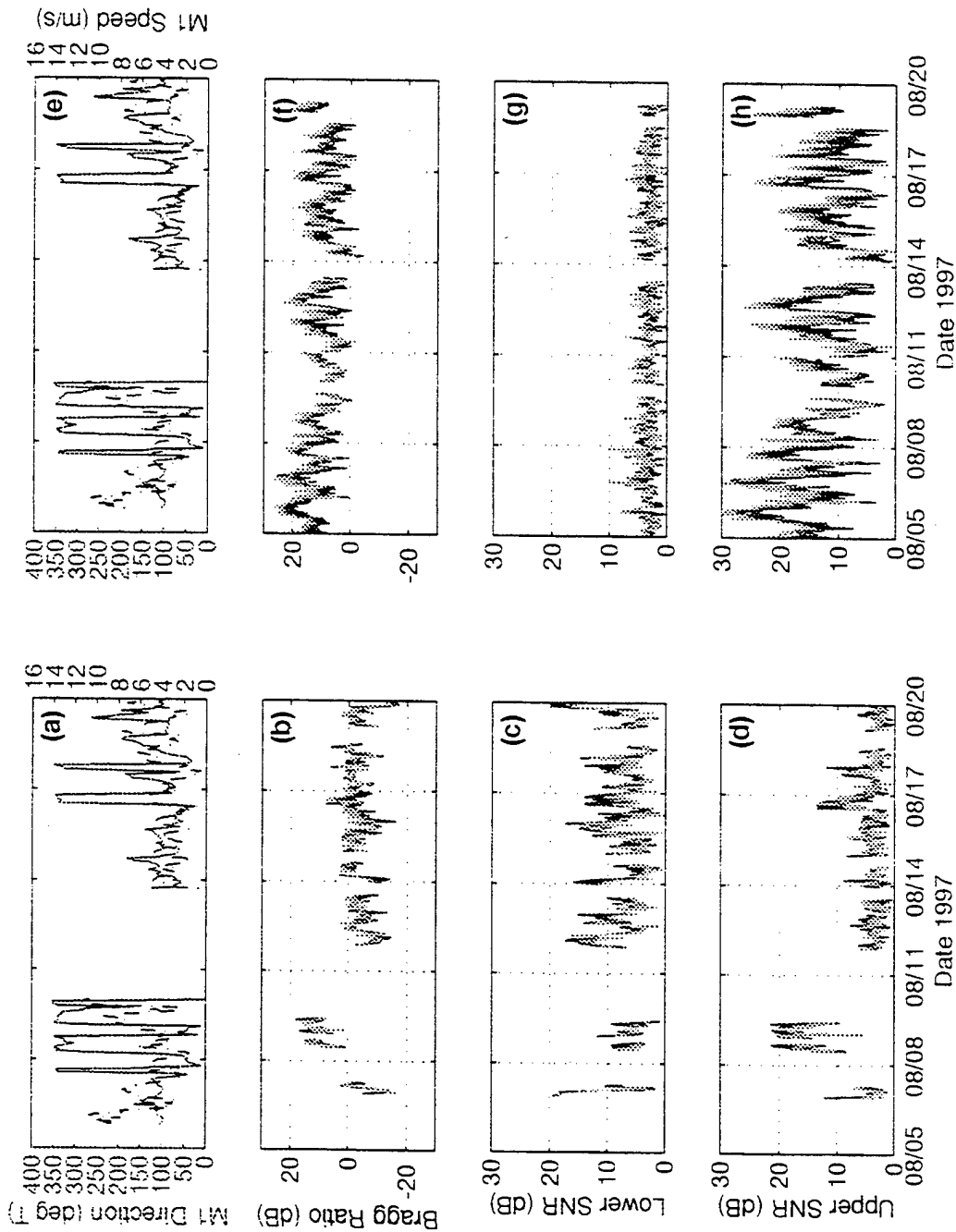
**Figure 23.** Mooring M1 and MCR channel 2 measurements from 21 June to 6 July 1997. (a) and (e) mooring M1 wind direction and speed followed by the Santa Cruz (b) Bragg ratio; (c) lower side peak power [solid] and noise [dashed]; (d) upper side peak power [solid] and noise [dashed]. The right column shows the Moss Landing (f) Bragg ratio; (g) lower side peak power [solid] and noise [dashed]; (h) upper side peak power [solid] and noise [dashed].

67
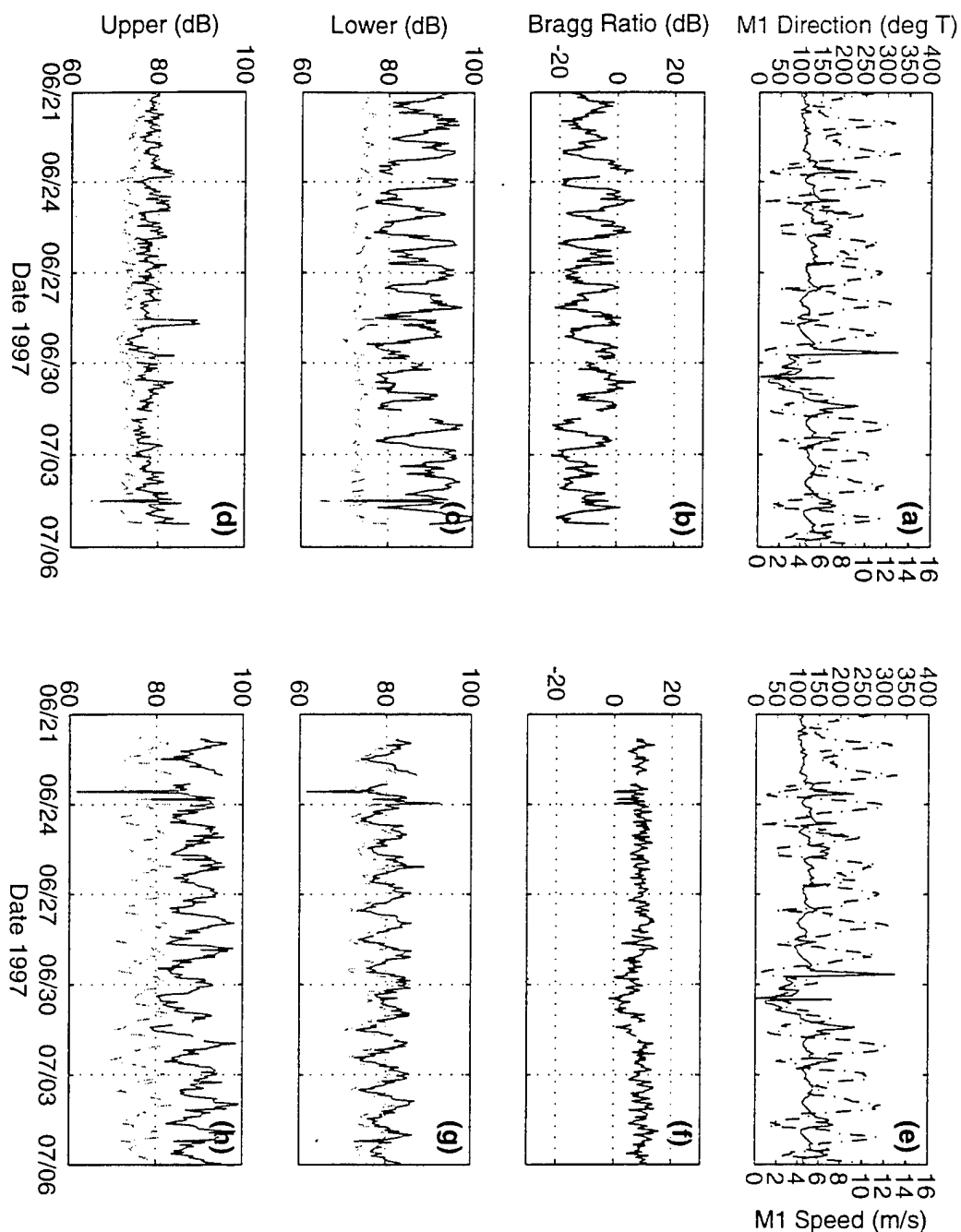
**Figure 24.** Mooring M1 and MCR channel 3 measurements from 21 June to 6 July 1997. (a) and (e) mooring M1 wind direction and speed followed by the Santa Cruz (b) Bragg ratio; (c) lower side peak power [solid] and noise [dashed]; (d) upper side peak power [solid] and noise [dashed]. The right column shows the Moss Landing (f) Bragg ratio; (g) lower side peak power [solid] and noise [dashed]; (h) upper side peak power [solid] and noise [dashed].
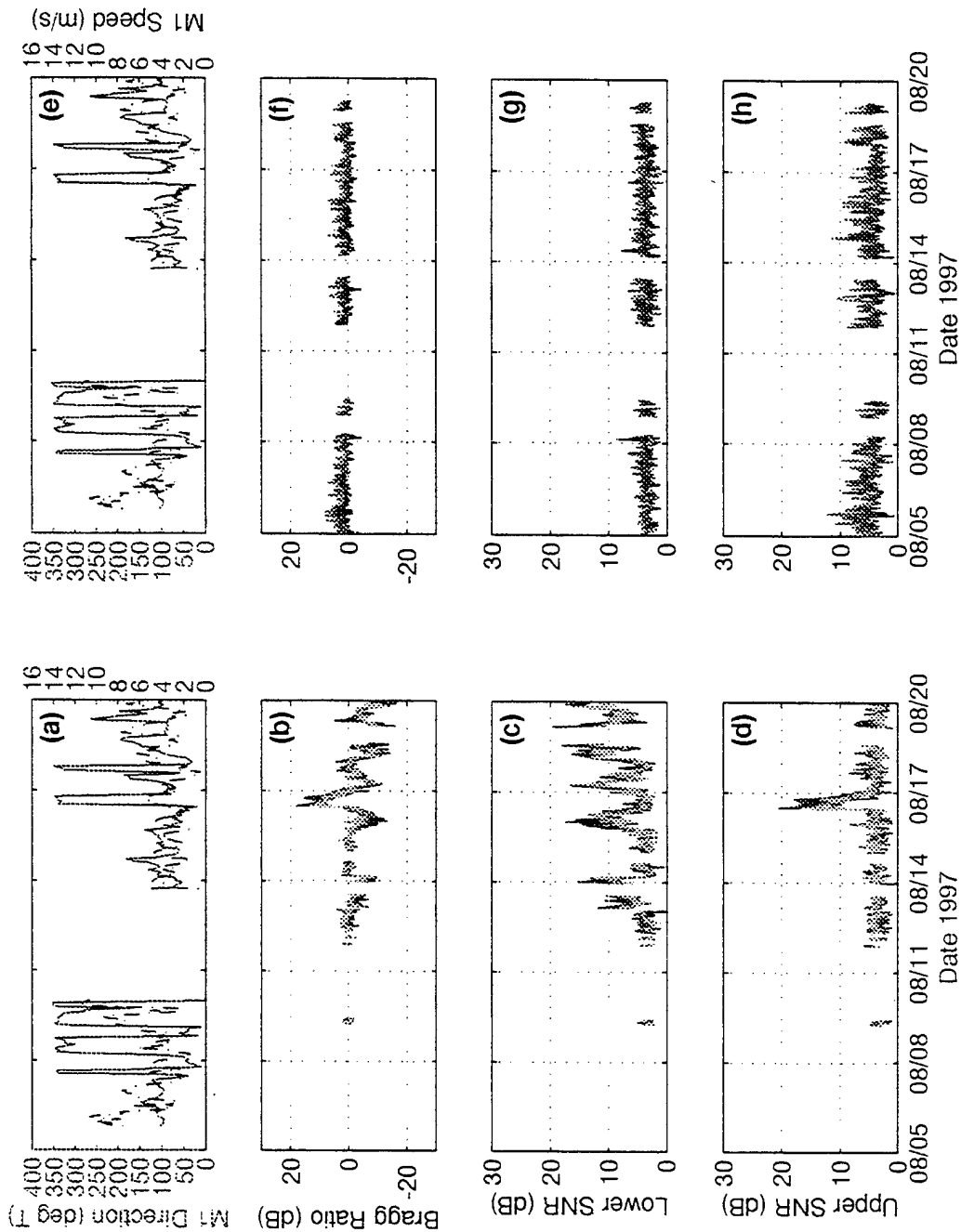
**Figure 25.** Mooring M1 and MCR channel 4 measurements from 21 June to 6 July 1997. (a) and (e) mooring M1 wind direction and speed followed by the Santa Cruz (b) Bragg ratio; (c) lower side peak power [solid] and noise [dashed]; (d) upper side peak power [solid] and noise [dashed]. The right column shows the Moss Landing (f) Bragg ratio; (g) lower side peak power [solid] and noise [dashed]; (h) upper side peak power [solid] and noise [dashed].

69

**Figure 26.** Mooring M1 and MCR channel 1 measurements from 5 to 20 August 1997. (a) and (e) mooring M1 wind direction and speed followed by the Santa Cruz (b) Bragg ratio; (c) lower side signal-to-noise; (d) upper side signal-to-noise. The right column shows the Moss Landing (f) Bragg ratio; (g) lower side signal-to-noise; (h) upper side signal-to-noise.

70

**Figure 27.** Mooring M1 and MCR channel 2 measurements from 5 to 20 August 1997. (a) and (e) mooring M1 wind direction and speed followed by the Santa Cruz (b) Bragg ratio; (c) lower side signal-to-noise; (d) upper side signal-to-noise. The right column shows the Moss Landing (f) Bragg ratio; (g) lower side signal-to-noise; (h) upper side signal-to-noise.

71

**Figure 28.** Mooring M1 and MCR channel 3 measurements from 5 to 20 August 1997. (a) and (e) mooring M1 wind direction and speed followed by the Santa Cruz (b) Bragg ratio; (c) lower side signal-to-noise; (d) upper side signal-to-noise. The right column shows the Moss Landing (f) Bragg ratio; (g) lower side signal-to-noise; (h) upper side signal-to-noise.

72

**Figure 29.** Mooring M1 and MCR channel 4 measurements from 5 to 20 August 1997. (a) and (e) mooring M1 wind direction and speed followed by the Santa Cruz (b) Bragg ratio; (c) lower side signal-to-noise; (d) upper side signal-to-noise. The right column shows the Moss Landing (f) Bragg ratio; (g) lower side signal-to-noise; (h) upper side signal-to-noise.

73

**Figure 30.** Mooring M1 and MCR channel 3 measurements from 5 to 20 August 1997..
(a) and (e) mooring M1 wind direction and speed followed by the Santa Cruz (b) Bragg
ratio; (c) lower side peak power [solid] and noise [dashed]; (d) upper side peak power
[solid] and noise [dashed]. The right column shows the Moss Landing (f) Bragg ratio;
(g) lower side peak power [solid] and noise [dashed]; (h) upper side peak power [solid]
and noise [dashed].
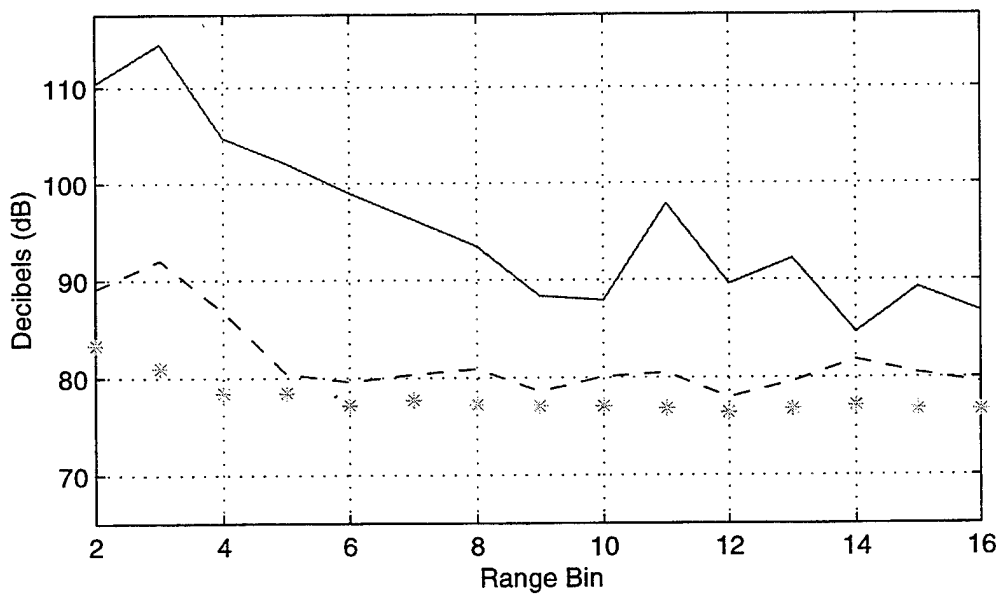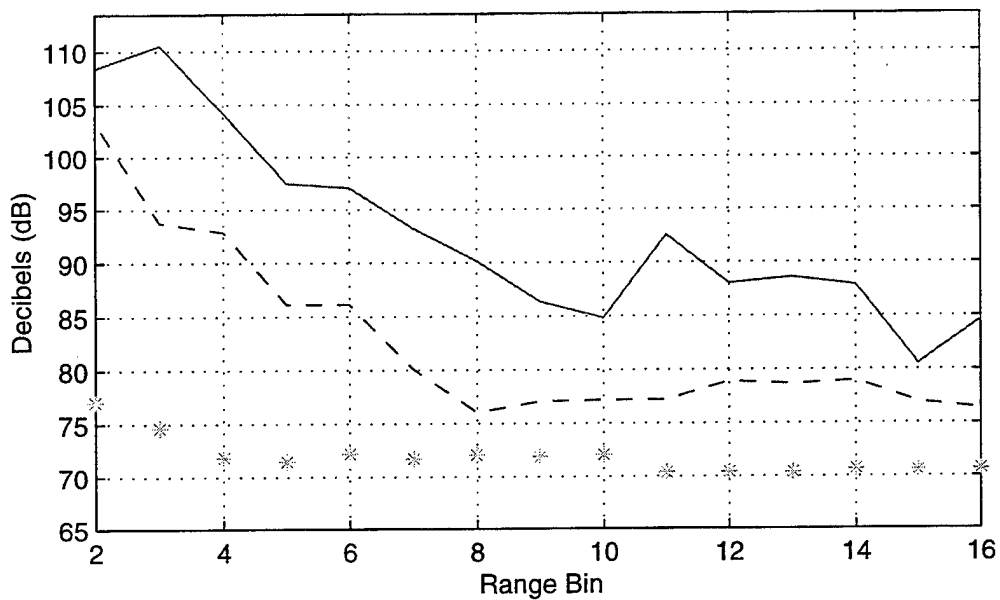
**Figure 31.** Upper side [solid], lower side [dashed] Bragg peak power levels and noise level [asterisks] vs. range bin when the mooring wind direction was towards the radar broadside for Santa Cruz MCR channel 3 at 1200 on 16 August 1997 (top) and Moss Landing MCR channel 3 at 2100 on 27 June 1997 (bottom).
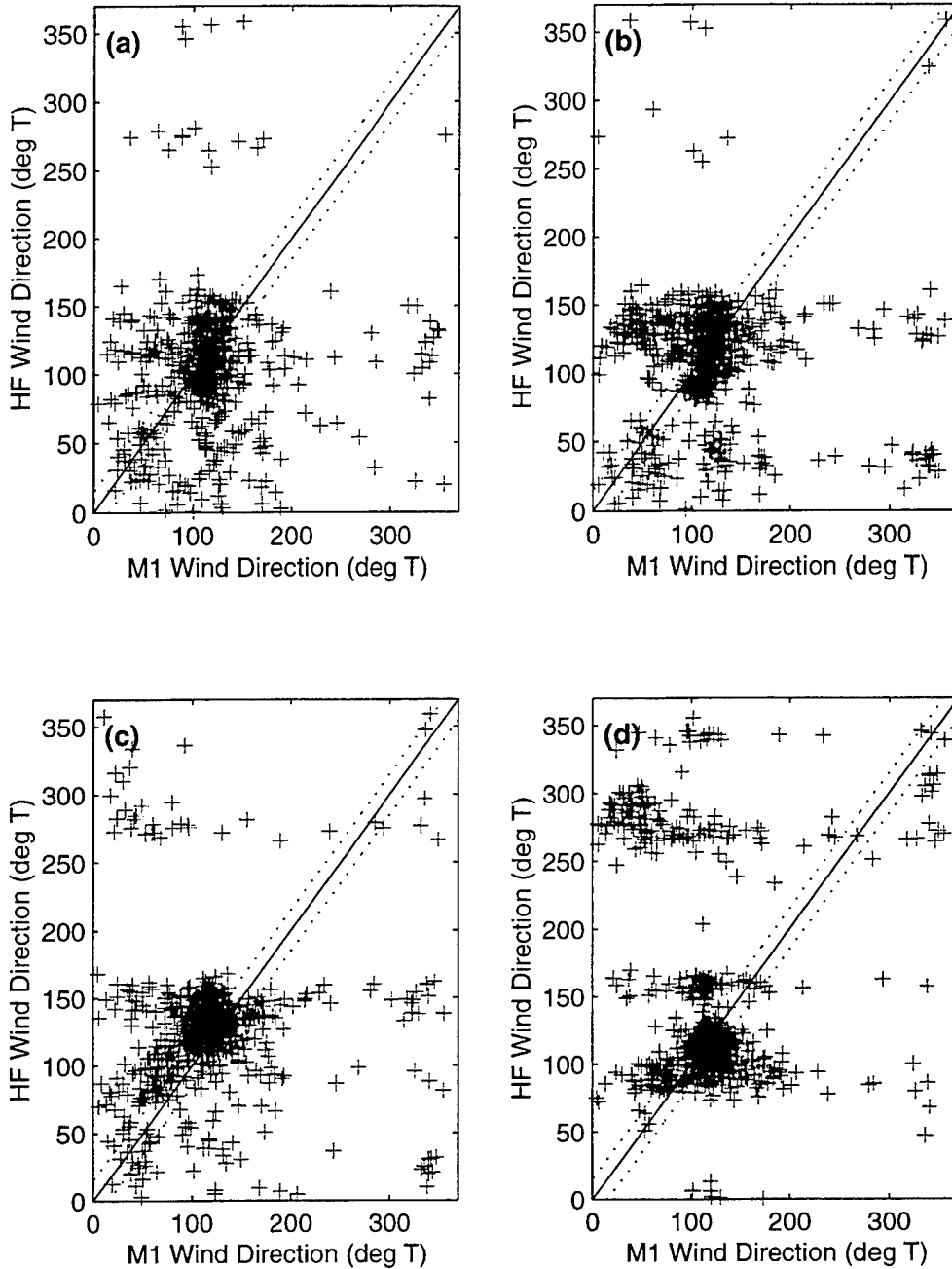
**Figure 32.** Scatter plot that compares the mooring M1 measured wind direction (abscissa) and MCR-derived wind direction (ordinate) at the nearest point to M1 for channel 1 (a), channel 2 (b), channel 3 (c), and channel 4 (d). Measurements are in oceanography convention. The solid diagonal line show perfect agreement between the platforms and the dotted lines show ±15° difference. The signal-to-noise (SNR) threshold is 3 dB in this case.
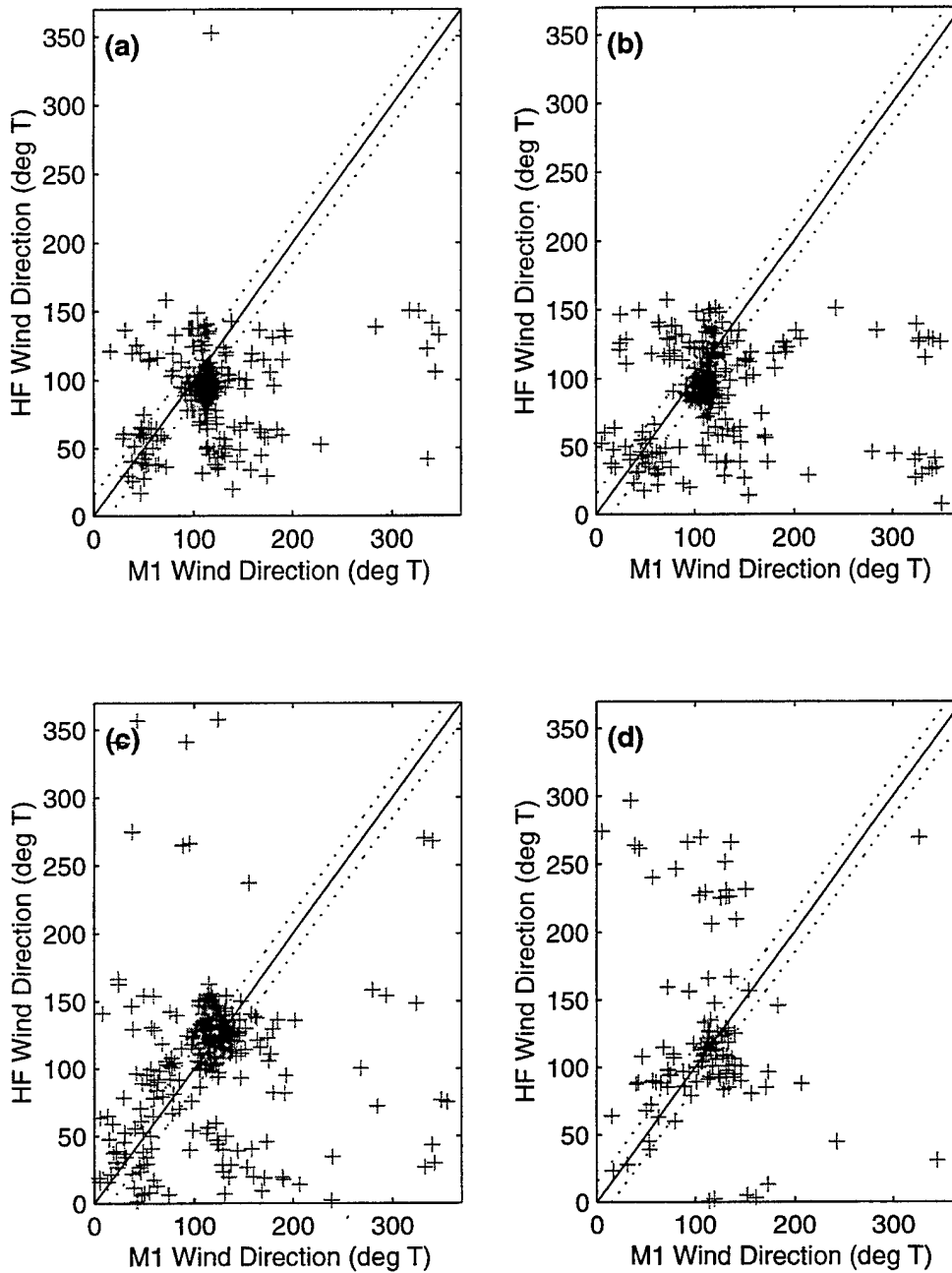
**Figure 33.** Scatter plot that compares the mooring M1 measured wind direction (abscissa) and MCR-derived wind direction (ordinate) at the nearest point to M1 for channel 1 (a), channel 2 (b), channel 3 (c), and channel 4 (d). The signal-to-noise (SNR) threshold is 5 dB in this case.
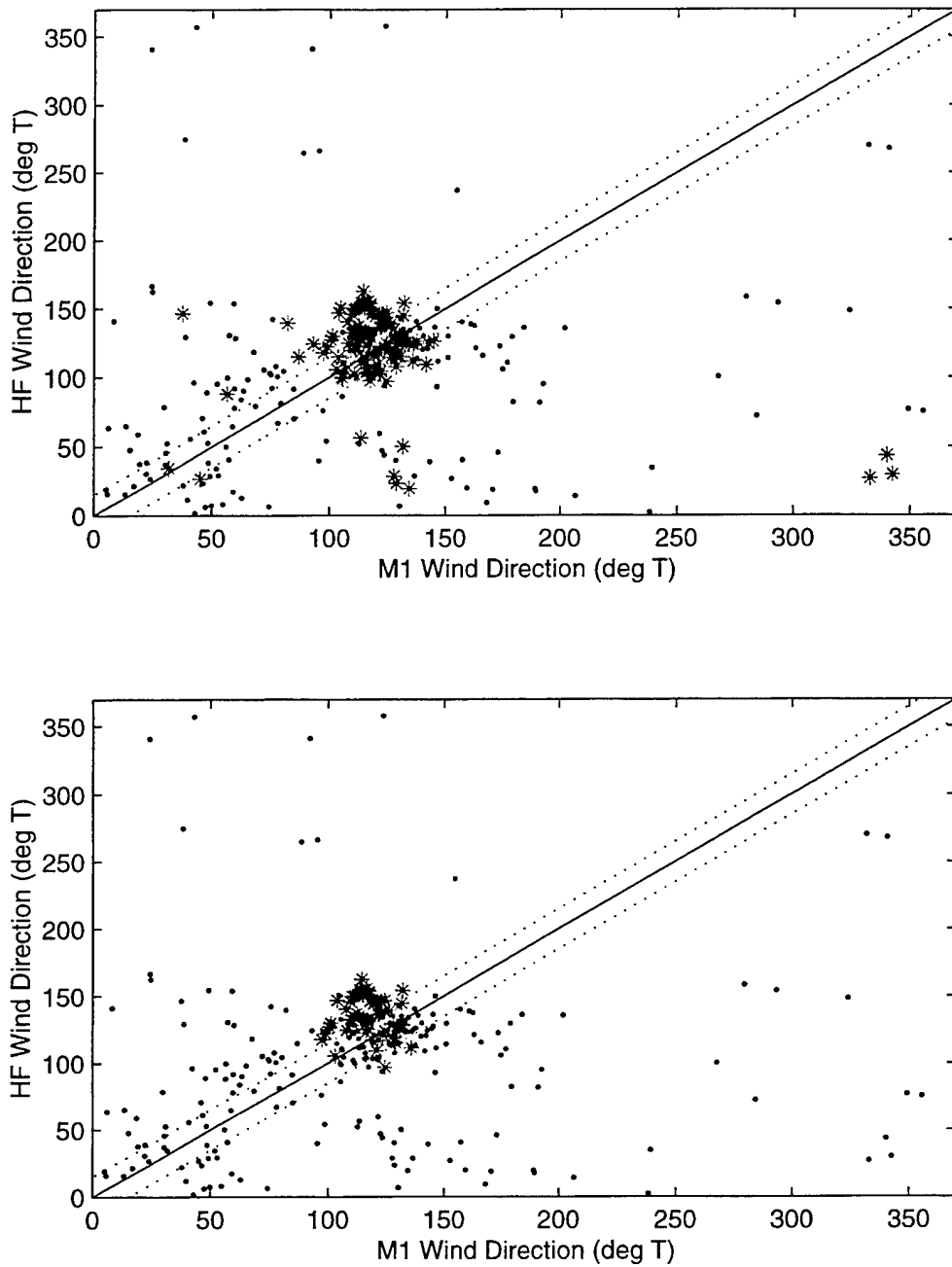
**Figure 34.** Scatter plot showing channel 3 data (at SNR threshold = 3 dB) sub-divided into high wind speed ( >5 m s$^{-1}$) [asterisks] and low wind conditions [crosses] (top). The lower panel shows the difference when the wind speed threshold is increased to 7.5 m s$^{-1}$.
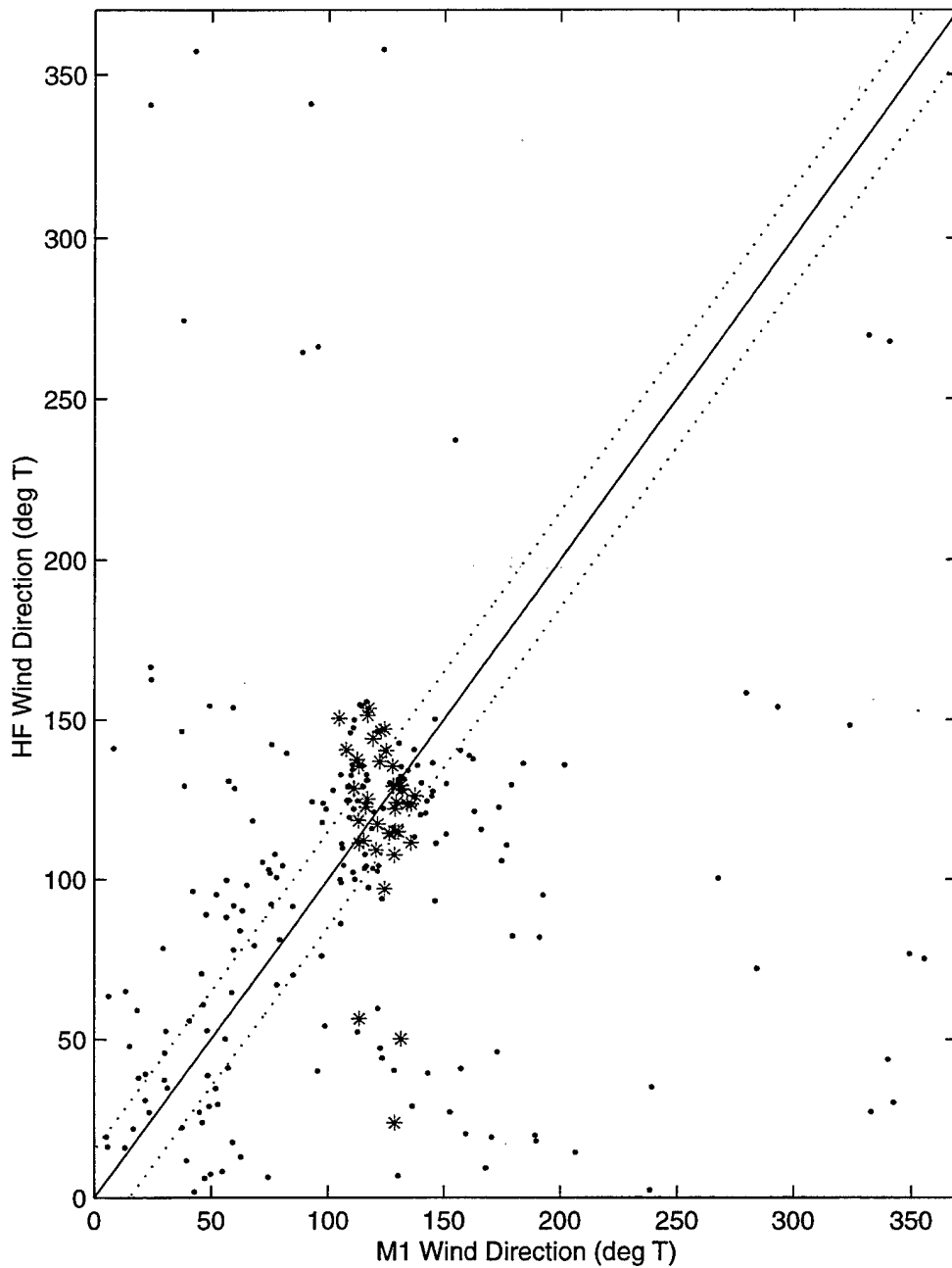
**Figure 35.** Scatter plot showing channel 3 high wind data (at SNR threshold = 3 dB) sub-divided into long duration (>12 h) [asterisks] and shorter duration wind conditions [crosses].
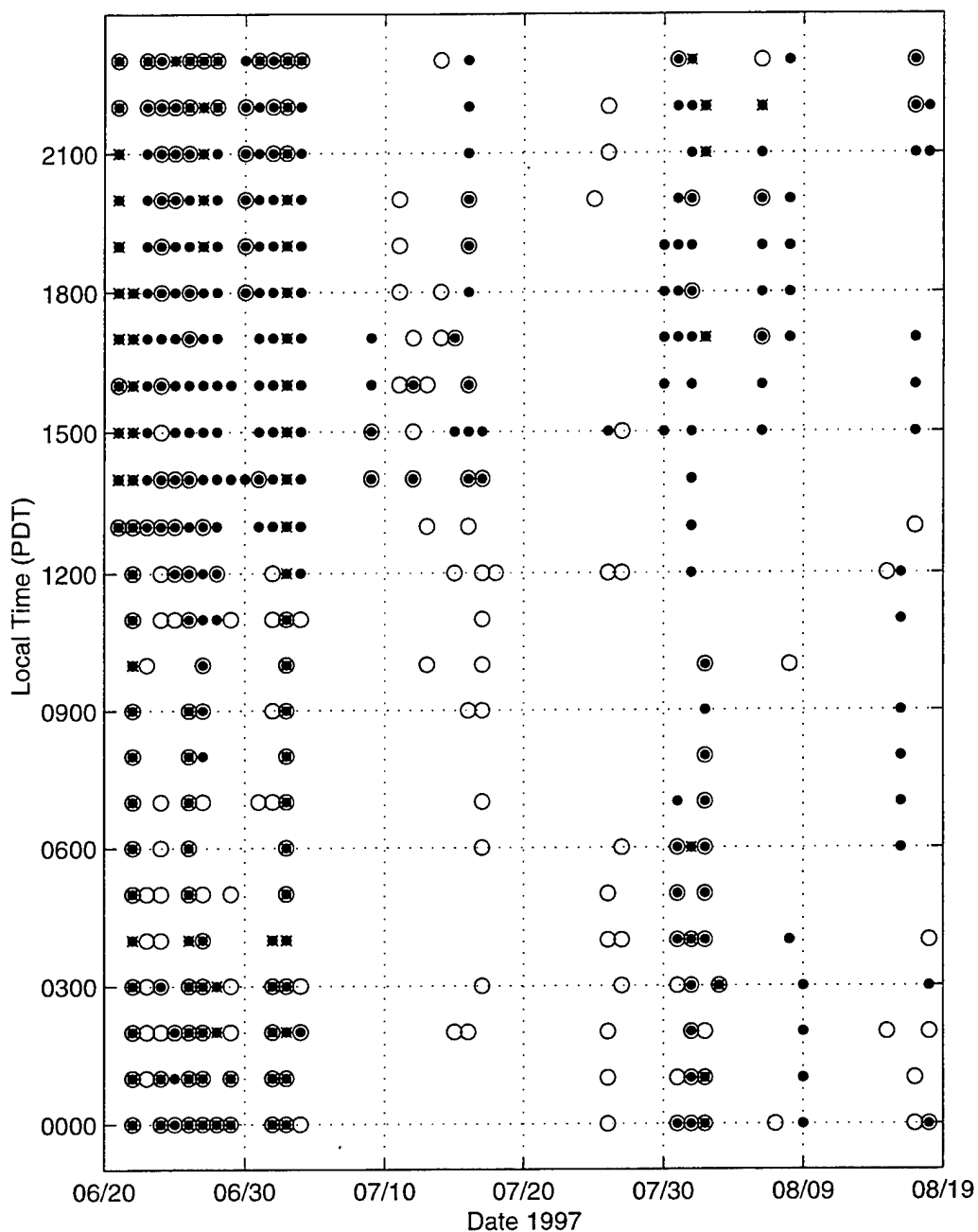
**Figure 36.** Listing by hour when channel 3 radar-derived wind directions agreed to within 15° of the mooring measurement [circles], when the mooring wind speed was greater than 5 m s-1 [crosses], and when high winds duration was greater than 12 h [dots]. data was concurrently available from both MCR sites during summer 1997 for channel 3 (top) and channel 4 (bottom).

80
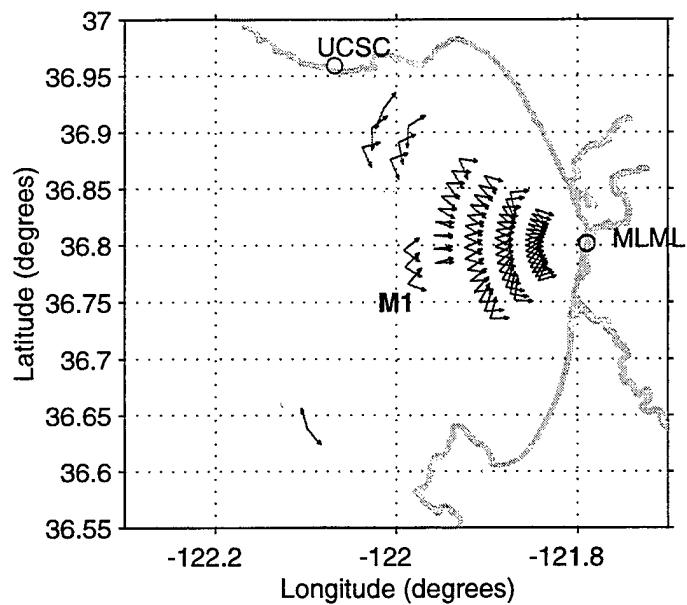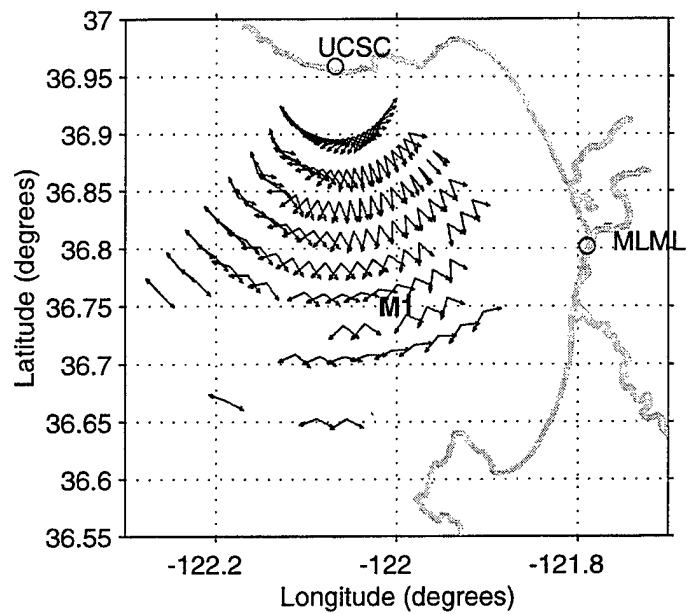
**Figure 37.** Left and right radar directions solutions for 1600 PDT, 24 June 1997 for the Santa Cruz MCR (top) and Moss Landing MCR (bottom) with the SNR threshold set at 5 dB.
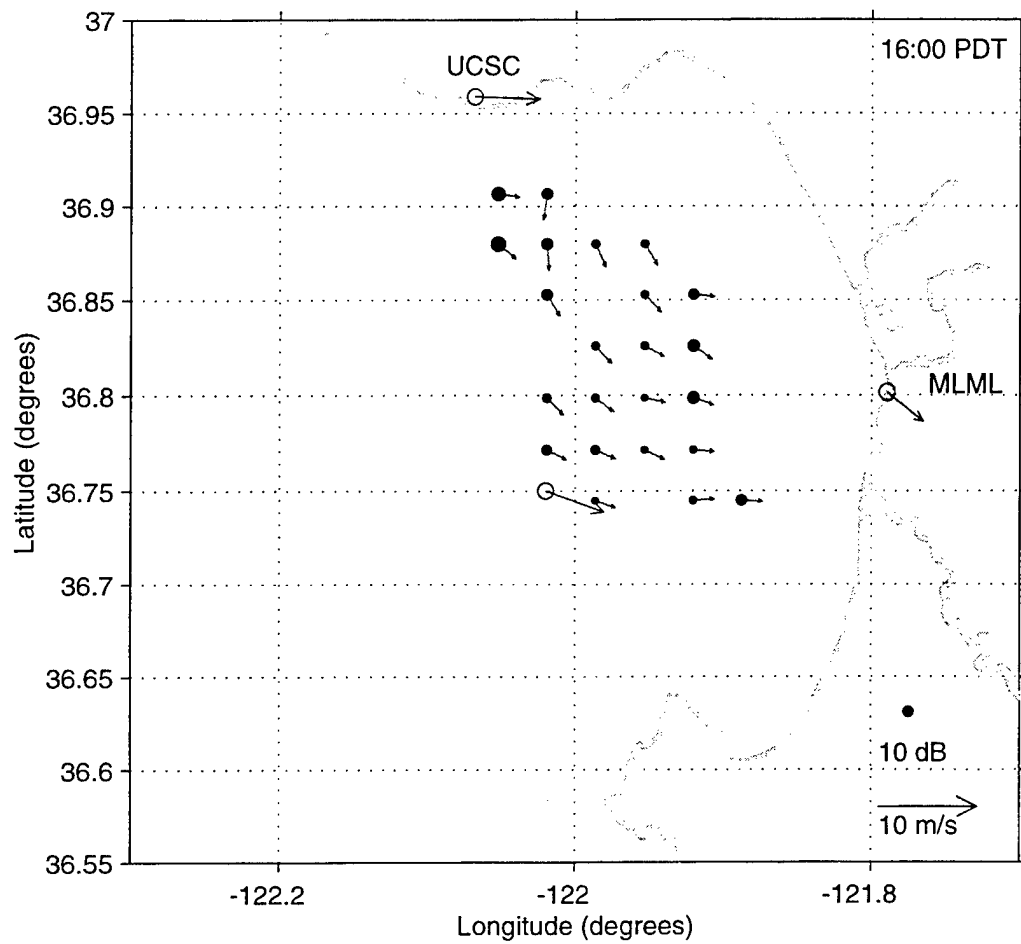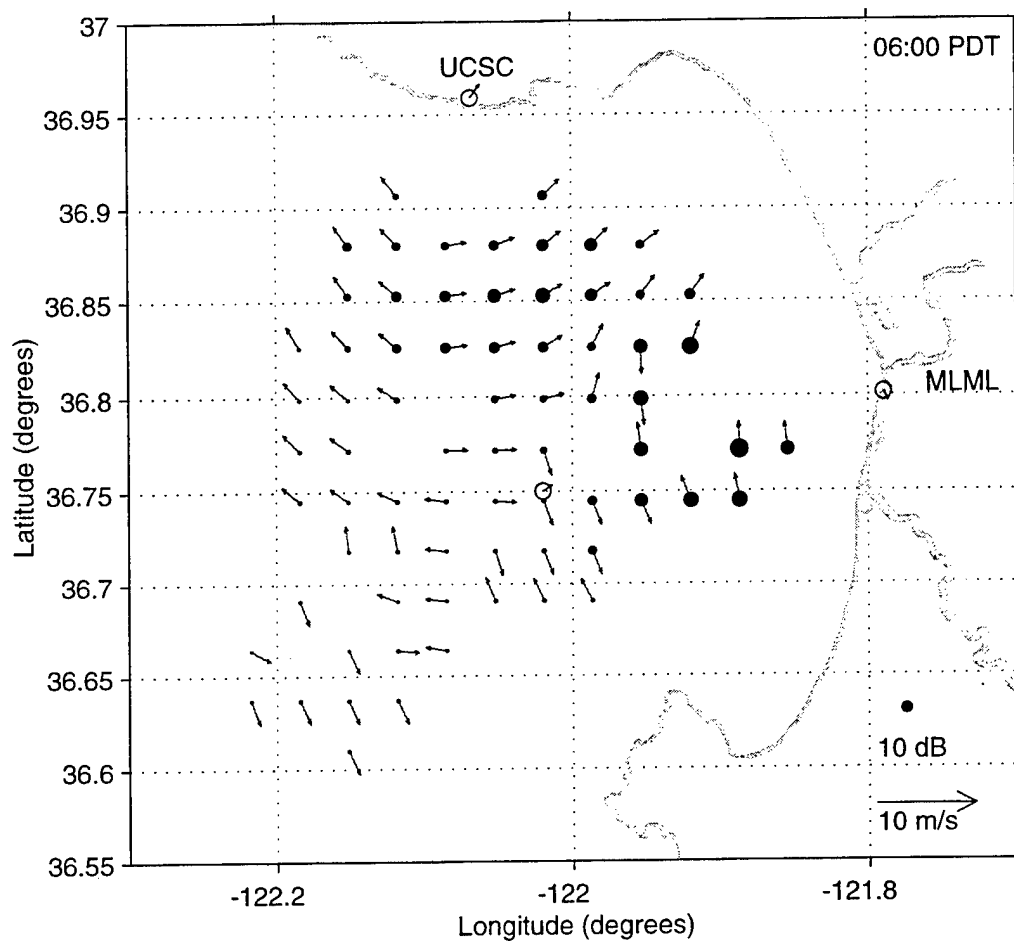
**Figure 38.** Radar-derived wind directions on 1600 PDT, 24 June 1997 computed from the wind-retrieval algorithm based on a SNR criteria of 5 dB. The dots indicate the average SNR of the radar solution selected at each grid point. The vectors show the wind observations at the MBARI M1 mooring, Moss Landing (MLML) and Santa Cruz (UCSC).
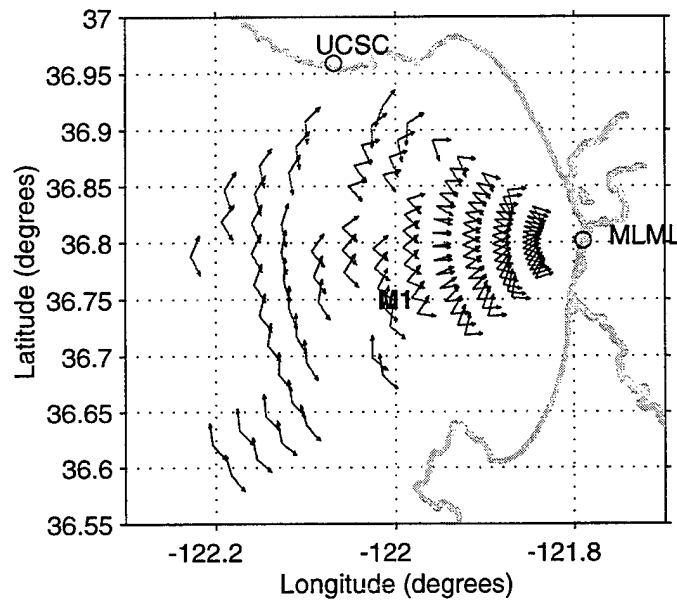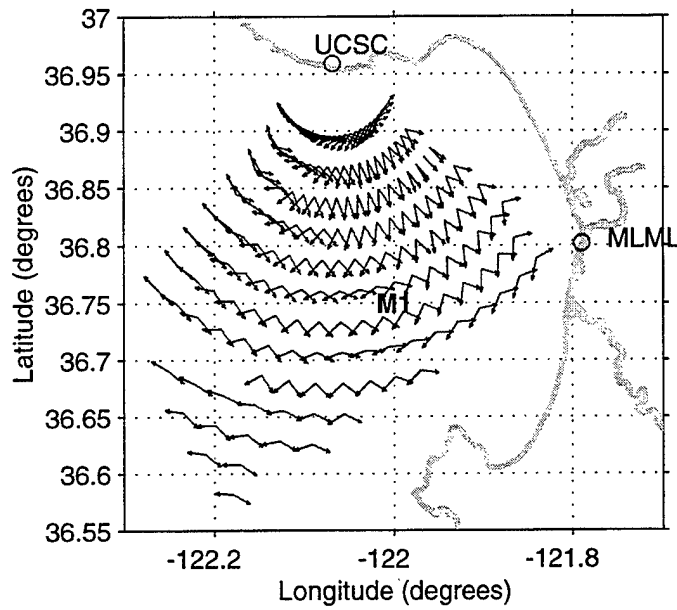
**Figure 39.** Left and right radar directions solutions for 1600 PDT, 24 June 1997 for the Santa Cruz MCR (top) and Moss Landing MCR (bottom) with the SNR threshold set at 3 dB.

83
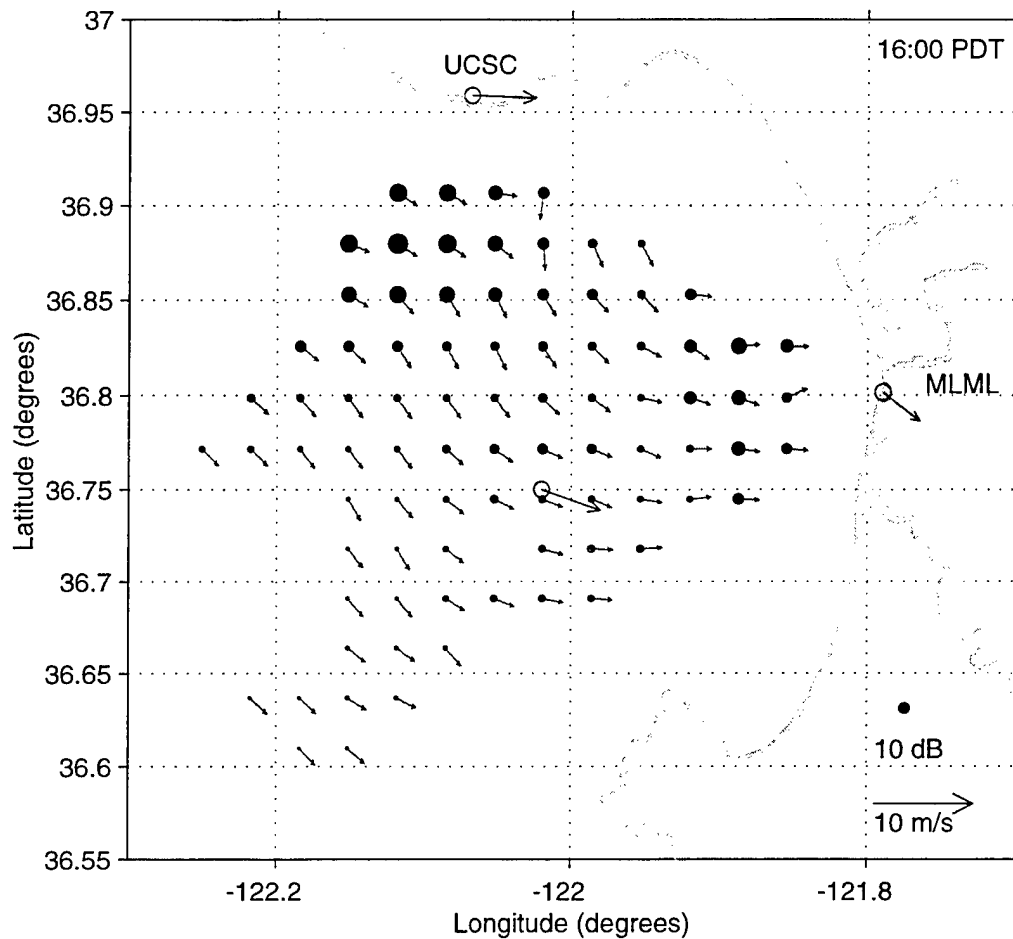
**Figure 40.** Radar-derived wind directions 1600 PDT, 24 June 1997 computed from the wind-retrieval algorithm based on a SNR criteria of 3 dB. The dots indicate the average SNR of the radar solution selected at each grid point. The vectors show the wind observations at the MBARI M1 mooring, Moss Landing (MLML) and Santa Cruz (UCSC).
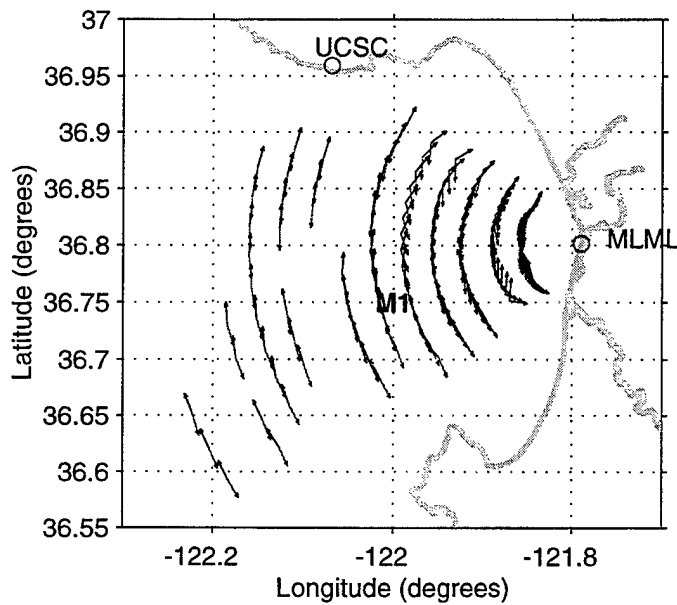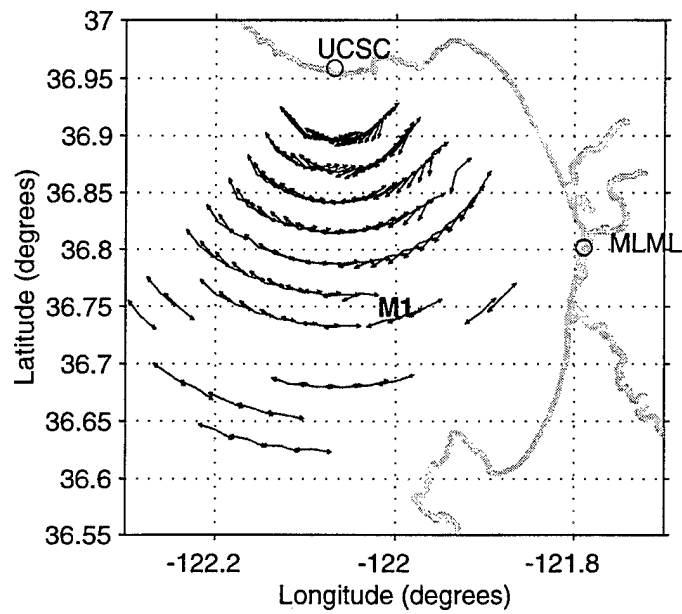
**Figure 41**. Left and right radar directions solutions for 0600 PDT, 14 July 1997 for the Santa Cruz MCR (top) and Moss Landing MCR (bottom) with the SNR threshold set at 3 dB.
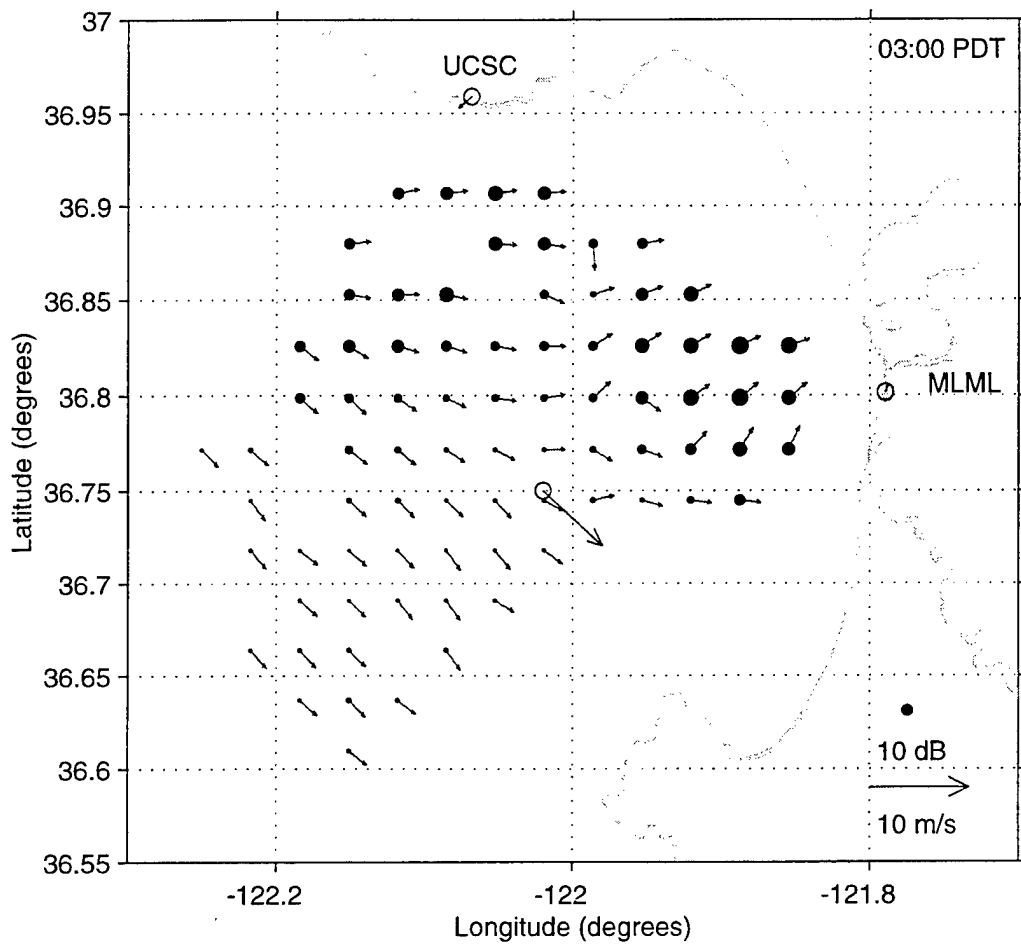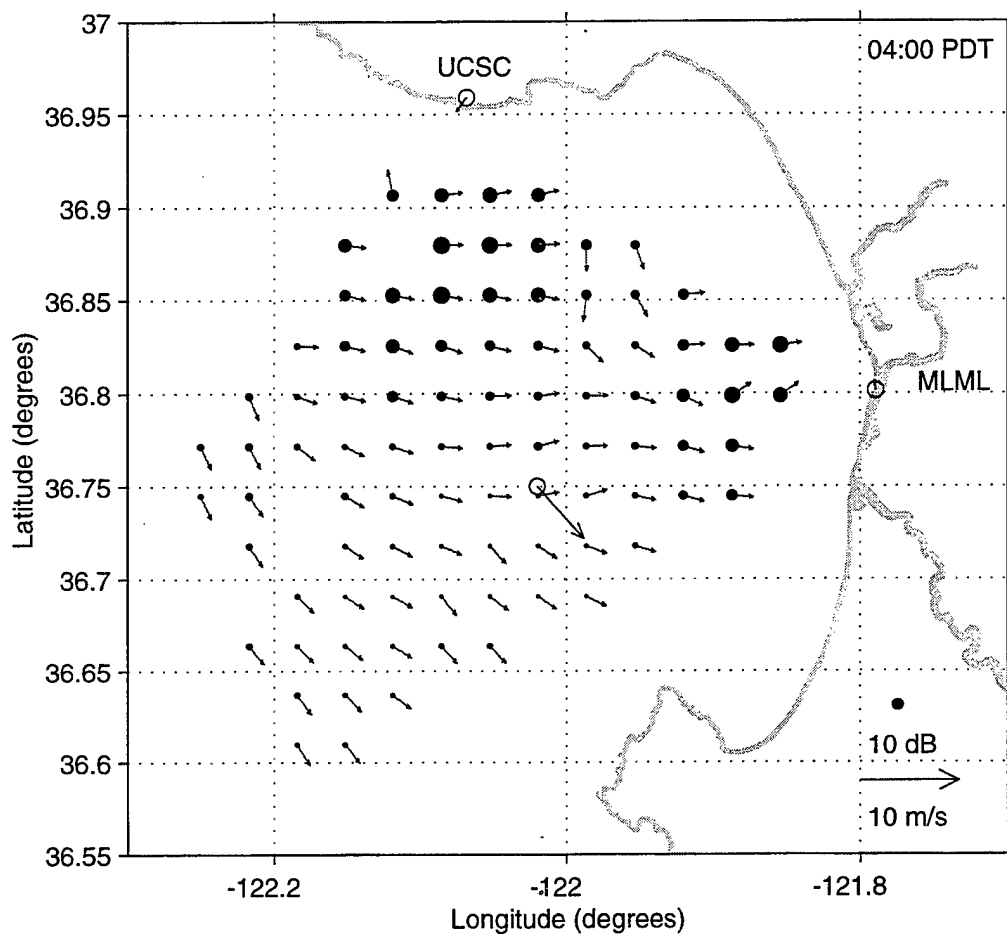
**Figure 42.** Radar-derived wind directions and in-situ observations at the MBARI M1 mooring, Moss Landing (MLML) and Santa Cruz (UCSC) for 0600 PDT, 14 July 1997, during low wind conditions when the radar-derived wind directions are least accurate.
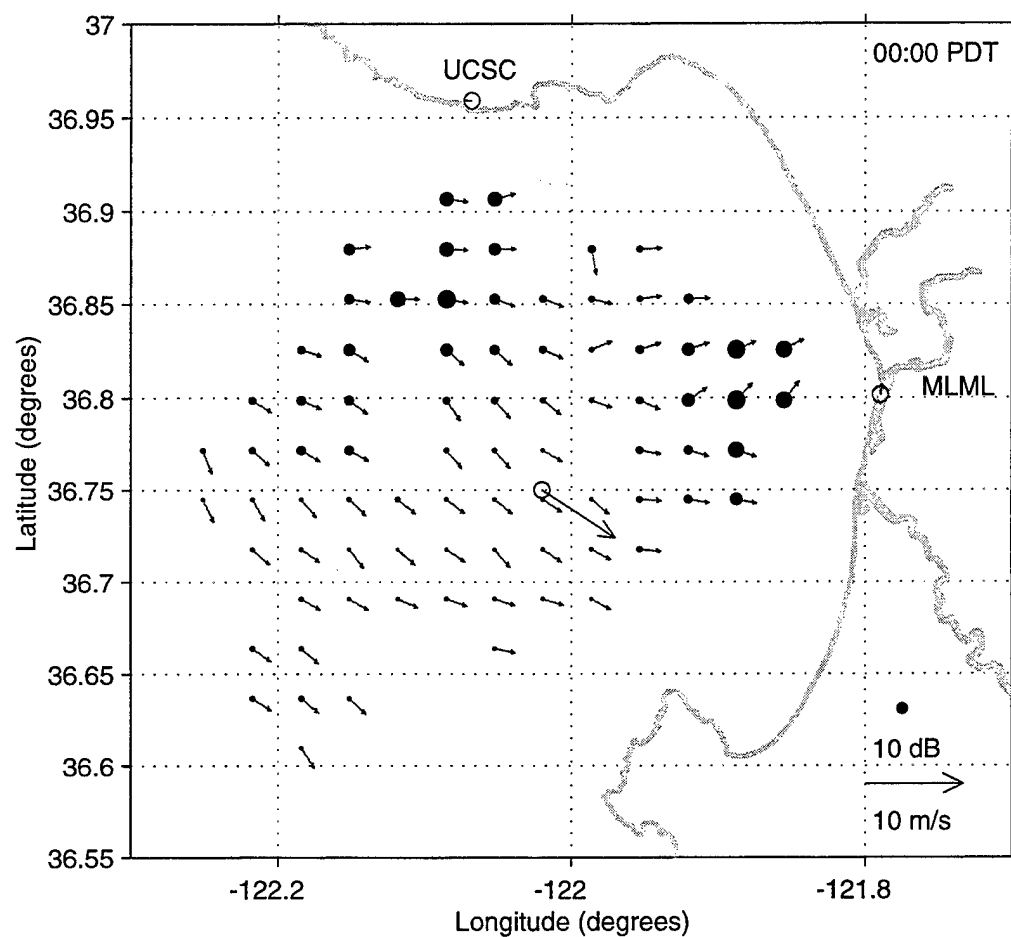
**Figure 43.** Radar-derived wind directions and in-situ observations at the MBARI M1 mooring, Moss Landing (MLML) and Santa Cruz (UCSC) for 0000 PDT, 27 June 1997.
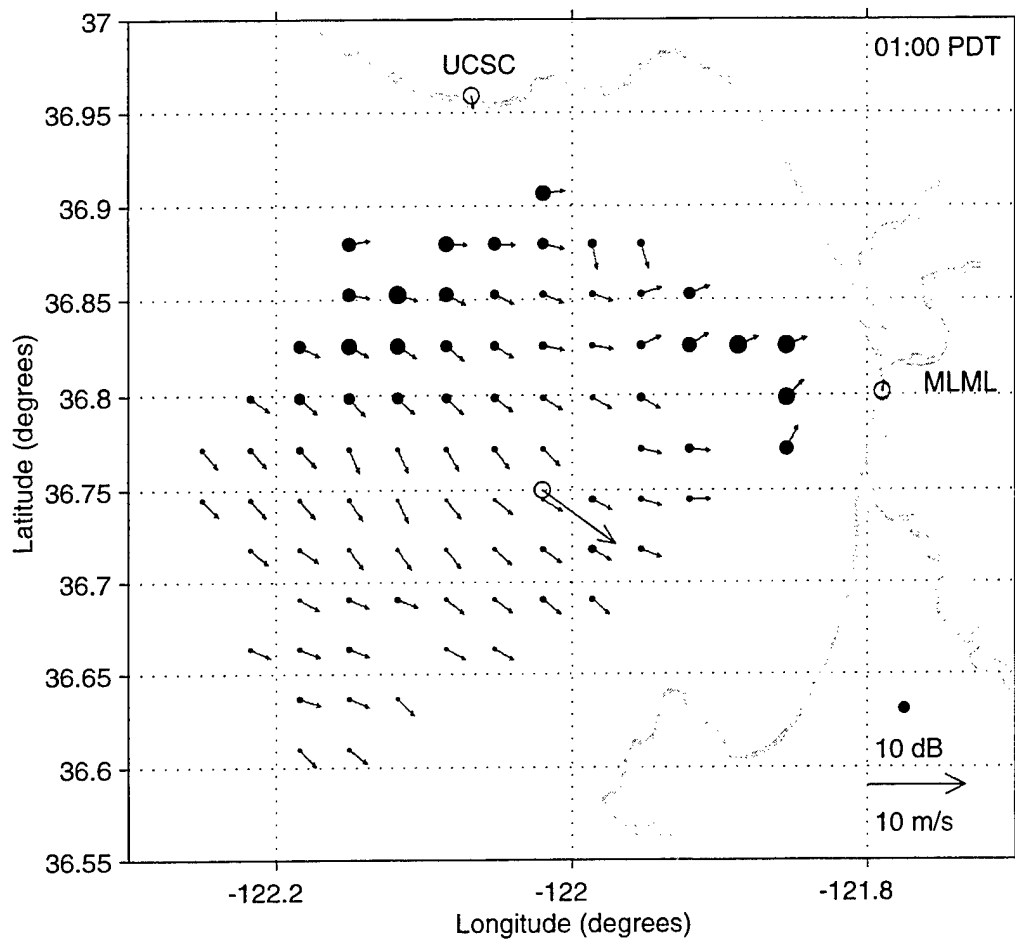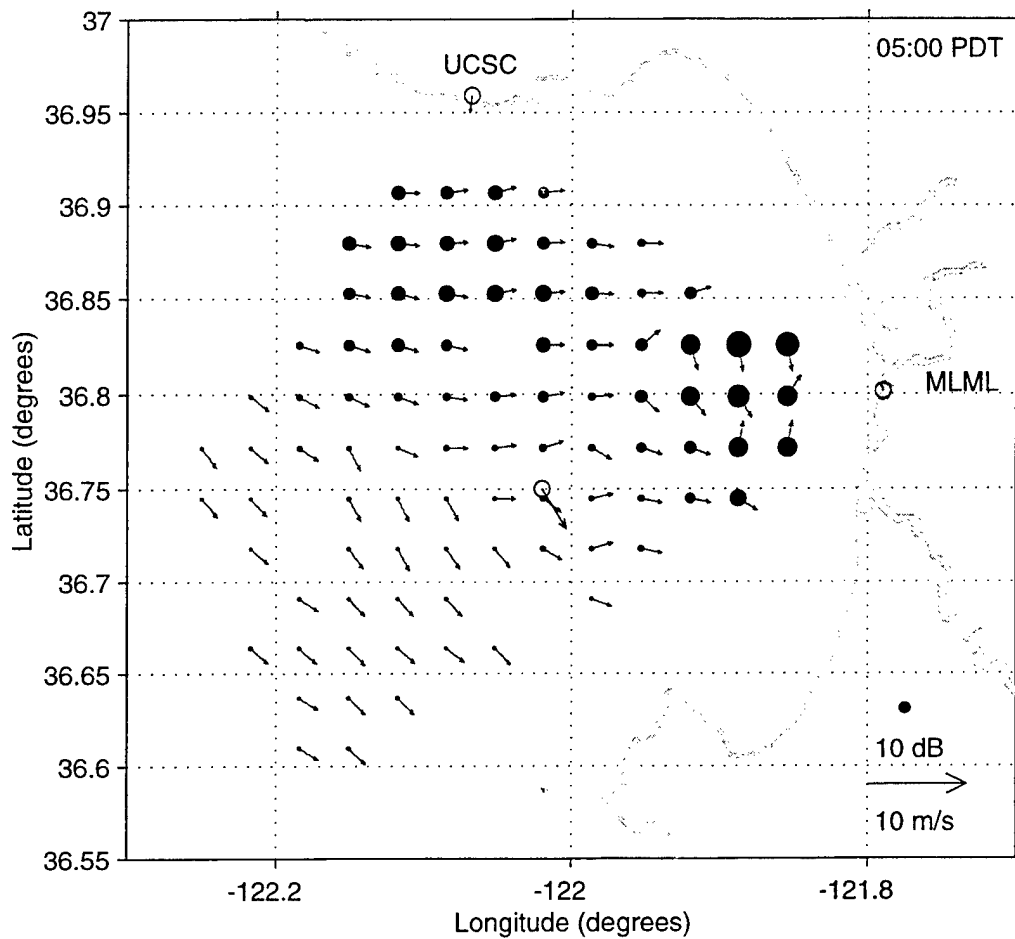
**Figure 44.** Radar-derived wind directions and in-situ observations at the MBARI M1 mooring, Moss Landing (MLML) and Santa Cruz (UCSC) for 0100 PDT, 27 June 1997.
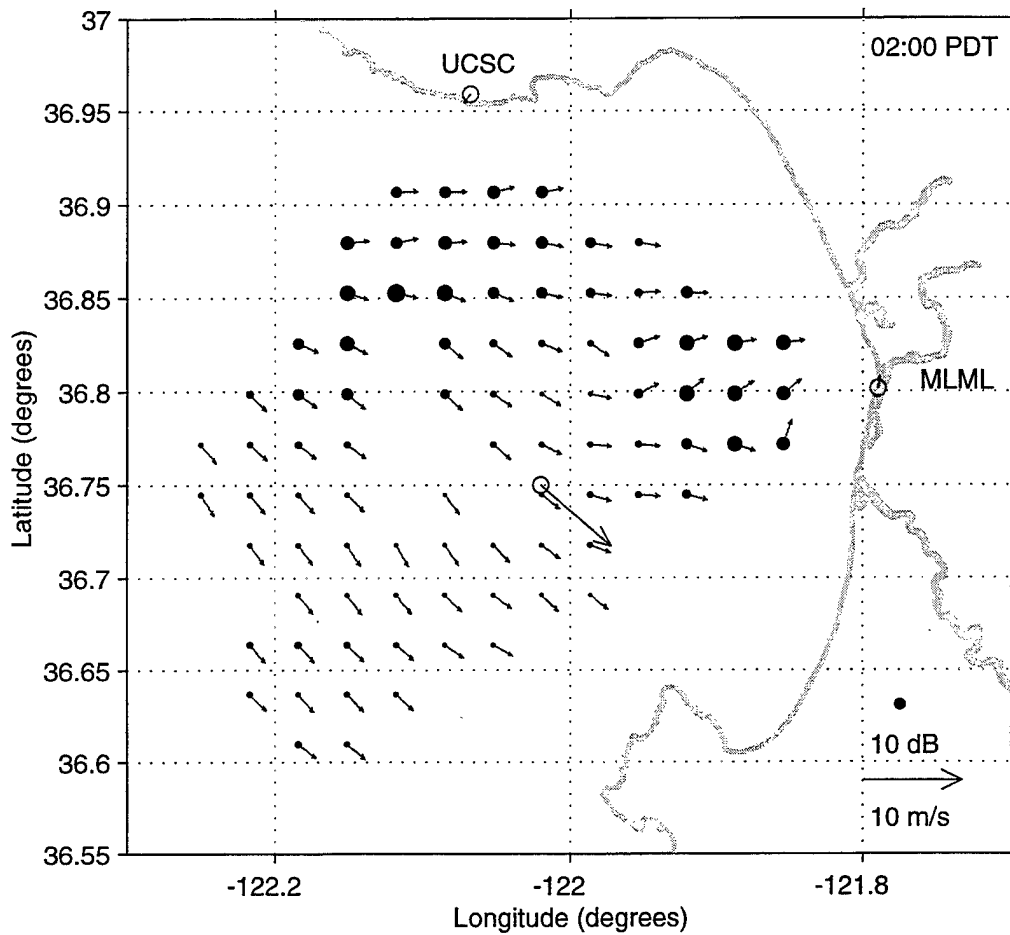
**Figure 45.** Radar-derived wind directions and in-situ observations at the MBARI M1 mooring, Moss Landing (MLML) and Santa Cruz (UCSC) for 0200 PDT, 27 June 1997.
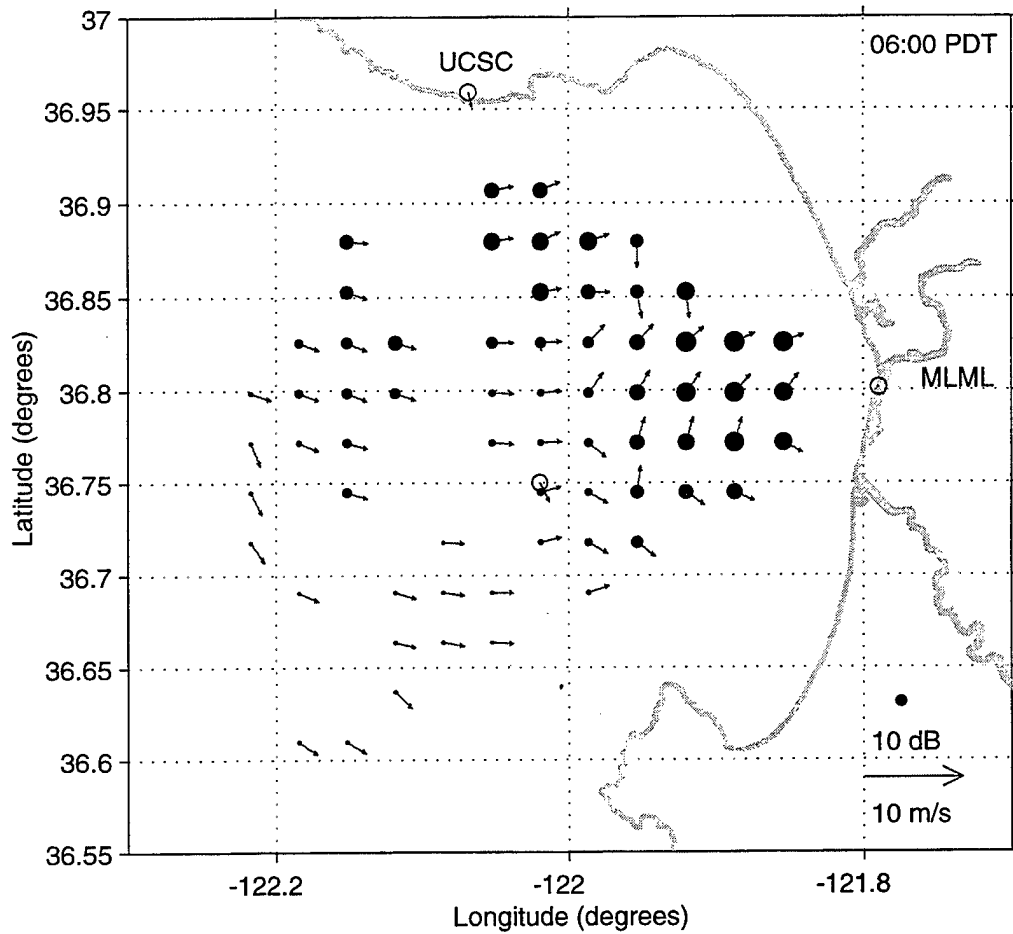
**Figure 46.** Radar-derived wind directions and in-situ observations at the MBARI M1 mooring, Moss Landing (MLML) and Santa Cruz (UCSC) for 0300 PDT, 27 June 1997.

90

**Figure 47.** Radar-derived wind directions and in-situ observations at the MBARI M1 mooring, Moss Landing (MLML) and Santa Cruz (UCSC) for 0400 PDT, 27 June 1997.
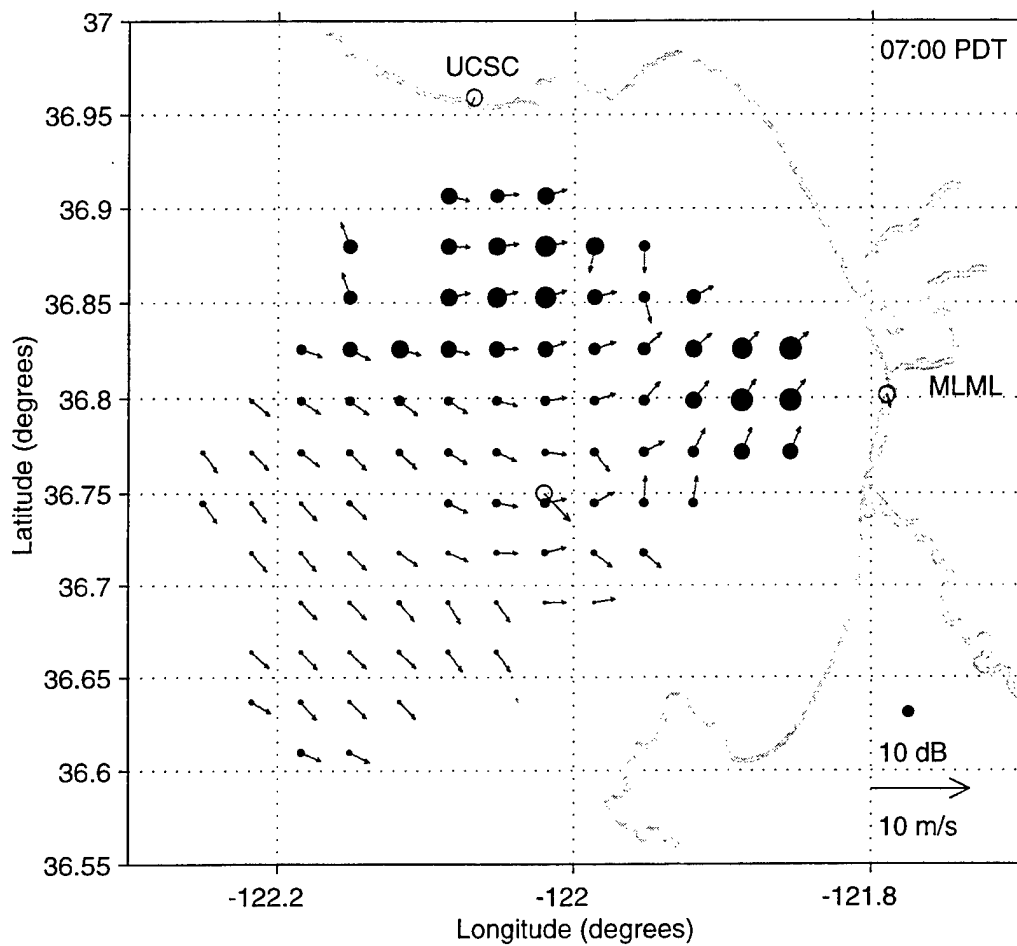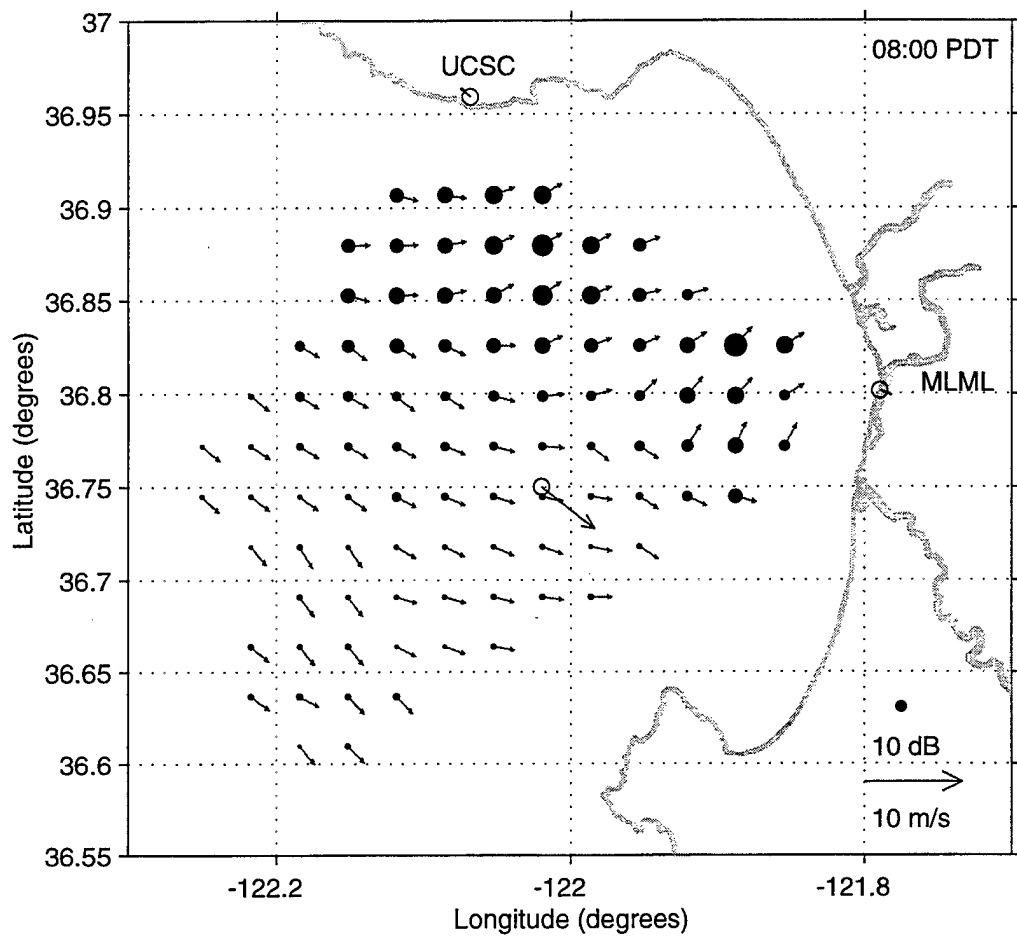
**Figure 48.** Radar-derived wind directions and in-situ observations at the MBARI M1 mooring, Moss Landing (MLML) and Santa Cruz (UCSC) for 0500 PDT, 27 June 1997.

92

**Figure 49**. Radar-derived wind directions and in-situ observations at the MBARI M1 mooring, Moss Landing (MLML) and Santa Cruz (UCSC) for 0600 PDT, 27 June 1997.

**Figure 50.** Radar-derived wind directions and in-situ observations at the MBARI M1 mooring, Moss Landing (MLML) and Santa Cruz (UCSC) for 0700 PDT, 27 June 1997.

**Figure 51.** Radar-derived wind directions and in-situ observations at the MBARI M1 mooring, Moss Landing (MLML) and Santa Cruz (UCSC) for 0800 PDT, 27 June 1997.
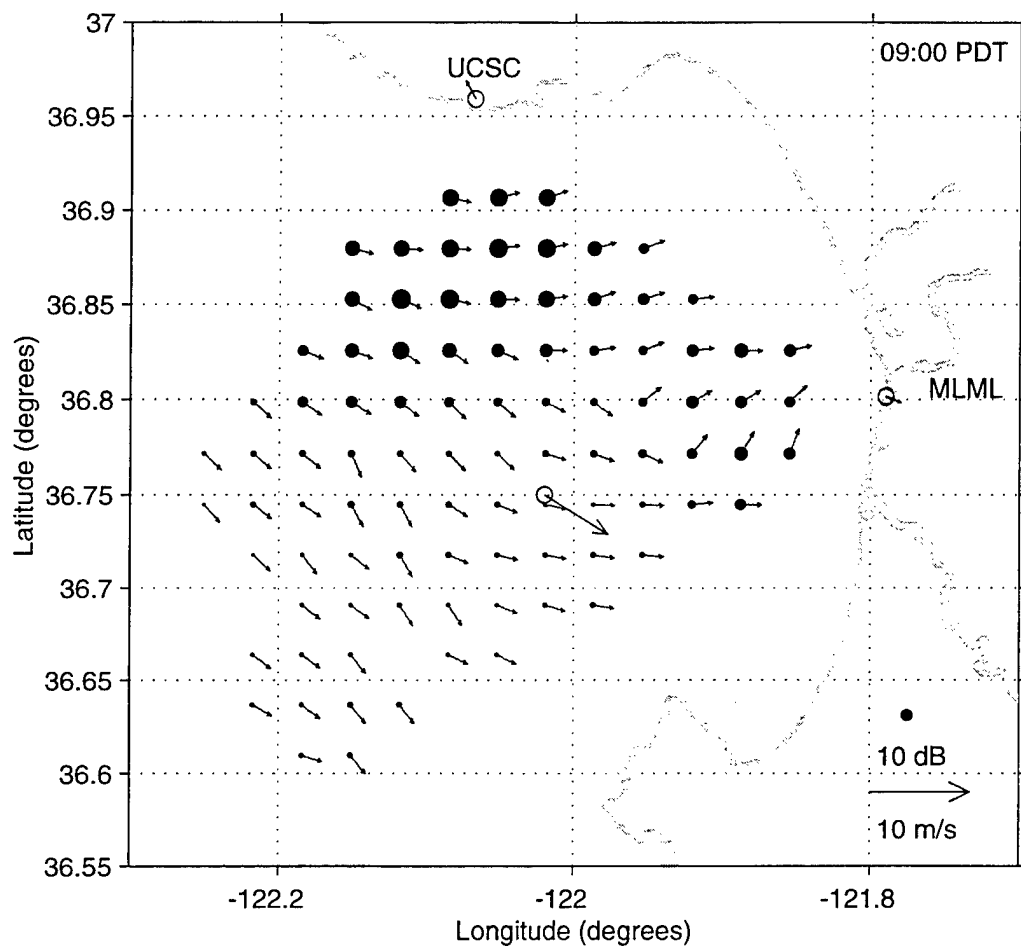
**Figure 52.** Radar-derived wind directions and in-situ observations at the MBARI M1 mooring, Moss Landing (MLML) and Santa Cruz (UCSC) for 0900 PDT, 27 June 1997.
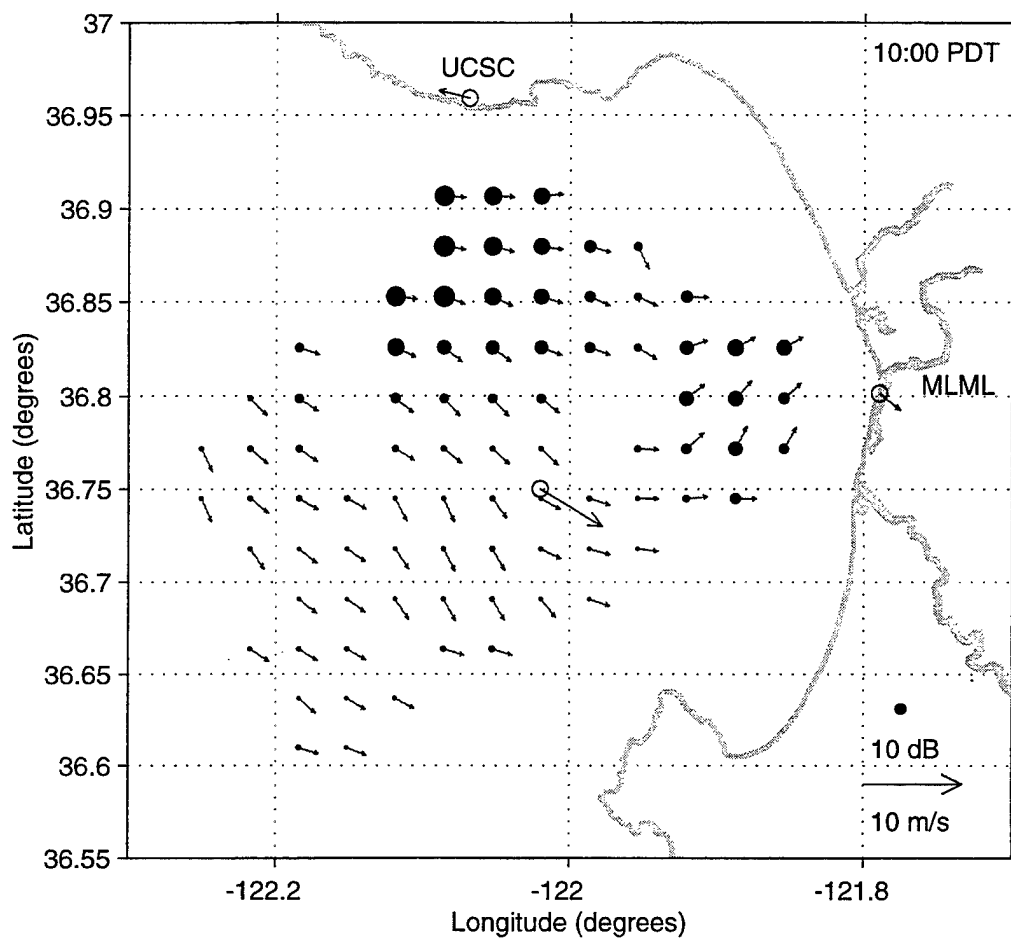
**Figure 53.** Radar-derived wind directions and in-situ observations at the MBARI M1 mooring, Moss Landing (MLML) and Santa Cruz (UCSC) for 1000 PDT, 27 June 1997.
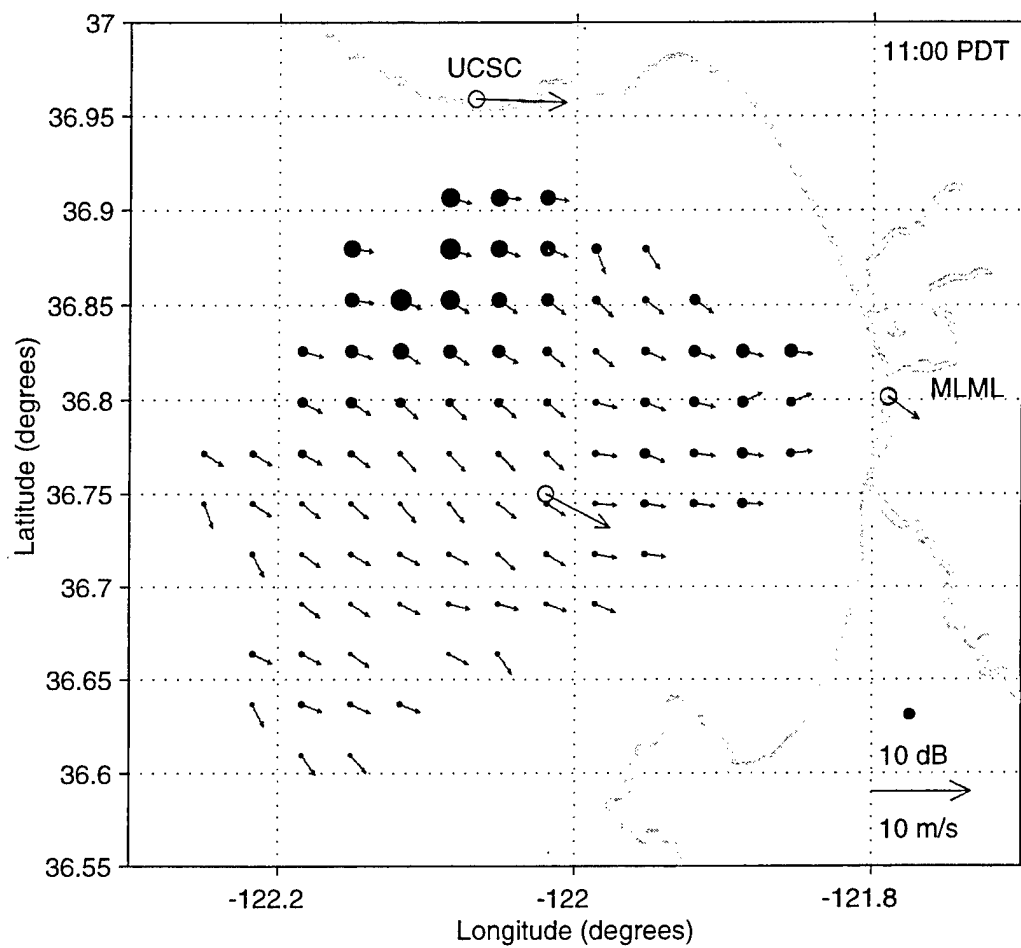
**Figure 54.** Radar-derived wind directions and in-situ observations at the MBARI M1 mooring, Moss Landing (MLML) and Santa Cruz (UCSC) for 1100 PDT, 27 June 1997.

**Figure 55.** Radar-derived wind directions and in-situ observations at the MBARI M1 mooring, Moss Landing (MLML) and Santa Cruz (UCSC) for 1200 PDT, 27 June 1997.

**Figure 56.** Radar-derived wind directions and in-situ observations at the MBARI M1 mooring, Moss Landing (MLML) and Santa Cruz (UCSC) for 1300 PDT, 27 June 1997.
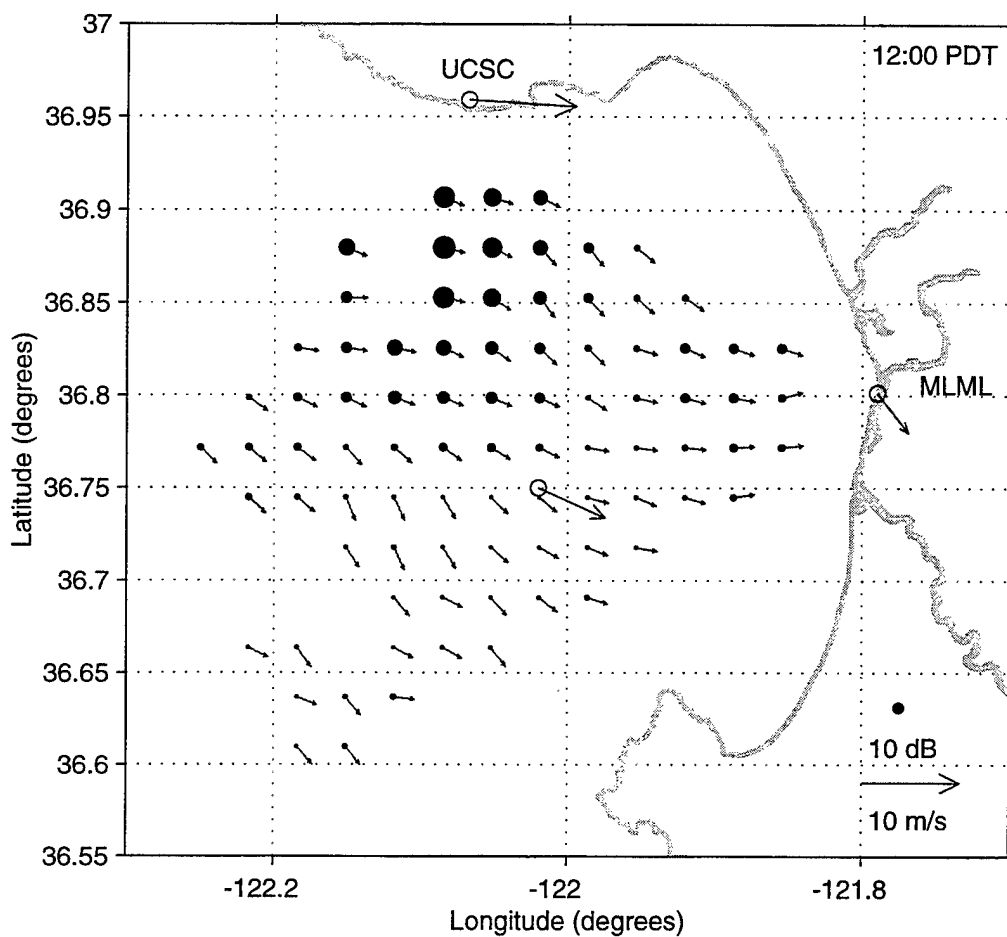
**Figure 57.** Radar-derived wind directions and in-situ observations at the MBARI M1 mooring, Moss Landing (MLML) and Santa Cruz (UCSC) for 1400 PDT, 27 June 1997.
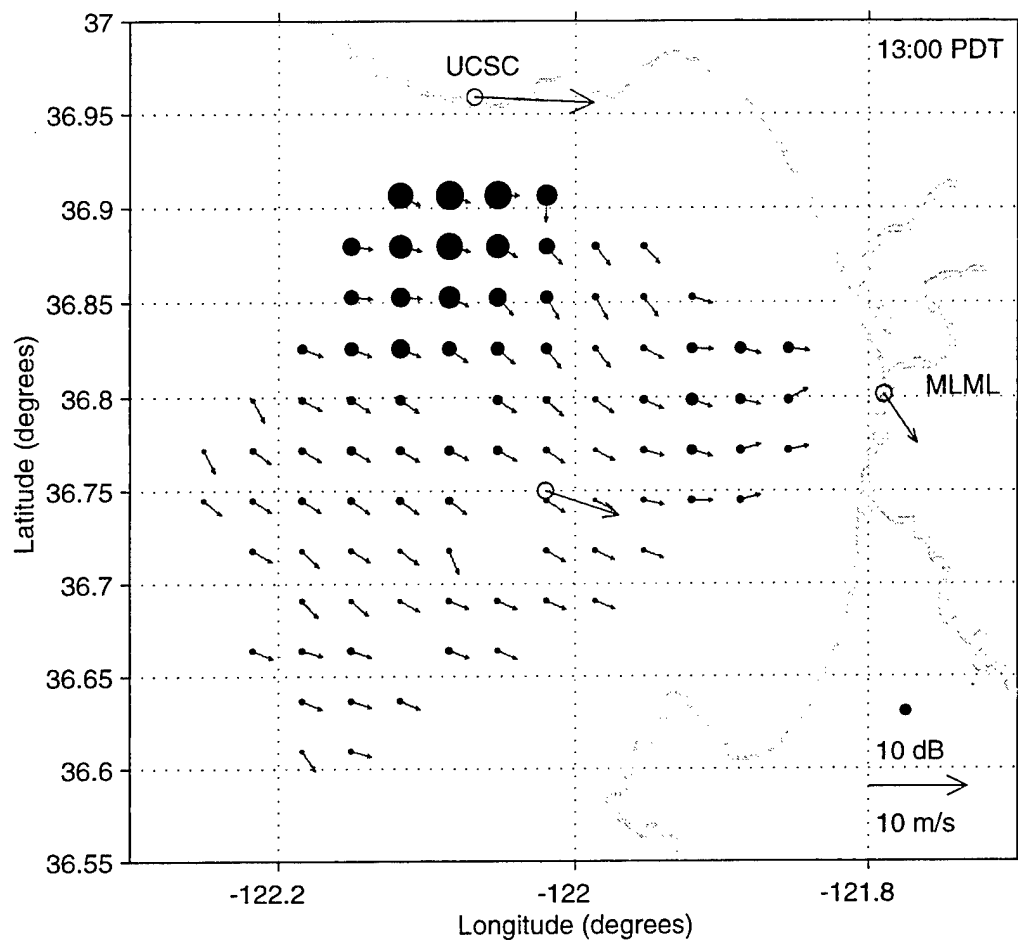
**Figure 58.** Radar-derived wind directions and in-situ observations at the MBARI M1 mooring, Moss Landing (MLML) and Santa Cruz (UCSC) for 1500 PDT, 27 June 1997.

**Figure 59.** Radar-derived wind directions and in-situ observations at the MBARI M1 mooring, Moss Landing (MLML) and Santa Cruz (UCSC) for 1600 PDT, 27 June 1997.
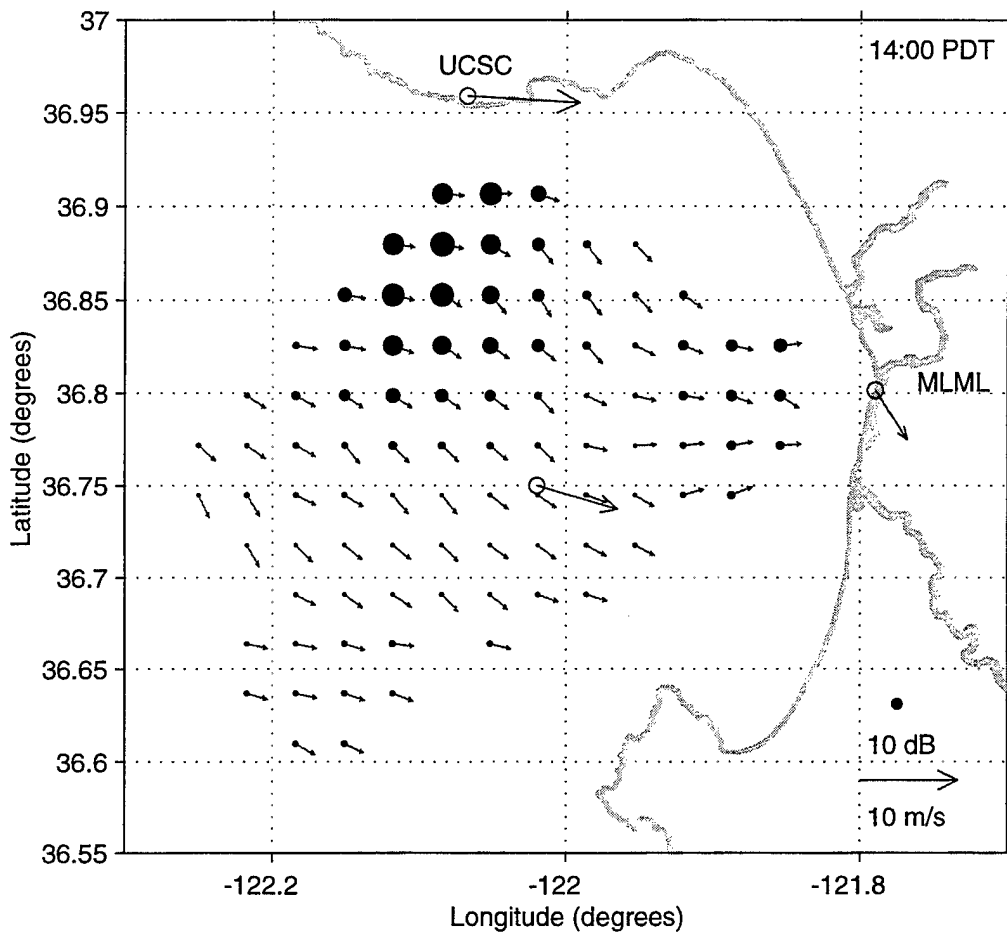
**Figure 60.** Radar-derived wind directions and in-situ observations at the MBARI M1 mooring, Moss Landing (MLML) and Santa Cruz (UCSC) for 1700 PDT, 27 June 1997.

104

**Figure 61.** Radar-derived wind directions and in-situ observations at the MBARI M1 mooring, Moss Landing (MLML) and Santa Cruz (UCSC) for 1800 PDT, 27 June 1997.
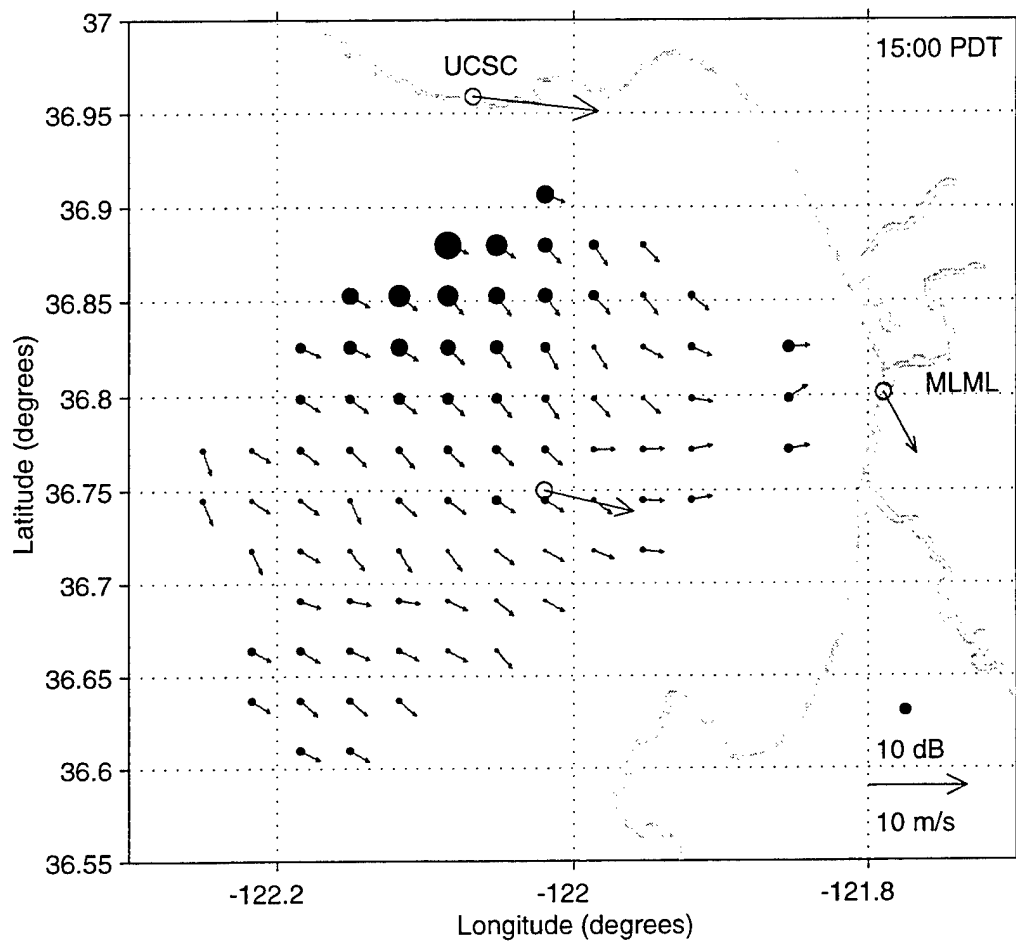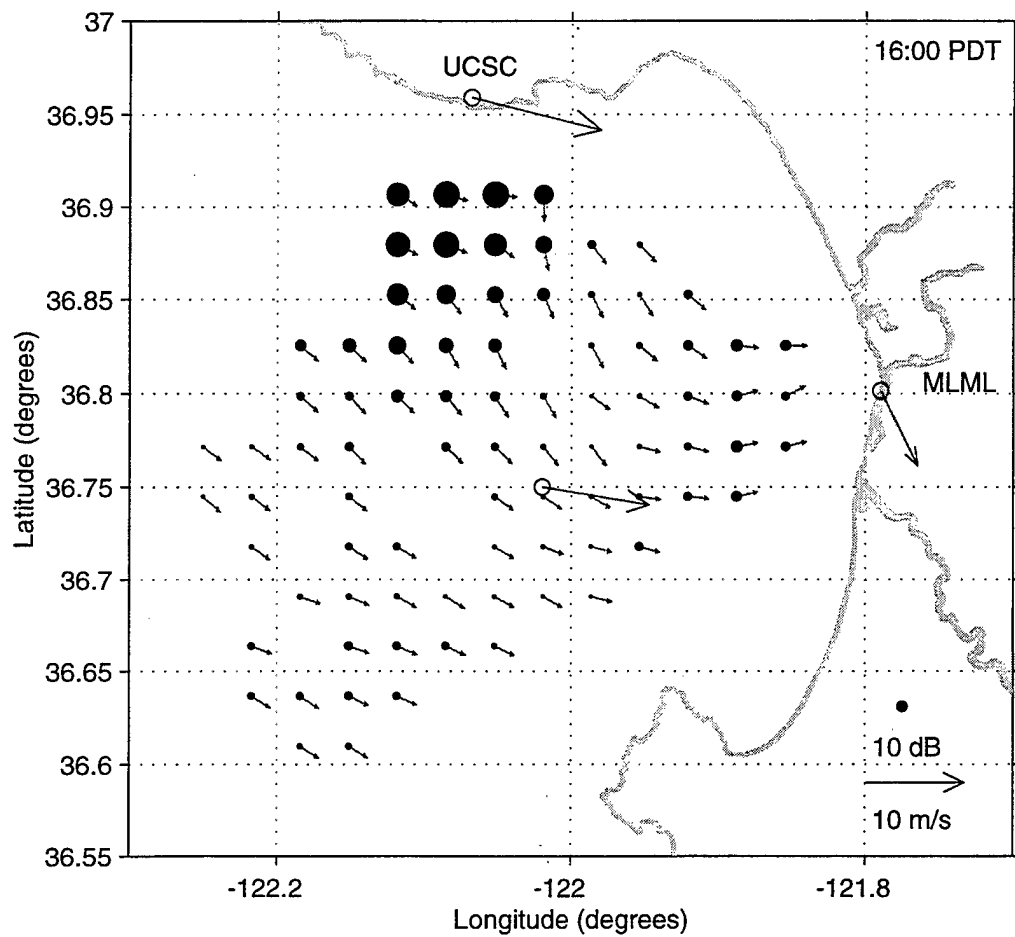
105

**Figure 62.** Radar-derived wind directions and in-situ observations at the MBARI M1 mooring, Moss Landing (MLML) and Santa Cruz (UCSC) for 1900 PDT, 27 June 1997.

**Figure 63.** Radar-derived wind directions and in-situ observations at the MBARI M1 mooring, Moss Landing (MLML) and Santa Cruz (UCSC) for 2000 PDT, 27 June 1997.

**Figure 64.** Radar-derived wind directions and in-situ observations at the MBARI M1 mooring, Moss Landing (MLML) and Santa Cruz (UCSC) for 2100 PDT, 27 June 1997.
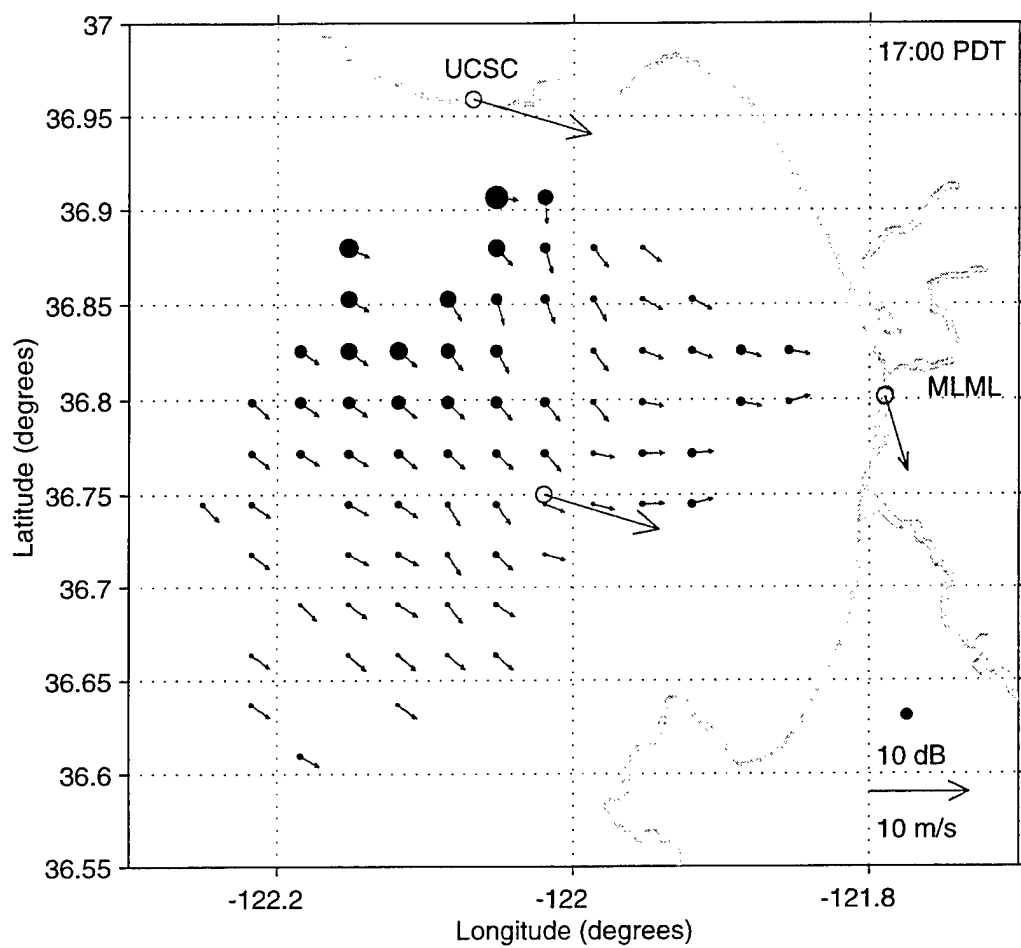
**Figure 65.** Radar-derived wind directions and in-situ observations at the MBARI M1 mooring, Moss Landing (MLML) and Santa Cruz (UCSC) for 2200 PDT, 27 June 1997.

**Figure 66.** Radar-derived wind directions and in-situ observations at the MBARI M1 mooring, Moss Landing (MLML) and Santa Cruz (UCSC) for 2300 PDT, 27 June 1997.
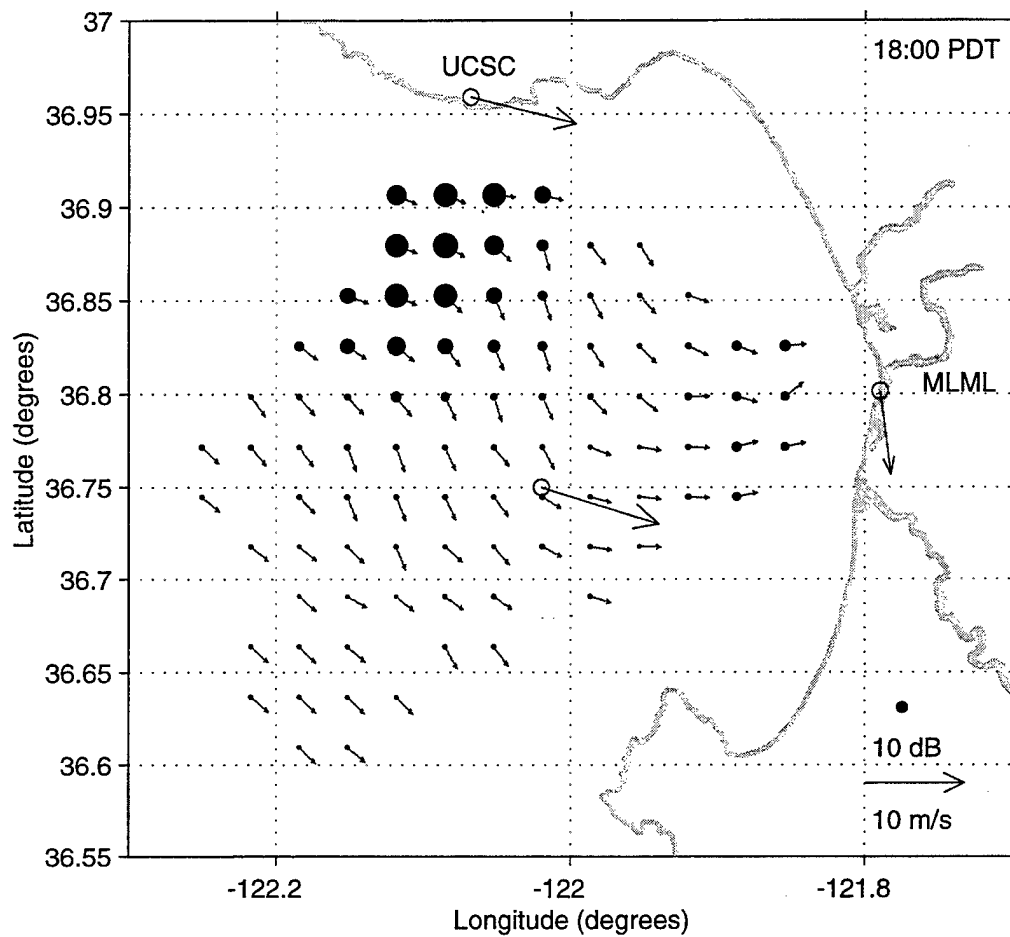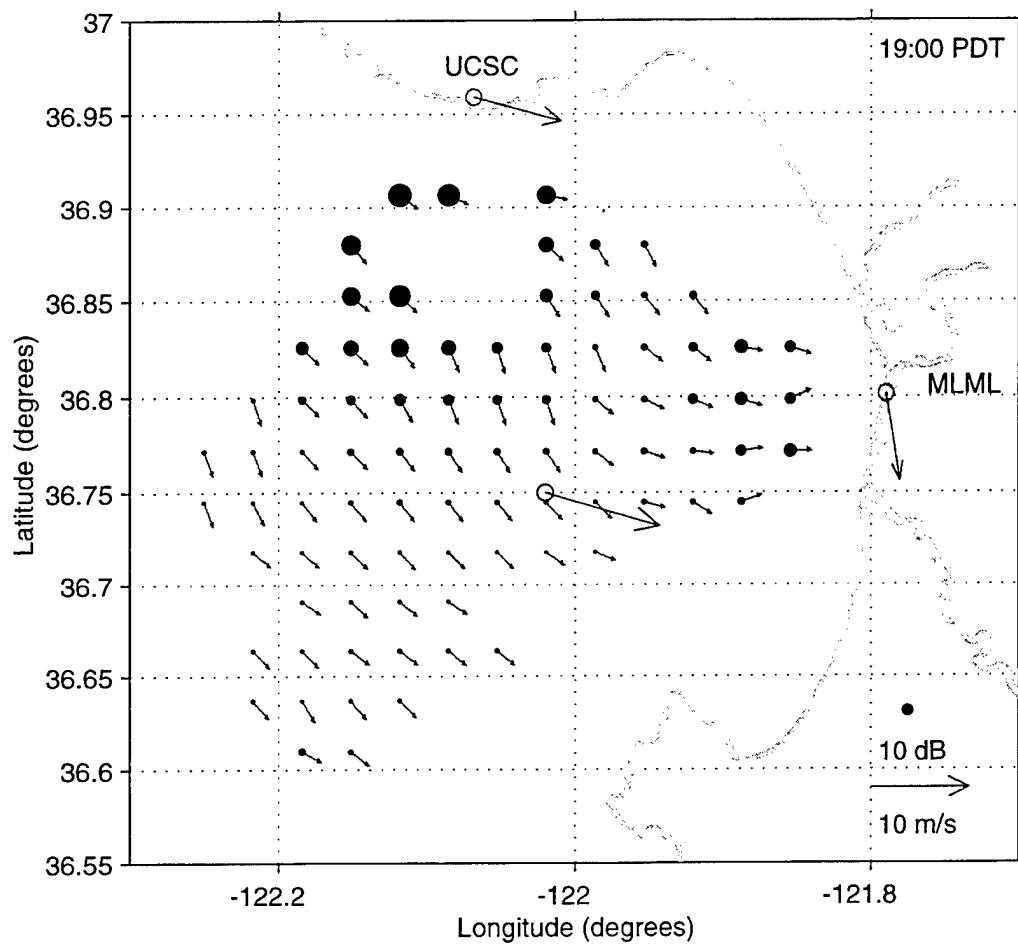
110

**Figure 67.** Radar-derived wind directions and in-situ observations at the MBARI M1 mooring, Moss Landing (MLML) and Santa Cruz (UCSC) for 0600 PDT, 16 August 1997.
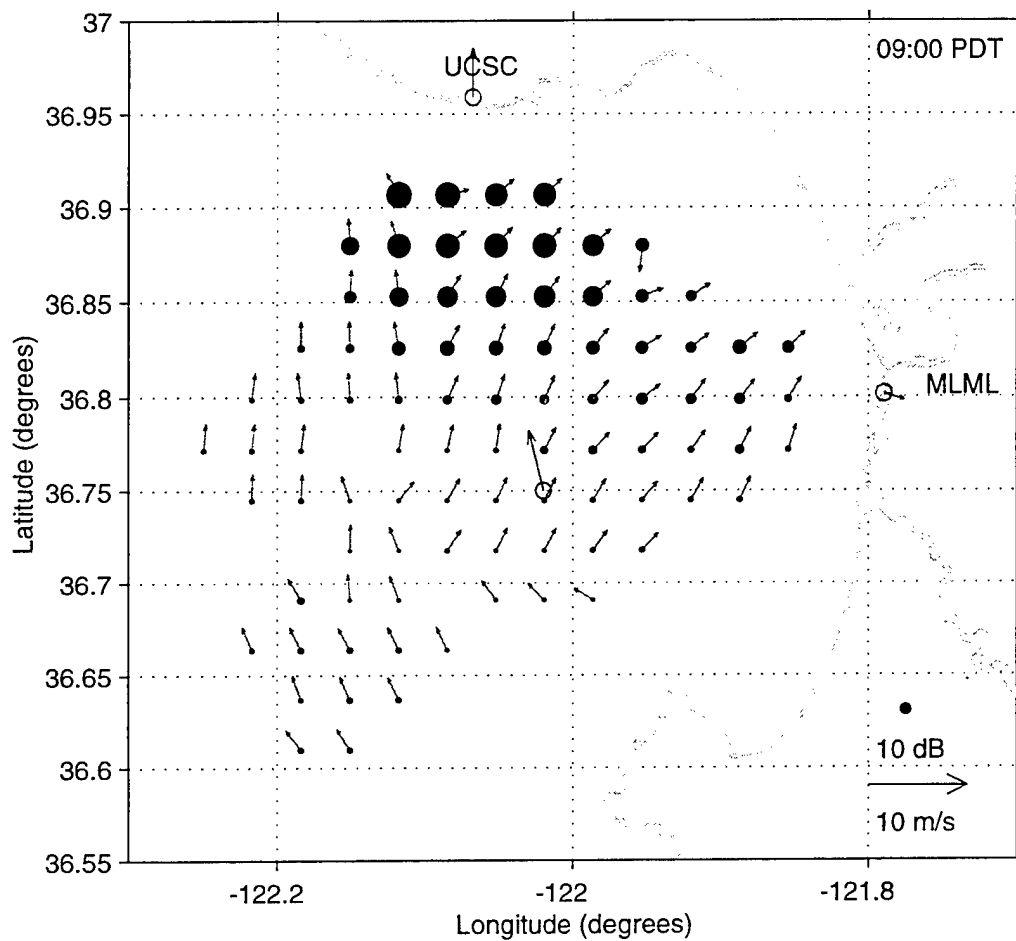
**Figure 68.** Radar-derived wind directions and in-situ observations at the MBARI M1 mooring, Moss Landing (MLML) and Santa Cruz (UCSC) for 0900 PDT, 16 August 1997.
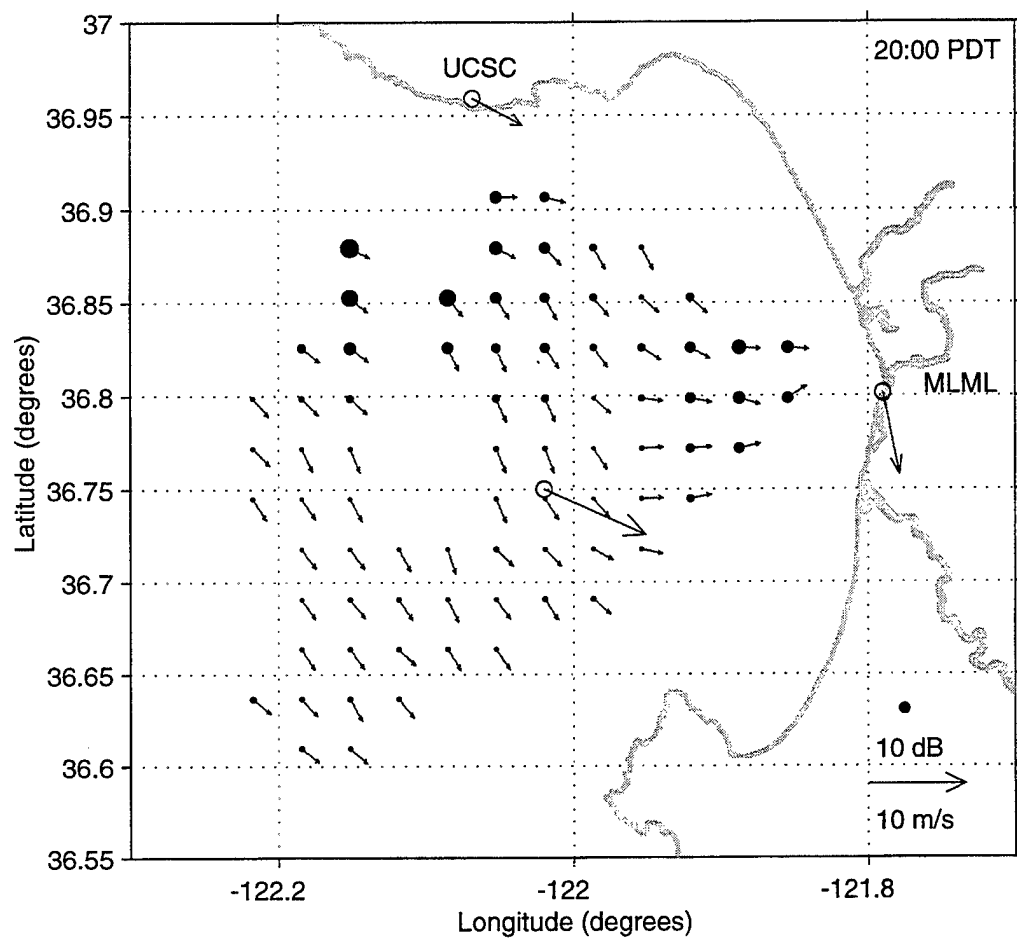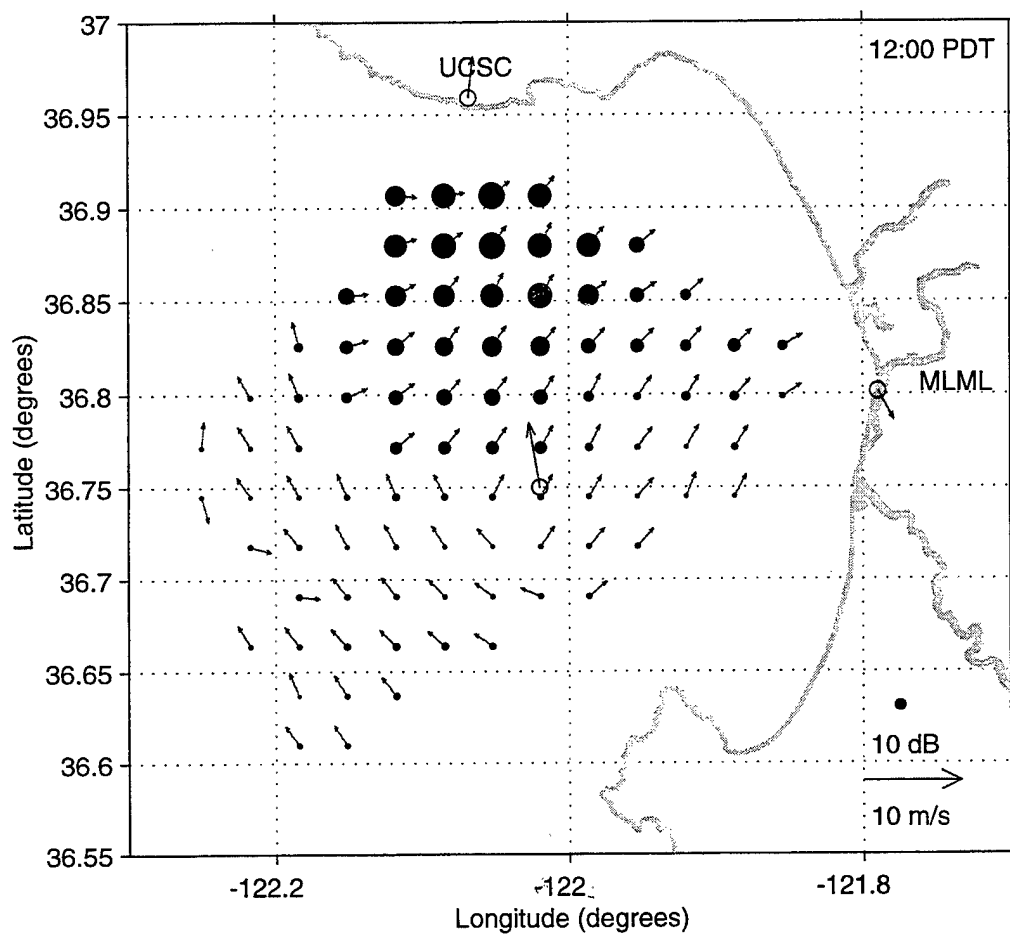
**Figure 69.** Radar-derived wind directions and in-situ observations at the MBARI M1 mooring, Moss Landing (MLML) and Santa Cruz (UCSC) for 1200 PDT, 16 August 1997.
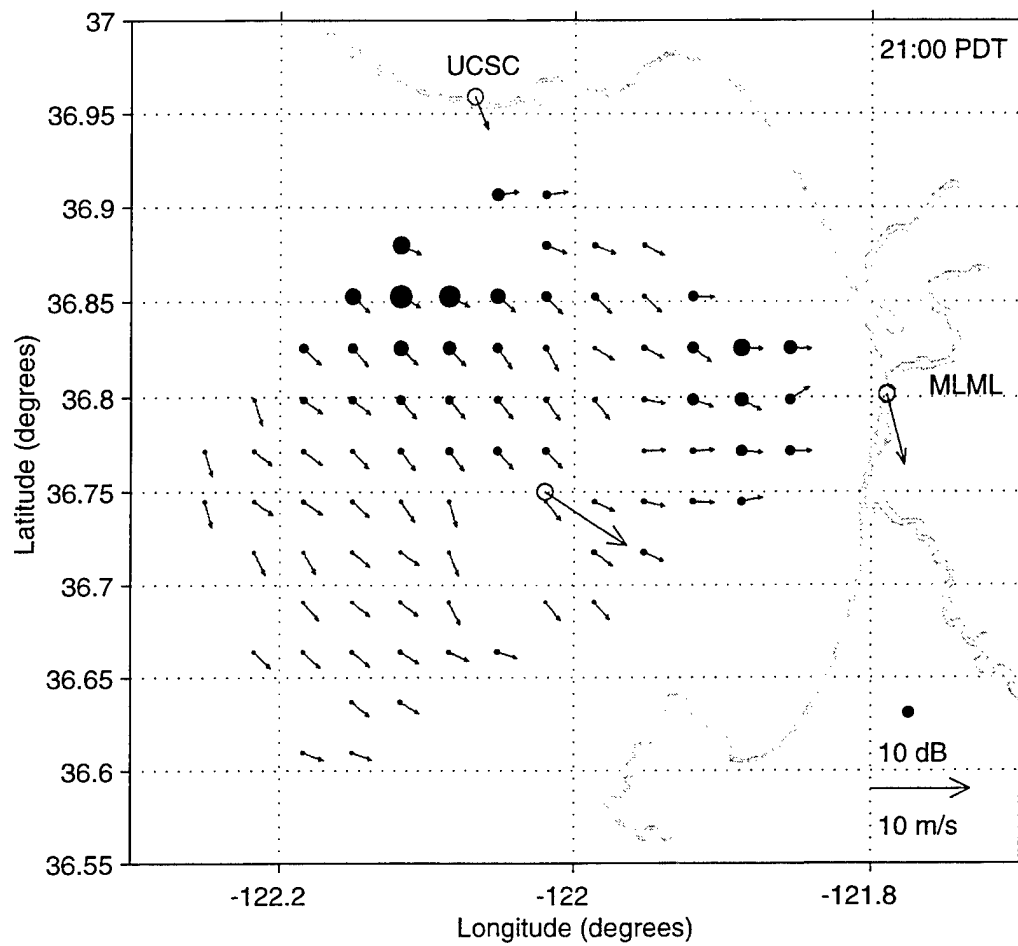
**Figure 70.** Radar-derived wind directions and in-situ observations at the MBARI M1 mooring, Moss Landing (MLML) and Santa Cruz (UCSC) for 1400 PDT, 16 August 1997.

114
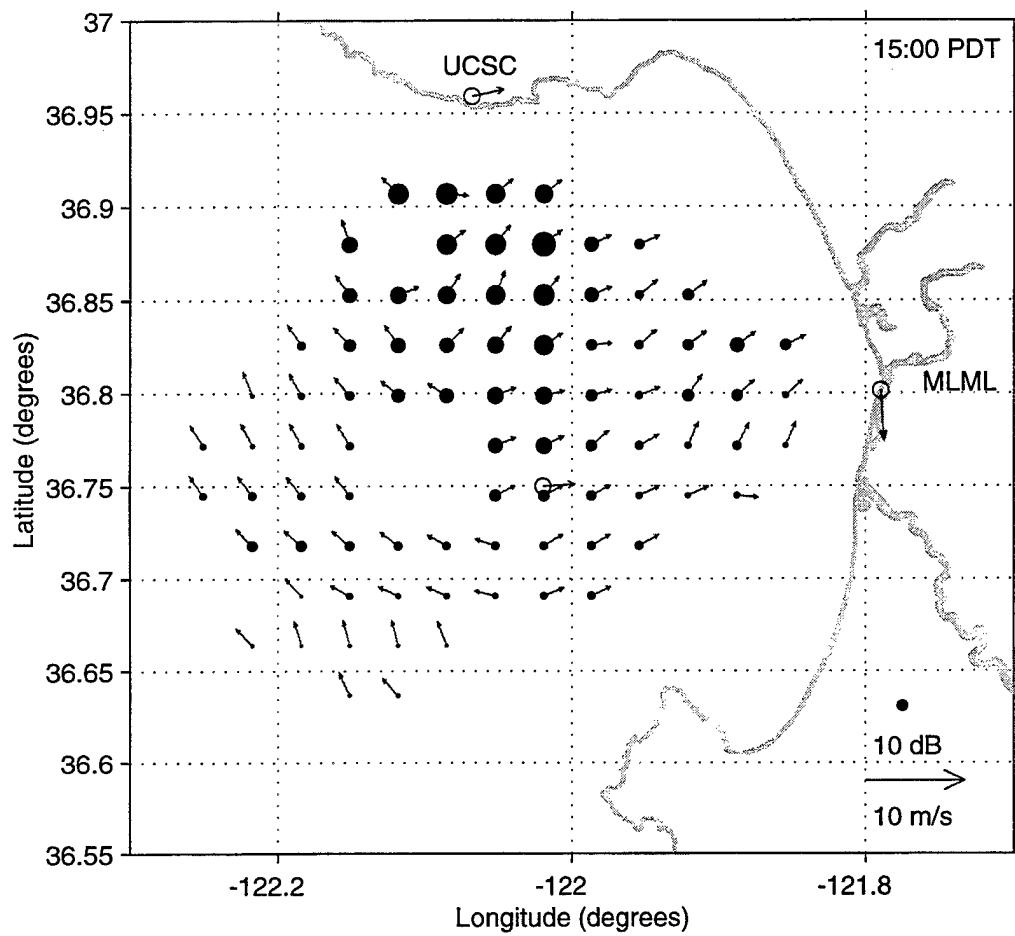
**Figure 71.** Radar-derived wind directions and in-situ observations at the MBARI M1 mooring, Moss Landing (MLML) and Santa Cruz (UCSC) for 1500 PDT, 16 August 1997.
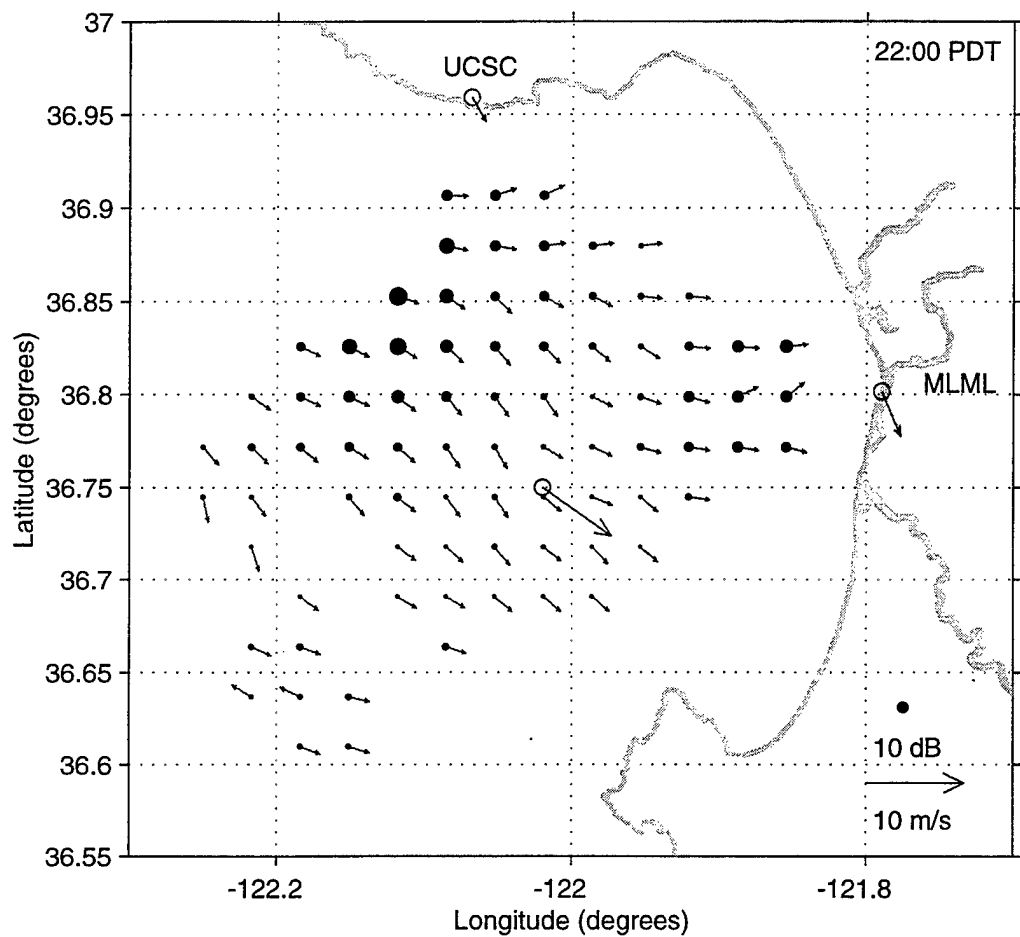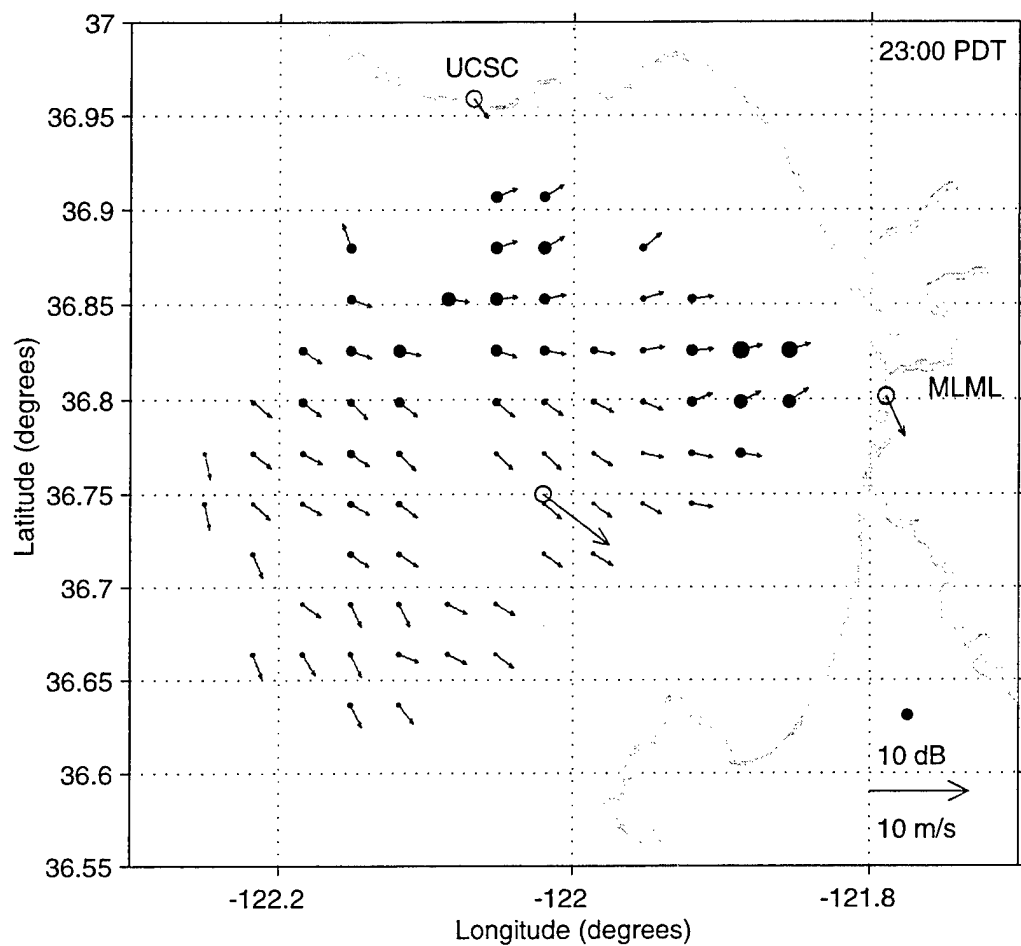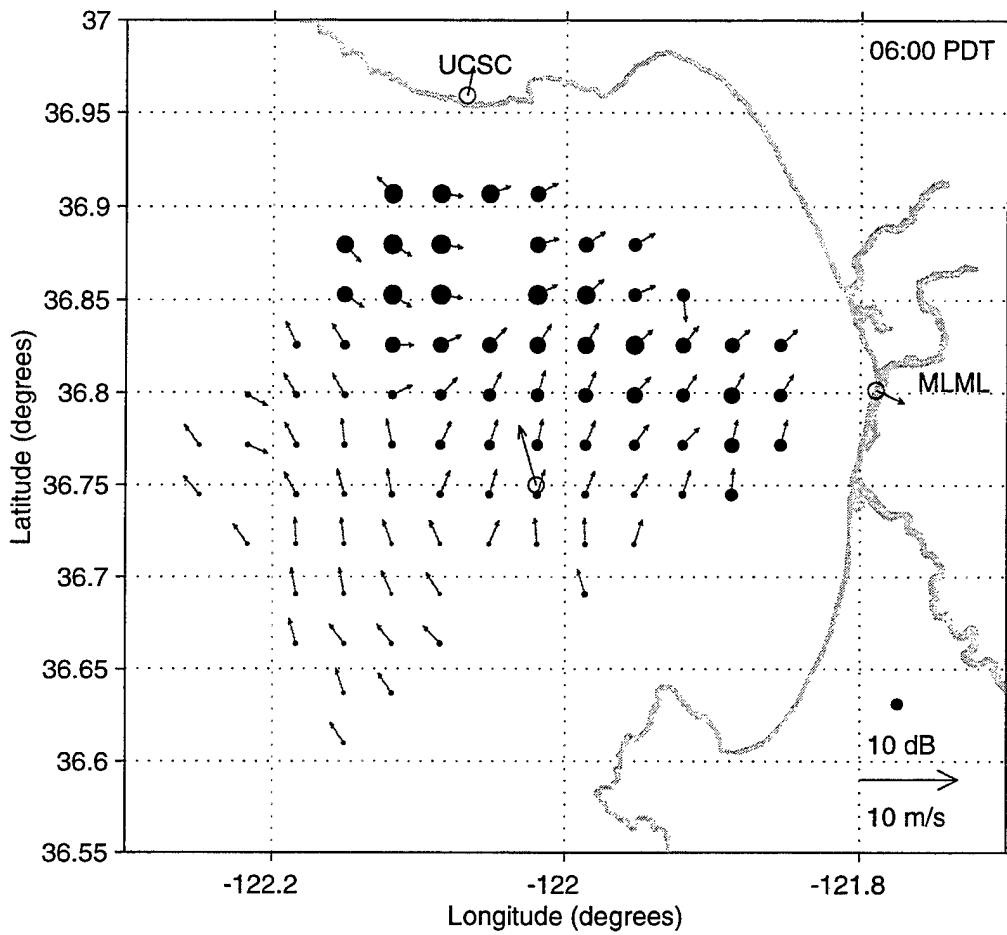
115
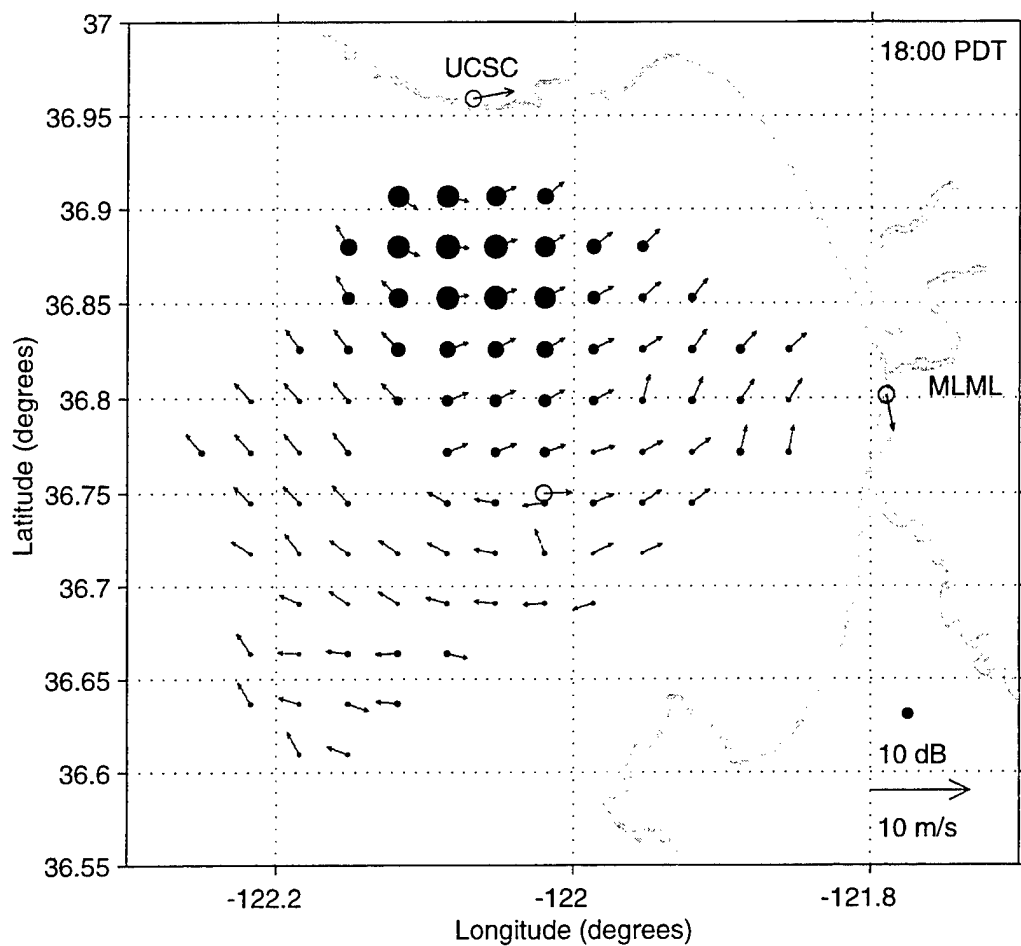
**Figure 72.** Radar-derived wind directions and in-situ observations at the MBARI M1 mooring, Moss Landing (MLML) and Santa Cruz (UCSC) for 1800 PDT, 16 August 1997.
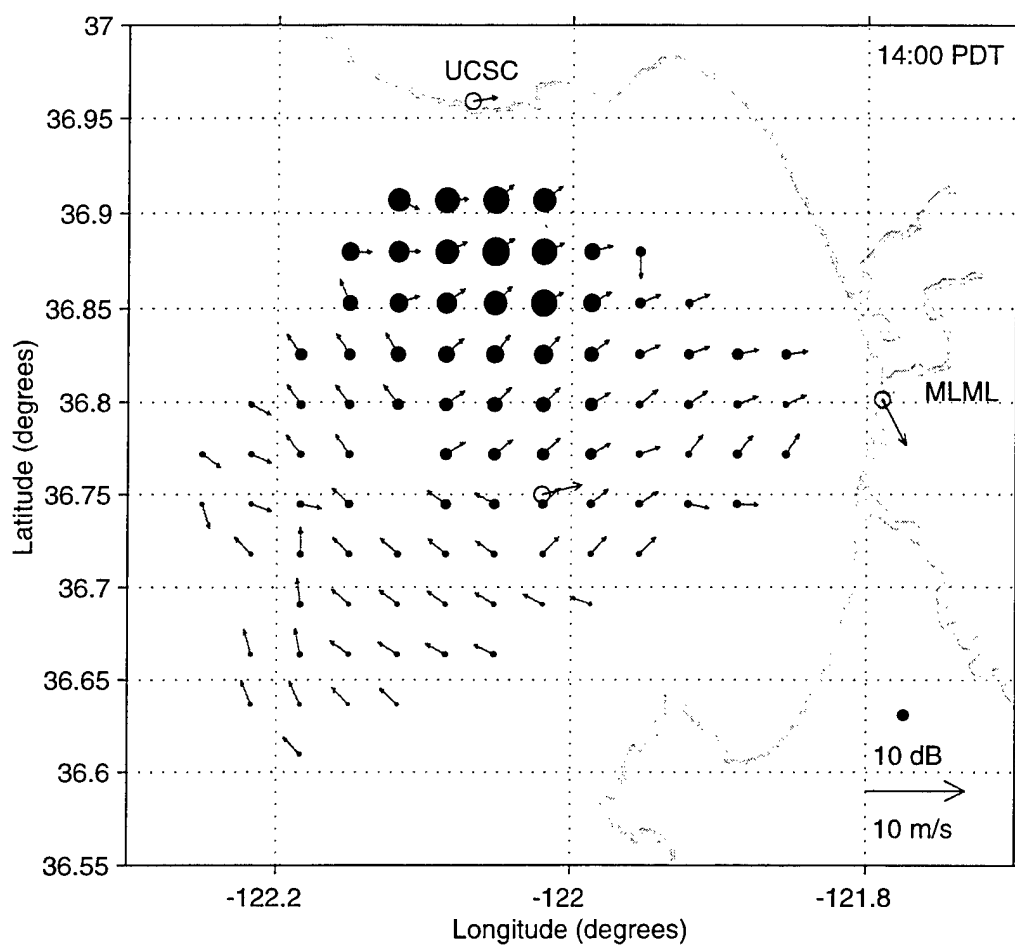
116

# V. SUMMARY AND RECOMMENDATIONS

## A.    SUMMARY

High frequency (HF) radar echo measurements made by the new phased-array Multi-frequency Coastal Radar (MCR) systems located at Santa Cruz and Moss Landing during the summer period 1997 were processed using conventional beam processing to create power density spectra for range-azimuth cells spaced every 3 km to approximately 45 km in range and every 5° in bearing from -50° to +50° measured from the broadside direction of each radar.  The ratio of the first-order Bragg peaks, as well as the noise level, were calculated and recorded for each spectrum.

Comparisons between the MBARI mooring M1 observations and the radar output indicated that the Bragg ratio generally fluctuates with the wind direction measured at the mooring, but also oscillates with the diurnal change in wind speed, for all four MCR frequencies, particularly at the Santa Cruz site.  The magnitude of oscillation of the Bragg ratios was greater for the lower frequencies of the MCR.  The ratio tended toward zero during times when the wind speed was low ($< 5$ m s$^{-1}$).  Further analysis indicated that the SNR for each side of the spectrum also fluctuates closely with wind speed primarily due to the diurnal fluctuation of the noise level.  The diurnal fluctuation of the noise level implied that Bragg-resonant waves were still growing and had not reached their saturation (i.e. fully developed) levels, or many Bragg peaks may not have been statistically above the noise floor.  The exception to these trends was channel 3.  The Santa Cruz channel 3

117

noise level varied little with wind speed. The Moss Landing channel 3 Bragg ratio roughly followed the mooring wind direction, and the upper side SNR was markedly higher than any other channel.

The Bragg ratio of each spectra was then inverted to a wind direction via the linear relationship of Georges et al. (1993) since the 24-dB upwind/downwind reference level was generally consistent with the MCR output. The linear model was used instead the Long-Trizna (1973) model due to better fit with the in-situ data, and instead of the cardioid model (Stewart and Barnum, 1975) because the Bragg ratios required to produce winds near-parallel to the radar look direction were beyond the observed dynamic range of the MCR systems.

A new wind-retrieval algorithm was created to resolve the left-right direction ambiguity inherent to all HF radar wind estimates. The algorithm computes the most appropriate combination of average solutions from each site for points on a 3-km Cartesian grid. Only radar data that meets a given SNR criteria are considered for the wind-retrieval algorithm.

Objective comparisons of radar-derived wind directions based on a low SNR threshold and the mooring M1 observations showed little correlation. However, when the SNR threshold was increased, the correlation improved and much of the spurious data was disregarded. Among the four channels, the comparisons verified that channel 3 best agreed with the mooring measurements. Further analysis showed that when the data is sub-divided into times when the mooring wind speed was greater than 5 m s$^{-1}$, the agreement significantly improved. Increasing the wind speed criteria to 7.5 m s$^{-1}$ further

improved the correlation. Furthermore, when the high wind conditions were separated into times when the wind speed sustained for more than 12 hr, a large majority of radar-derived estimates were within 15° of the mooring-measured wind direction.

Based on the times when there was good agreement with the mooring, full-field wind maps were produced. However, when a SNR threshold of 5 dB was used, the amount of usable data was insufficient to produce maps with any consistent spatial coverage. Although the data that met the higher threshold could be viewed with higher confidence, the threshold was lowered to 3 dB so more of the radar data was accepted. The radar-derived wind field was found to agreed quite well with the M1 mooring and land observations, particularly during the afternoon and evening hours when wind speeds were higher, and fully developed seas likely existed. During the early morning hours the radar-derived wind directions agreed less with the observations due to low backscatter intensity of smaller radar-resonant waves during low wind conditions. The radar also identified a wind-reversal during which northward flow dominated Monterey Bay. Despite the limited fetch of offshore flow and somewhat lower wind speeds, there was clear northward flow in the radar-derived wind directions. However, when the northward winds dissipated, the radar-derived winds persisted due to the time lag required for radar-resonant waves to decay and transition back to southeastward propagation.

## B.   RECOMMEDATIONS

The accuracy of MCR-derived wind directions is sensitive to the signal-to-noise ratio (SNR). Instead of setting fixed SNR criteria, as was done in this study, the variance

of the noise floor for each particular spectrum should determined in the spectra generation algorithm. The statistical significance of both Bragg peaks over the noise could then be determined for each radar measurement, and a variable SNR threshold could be applied to the various times and locations of the data. Although the MCR units have since been outfitted with more powerful amplifiers to increase the SNR, this selective thresholding process would further increase the confidence of the radar-derived directions and likely improve the amount of usable data.

Although the ground-wave MCR measurements were found to be generally consistent with the upwind reference level (24 dB) determined by earlier studies that used sky-wave radar, the high variability of the MCR data precluded establishment of a more appropriate value. Further analysis of MCR output at different sites and during more variable wind conditions, as well as detailed analysis of radar calibration data during simultaneous transponder trials, is recommended in order to establish a more appropriate value.

The measurement of wind speed by HF radar was not directly addressed in this study. However, the diurnal fluctuations noted in the Bragg peak power levels coincident with the wind speed variations measured by in-situ sensors suggests a potential way to infer wind speed from the first-order pattern in the HF spectrum. Alternatively, the unique capability of the MCR to simultaneously measure four radar-resonant ocean waves could be used infer wind speed from the near-surface current shear measured by the radar. It is recommended that both of these approaches be examined further so that a full radar-derived wind vector could be ascertained.

# LIST OF REFERENCES

Ahern, J.L., S.R. Curley, J.M. Headrick, and D.B. Trizna, 1974: Tests of remote skywave measurements of ocean surface conditions. *Proceedings of the IEEE*, 62, 681-687.

Fernandez, D.M., H.C. Graber, J.D. Paduan, and D.E. Barrick, 1997: Mapping wind direction with HF radar. *Oceanography*, 10, 93-95.

Foster, M.D., 1993: Evolution of diurnal surface winds and surface currents for Monterey Bay, M.S. thesis, 100 pp., Naval Postgrad. School, Monterey, CA.

Georges, T.M., J.A. Harlan, L.R. Meyer, and R.G. Peer, 1993: Tracking hurricane Claudette with the U.S. Air Force over-the-horizon radar. *J. Atmos. and Oceanic Tech.*, 10, 441-451.

Ha, E.C., 1979: Remote sensing of ocean surface current and current shear by HF backscatter radar. Ph.D. Dissertation, Stanford University, Tech. Rep. D415-1.

Hasselman, K., 1971: Determination of ocean wave spectra from Doppler radio return from the sea surface. *Nature Phys. Sci.*, 229, 16-17.

Haus, B.K., H.C. Graber, and L.K. Shay, 1997: Synoptic measurements of dynamic oceanic features. *Oceanography*, 10, 45-48.

Heron, M.L., P.E. Dexter, and B.T. McGann, 1985: Parameters of the air-sea interface by high-frequency ground-wave HF Doppler radar. *Aust. J. Mar. Freshwater Res.*, 36, 655-670.

Kinsman, B., 1965: *Wind Waves*. Ch. 6. Prentice-Hall, Englewood Cliffs, NJ.

Long, A.E., and D.B. Trizna, 1973: Mapping of North Atlantic winds by HF radar sea backscatter interpretation. *IEEE Trans. Antennas Propag.*, AP-21, 680-685.

Paduan, J.D. and L.K. Rosenfeld, 1996: Remotely sensed surface currents I Monterey Bay from shore-based HF radar (Coastal Ocean Dynamics Application Radar). *J. Geophys. Res.*, 101(C9), 20,669-20,686.

_____ , and H.C. Graber, 1997: Introduction to high frequency radar: reality and myth. *Oceanography*, 10, 36-39.

Phillips, O.M.,1981: The structure of short gravity waves on the ocean surface. In: *Spaceborne Synthetic Aperture Radar for Oceanography* (R.C. Beal, P. Deleonibus and I. Katz, eds.). Johns Hopkins Univ. Press, Baltimore MD, pp 24-31.

Pierson, J.P., L.J. Tick, and L. Baer, 1966: In *Proceed. 1966 Symp.*, Naval Hydrodynamics, ACR-136, pp. 400-452.

Shearman, E.D.R., 1981: Remote sensing of ocean waves, currents and surface winds by deka metric radar. In: *Remote Sensing in Meteorology, Oceanography and Hydrology*. A.P. Cracknell, ed. Ellis Horwood, London, 312-335.

Stewart, R.H., and J.R. Barnum, 1975: Radio measurements of oceanic winds at long ranges: an evaluation. *Radio Sci.*, 10, 853-857.

Sverdrup, H.U., and W.H. Munk, 1947: Wind, sea and swell: theory of relations for forecasting. U. S. Navy Hydrographic Office Pub. No. 601. 44 pp.

Teague, C.C., J.F. Vesecky, P.E. Hansen, N.G. Schepf, J.M. Daida, R.G. Onstott, K. Fischer, D.M. Fernandez, 1997: Initial observations of ocean currents, current shears and wind direction using multi-frequency HF radar. *IGARSS '97 Proceedings*, Piscataway, NJ: IEEE Press.

Tyler, G.L., C.C. Teague, R.H. Stewart, A.M. Peterson, W.H. Munk, and J.W. Joy, 1974: Wave directional spectra from synthetic aperture observations of radio scatter. *Deep-Sea Res.*, 21(12), 989-1016.

Vesecky, J.F., C.C. Teague, F.L. Ludwig, , R.G. Onstott, P. Hansen, N Schnepf, D. Fernandez, J. Diada, and K. Fischer, 1997: Multifrequency HF Radar Observations on Coastal Dynamics. Progress report, Project 032883, University of Michigan, Ann Arbor, MI, 48109-2143.

_____, F.L. Ludwig, C.C. Teague, W. Nuss, R.G. Onstott, P. Hansen, D. Fernandez, J. Diada, and K. Fischer, 1998: Estimating the surface wind field over coastal oceans using multi-frequency high frequency radar and in situ observations. Proceedings, 2nd AMS Conference on Coastal Atmospheric and Ocean Processes, Phoenix, AZ.

Wu, J., 1969: Wind stress and surface roughness at air-sea interface. *J. Geophys. Res.*, 74(2), 444 - 455.

# INITIAL DISTRIBUTION LIST

No. Copies

1. Defense Technical Information Center.............................................................2
   8725 John J. Kingman Rd., STE 0944
   Ft. Belvoir, VA 22060-6218

2. Dudley Knox Library.......................................................................................2
   Naval Postgraduate School
   411 Dyer Rd.
   Monterey, CA 93943-5101

3. Superintendent.................................................................................................2
   Attn: Chairman, Department of Meteorology (Code MR/WX)
   Naval Postgraduate School
   Monterey, CA 93943-5000

4. Superintendent.................................................................................................1
   Attn: Chairman, Department of Oceanography (Code OC/CO)
   Naval Postgraduate School
   Monterey, CA 93943-5000

5. Superintendent.................................................................................................2
   Attn: Professor J. D. Paduan (Code OC/PD)
   Naval Postgraduate School
   Monterey, CA 93943-5000

6. Lieutenant Raymond R. Delgado .................................................................1
   NAVEURMETOCCEN
   PSC 819, Box 31
   FPO AE, 09645-3200

7. Superintendent.................................................................................................1
   Naval Research Laboratory
   7 Grace Hopper Avenue Stop 2
   Monterey, CA 93943-5502

8. Dr. Calvin Teague ..........................................................................................1
   232 Durand Building
   Stanford University
   Stanford, CA 94305

9.      Dr. John Vesecky............................................................................ 1
        Space Physics Research Laboratory
        University of Michigan
        Arbor, MI  48109

10.     Dr. Dennis Trizna ......................................................................... 1
        Office of Naval Research (Code 321-SR)
        800 North Quincy Street
        Arlington, VA  22217-5660